

Ph.D. thesis

Accumulation of a large number of antiprotons and
production of an ultra-slow antiproton beam

反陽子の大量捕捉と
超低速反陽子ビームの生成

東京大学大学院理学系研究科
物理学専攻
黒田 直史

December 19, 2003

Abstract

A large number of antiprotons, approximately five millions, the largest number ever accumulated, have been successfully trapped in an electromagnetic trap called an MRT (Multi-ring trap) in combinations with the RFQD (radio frequency quadrupole decelerator) and the AD (Antiproton Decelerator) at CERN. Antiprotons emerging at 5.3 MeV from the AD were decelerated to 110 keV by the RFQD, and were injected in the MRT installed in a cold bore (≈ 10 K) of a superconducting solenoid via double degrader foils of $90 \mu\text{g}/\text{cm}^2$ each, which reduced the antiproton energy lower than ≈ 10 keV.

Electrons were preloaded in the MRT to cool the antiprotons to sub-electronvolt energy region. The electrons cool themselves via synchrotron radiation and behave as a non-neutral plasma. The time evolutions of plasma modes have revealed, for the first time, the cooling feature of antiprotons nondestructively.

Further, ultra-slow antiproton beams of 10–500 eV have been extracted from the MRT and the beam was transported to the target area via a beam line designed for efficient transport of slow antiprotons realizing at the same time differential pumping of more than six orders of magnitude. By ramping up the trapping potential slowly, ultra-slow antiprotons of 10–500 eV have been extracted from the strong magnetic field region for the first time.

The accumulation of a large number of antiprotons and the production of ultra-slow antiproton beams are expected to open a new field of research of antiprotonic atoms and antihydrogen under well-controlled conditions.

Contents

Abstract	i
1 Why ultra-slow antiprotons?	1
1.1 Background	1
1.1.1 Atomic physics with antiprotons	1
1.2 Motivations	3
1.2.1 Antiprotonic atom formation	3
1.2.2 Cold antihydrogen atoms	6
1.3 Charged particle trap	11
1.3.1 Antiproton confinement in the trap	13
2 Apparatus	17
2.1 The Antiproton Decelerator	18
2.2 The Radio Frequency Quadrupole Decelerator	20
2.3 Antiproton trap	26
2.3.1 Multi-ring trap	27
2.3.2 Superconducting solenoid	29
2.3.3 Energy degrading thin foil	29
2.3.4 MOS-FET high-voltage transistor switch	30
2.3.5 Electron emitter	32
2.4 Transport beam line	32
2.5 Detection system	36

2.5.1	Beam profile monitor	36
2.5.2	Microchannel plate with delay-line anode	39
2.5.3	Čerenkov detector	39
2.5.4	Track detector	40
2.6	Control and data acquisition system	43
3	Confinement of antiprotons	45
3.1	Scheme of the confinement of antiprotons in the MRT	45
3.2	Antiproton beam transport to the MRT	48
3.2.1	Beam transport at the MEBT	49
3.2.2	Tuning of the buncher phase	49
3.2.3	Transport of 110 keV antiproton beam at the LEBT	50
3.3	Degrading antiproton beam energy through thin foils	51
3.3.1	Energy loss in the PET foils	51
3.3.2	Energy distribution of the degraded antiprotons	54
3.4	Confinement in the MRT	57
3.4.1	Capture of the 10 keV antiprotons	58
3.4.2	Confinement of antiprotons in the MRT	58
3.4.3	Vacuum condition for stable confinement	60
4	Cooling of antiprotons in the MRT	67
4.1	Electrostatic modes of the electron plasma	67
4.1.1	Axially symmetric electrostatic modes	67
4.1.2	Observed axially symmetric modes of electron plasma	71
4.2	Electron cooling feature	73
4.2.1	Experimental setup	75
4.2.2	Synchrotron radiation cooling of electrons	76
4.2.3	The frequency shift of the (3,0) mode	77
4.3	The frequency shift of the (1,0) mode	82

5	Extraction and transportation of ultra-slow antiprotons	87
5.1	Antiproton beam extraction from the MRT	87
5.1.1	Disturbance by electrons during the slow extraction	87
5.1.2	Slow extraction of antiprotons from the MRT	90
5.2	Ultra-slow antiproton beam transport	90
5.3	Extraction efficiency	97
5.3.1	Attempt of the radial compression of the antiproton cloud	98
6	Conclusions	101
A	Planned atomic collision experiment	103
A.1	Antiproton collision experimental chamber	103
B	Sideband cooling	107
B.1	Particle motion in a trap	107
B.2	Sideband cooling	108
B.3	Radial compression of proton and H_3^+ ion cloud	110
C	Properties of nonneutral plasma	113
C.1	Plasma oscillation	113
C.2	Debye shielding	114
C.3	Rigid rotor equilibrium	114
C.3.1	Vlasov equation	116
C.3.2	Rigid rotor Vlasov equilibria	117
	Acknowledgements	133

Chapter 1

Why ultra-slow antiprotons?

1.1 Background

1.1.1 Atomic physics with antiprotons

Antiproton, the antiparticle of proton was discovered in 1955 at Bevatron, Berkeley, by Chamberlain, Segré, Wiegand and Ypsilantis [1] injecting 6.2 GeV protons on a copper target. After the discovery of antiproton, various investigations were performed, which include CPT symmetry tests (e.g. [2]), strong interaction of antiproton with nuclei via antiprotonic X-ray spectroscopy [3], ionization processes of atoms with antiprotons and protons [4], etc.

At CERN, Organisation européenne pour la recherche nucléaire or European Organization for Nuclear Research, the Antiproton Decelerator (AD), a facility providing low energy antiproton beam of $100 \text{ MeV}/c$ (5.3 MeV), was built primarily for atomic physics experiments like antihydrogen and antiprotonic atom syntheses, their spectroscopy, and collision experiments. The AD has been in operation since year 2000 as an alternative of LEAR (Low Energy Antiproton Ring), the first slow antiproton ring built in 1982.

Antiproton has infinite lifetime in vacuum (at least 10^{25} years [5]), it is an unique hadronic anti-particle in the sense that it can be stored, cooled, and also be manipulated to form an ultra-slow beam. Since the LEAR era, while researches like exotic meson survey [6] or CPT-symmetry [2] using proton-antiproton annihilation have been studied, some low energy antiproton experiments in the field related to the atomic physics has also

been performed [7]. Some examples of performed and ongoing experiments are listed;

- Various exciting findings in the field of atomic physics were made by PS194 collaboration during the period of LEAR, e.g., double ionization cross sections of He by antiproton was found to be two times larger than those by protons in a fast collision region, which is not theoretically solved even now. The energy regions covered were not low enough to study antiprotonic atom formation processes in the LEAR period, and should be one of the most important subjects of the AD (See e.g. [4]).
- Antiprotonic helium atom ($\bar{p}\text{He}^+$) has been found to be metastable even in a dense He target [8] having lifetimes of microseconds. Because of this metastability, a high resolution laser spectroscopy can be applied, eventually reached the precision as high as 10^{-8} . Surprisingly, theoretical treatments of this three body system (antiproton + electron + alpha nucleus) were quite successful, giving almost perfect agreements with the observed transition energies when the charge and mass of protons were used instead of antiproton. Combining with the charge to mass ratio experiment described above, the mass and the charge of antiprotons have been evaluated with the precision of 10^{-8} , proving that the CPT symmetry between proton and antiproton with respect to mass and charge are conserved with the precision of 10^{-8} , or vice versa, under the assumption of the CPT symmetry, the three body calculation involving three particles with different mass with each other can be done with the precision of 6×10^{-8} [9][10].
- Antiproton trapping and cooling techniques were developed by PS196 and PS200 collaborations at LEAR (See e.g. [11][12]). The PS196 collaboration has found that the charge to mass ratio of \bar{p} is the same as that of proton to the precision of 9×10^{-11} [13].
- Antihydrogen atoms were synthesized in 1996 at CERN [14] for the first time, and in 1998 at Fermilab [15], Fermi National Accelerator Laboratory, even though the

atoms had a relativistic speed. After the AD launched, “cold” antihydrogen atoms were produced by two groups [16][17].

1.2 Motivations

There are two principal motivations for the accumulation of a large number of antiprotons and the production of ultra-slow antiproton beams. One is to investigate the initial processes of antiprotonic atom ($\bar{p}A^+$) formation, and the other is to synthesize a large number of cold antihydrogen atoms ($\bar{p}e^+$). The antiprotonic atoms are not only a unique object to provide a field of atomic process with a “heavy electron”, but also to permit precision test of CPT symmetry between matter and antimatter by high-resolution laser and microwave spectroscopy.

1.2.1 Antiprotonic atom formation

Antiprotonic atom is a bound system of an antiproton (\bar{p}) and an ion (A^+) by Coulomb force. When a slow antiproton collides with an atom, it can replace an outer-most electron in the atom and form an antiprotonic atom [18].

When antiprotonic atoms are formed in vacuum under single collision conditions, a considerable fraction of them are expected to be in metastable state. On the other hand, in dense media, antiprotonic atoms will annihilate immediately except for antiprotonic helium ($\bar{p}He^+$) which has been studied by using methods of laser and microwave spectroscopy [19] [20]. The simplest two body system of particle and antiparticle, antiprotonic hydrogen atom (protonium), $\bar{p}p$, is especially interesting among such antiprotonic atoms. Because such a two-body Coulombic system in Yrast state decays only via radiative transitions without external electric field, having life time longer than $1 \mu s$, the spectroscopic nature of $\bar{p}p$ will be studied precisely without three-body calculations. This figure is different in the case of $\bar{p}He^+$, though the spectroscopy of $\bar{p}He^+$ has been studied and revealed antiproton’s mass with precision of the order of 10^{-8} [9].

To produce an antiprotonic hydrogen atom, i.e., $\bar{p}p$, and study its spectroscopic nature,

it is performed between a dilute gas target (See App. A) and ultra-slow antiprotons whose energy should be less than ionization energy for target atoms or molecules. At this time, a considerable fraction of them are expected to be in metastable state.

A collision between an antiproton and an atom to be discussed satisfies a so-called adiabatic condition, i.e., $v_{\bar{p}} \ll v_e$, where $v_{\bar{p}}$ and v_e are the velocities of the antiproton and the electron, respectively. When the kinetic energy of antiproton is small enough so that the released electron can take away the major part of the antiproton's kinetic energy, the antiproton and the ionized atom are bound together in a state with a large principal quantum number n . The production process of an antiprotonic atom is qualitatively understood as follows: when an antiprotonic atom is formed, the energy conservation before and after the collision in the laboratory frame requires,

$$K_{\bar{p}} - \varepsilon_e = K_a + K_e - \varepsilon_{\bar{p}}, \quad (1.1)$$

where K_e and $K_{\bar{p}}$ are the kinetic energies, ε_e and $\varepsilon_{\bar{p}}$ the binding energies of electron and antiprotons, respectively. K_a is the recoil energy of the antiprotonic atom, considering that the electron is “oozing” out, one can safely assume that $K_e \sim 0$.

Because the momentum of the antiprotonic atom is practically that of the incident antiproton, one gets,

$$\varepsilon_{\bar{p}} = \varepsilon_e - \left(1 - \frac{m_{\bar{p}}}{m_a}\right) K_{\bar{p}}, \quad (1.2)$$

$m_{\bar{p}}$ and m_a being the masses of the antiproton and antiprotonic atom, respectively. In other words, the principal quantum number n of the adiabatically-formed atom is given by

$$n \approx \sqrt{\frac{\mu_{\bar{p}}}{m_e} \times \frac{\varepsilon_e}{\varepsilon_e - \kappa K_{\bar{p}}}}, \quad (1.3)$$

where m_e and $\mu_{\bar{p}}$ are the reduced masses, of the electron and antiproton, respectively, and $\kappa = A/(A+1)$ for a target of mass number A , that is, for atomic hydrogen $\kappa = 1/2$ and $\kappa \rightarrow 1$ for heavier targets. The antiproton n -value is thus a function of $K_{\bar{p}}$ only, and can be tuned from $n_{min} \sim \sqrt{\mu_{\bar{p}}/m_e}$ to infinity by increasing $K_{\bar{p}}$ from 0 to ε_e/κ , i.e., antiprotonic atoms are in high Rydberg metastable state.

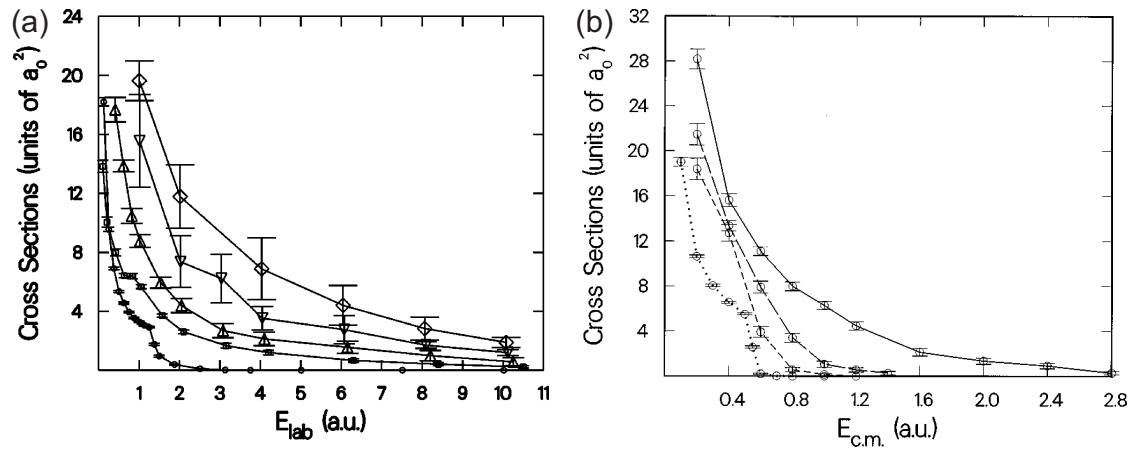


Figure 1.1: (a) Calculated protonium and antiprotonic atom formation cross sections by a quasi-classical calculation for H (dotted line), H₂ without rotation (short dashed line), H₂ with rotation (long dashed line) and H₂ with rotation and vibration (solid line). The circles are calculated values [23]. (b) Antiprotonic atom formation cross sections for He (circle), Ne (square), Ar (up triangle), Kr (down triangle), and Xe (diamond) by the FMD calculation [22].

The formation cross sections of antiprotonic atoms has been studied for various targets by Classical Trajectory Monte Carlo (CTMC) calculations taking into account the Pauli exclusion principle employing a fermion molecular dynamics (FMD) method [21] [22].

The dotted line in Fig. 1.1 (a) shows the formation cross sections of protonium ($\bar{p}p$) in $\bar{p} + H$ collision, which predicts that the formation cross section is finite when the incident antiproton energy is lower than ~ 0.5 a.u. in the center of mass system, i.e., 1 a.u. in the laboratory frame as is seen in Eq.(1.2).

In the case of molecular hydrogen, H₂, Cohen predicted that an antiprotonic molecule, $\bar{p}H_2^+$, is temporary formed, which then dissociates into an antiprotonic atom and an H⁰ atom or a proton and an electron [23]. In the case of molecular targets, no threshold of the collision energy is predicted. This is because the dissociated H⁰ atom can take care of excess momentum of incident antiproton, which is particularly the case when the molecular vibration is taken into account.

Figure 1.1 (b) shows that antiprotonic noble-gas atoms are formed even at relatively high impact energy. This is primarily due to multiple electron release processes, which

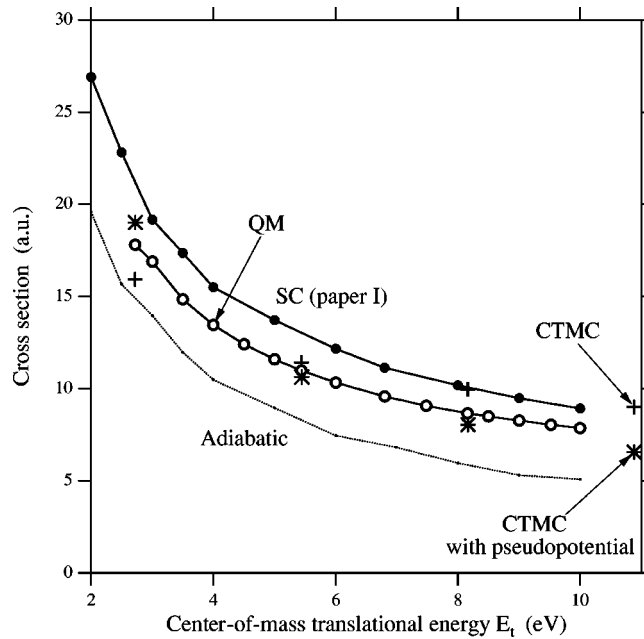


Figure 1.2: Calculated protonium formation cross section by full-quantum mechanical calculation [24] (circle). The result from the CTMC method (“+”) and that with the FMD (“*”) are also in the figure. The semiclassical (SC) results are taken from the reference [25]. The cross section obtained under the adiabatic assumption are shown.

effectively increase ε_e and accordingly increase the threshold energy.

Figure 1.2 compares a full-quantum calculation of protonium formation cross section with classical one. These results, which more or less show a similar behavior, ensure that the classical treatments are rather accurate in the present system.

1.2.2 Cold antihydrogen atoms

Antihydrogen ($\bar{p}e^+$) is the simplest antimatter. A couple of experiments using cold antihydrogen atoms to test CPT symmetry have been proposed, which includes not only high-precision laser spectroscopy but also ground-state hyperfine spectroscopy.

Schemes of antihydrogen synthesis

To synthesize antihydrogen atoms, the following recombination processes are considered to play major roles.

(1) Spontaneous radiative recombination [26]

It is the inverse photo emission process, which is described as



The reaction rate Γ_r is given by [27]

$$\Gamma_r = \frac{N_{\bar{p}}N_{e^+}\sigma_r v^*}{V} \propto \sqrt{\frac{1}{T^*}}, \quad (1.5)$$

where the number of antiprotons and positrons are $N_{\bar{p}}$ and N_{e^+} , respectively, which are confined in a volume V at temperature T^* (their relative collision velocity v^*).

(2) Three-body recombination [28]

The three-body recombination process is described as



The reaction rate Γ_t is given by

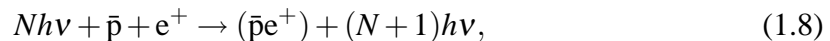
$$\Gamma_t \sim \left(\frac{N_{e^+}}{V}\right)^2 \left(\frac{1}{T^*}\right)^{\frac{9}{2}}. \quad (1.7)$$

The rate is inversely proportional to $T^{-9/2}$, growing much faster than the radiative recombination process with decreasing temperature.

Figure 1.3 shows examples of the recombination cross sections for both processes. It is seen that the three body recombination cross section plays the dominant role for a realistic positron density and temperature ranges.

(3) Laser induced recombination [7]

This is a variation of the radiative recombination, which increases the recombination rate by a laser stimulation.



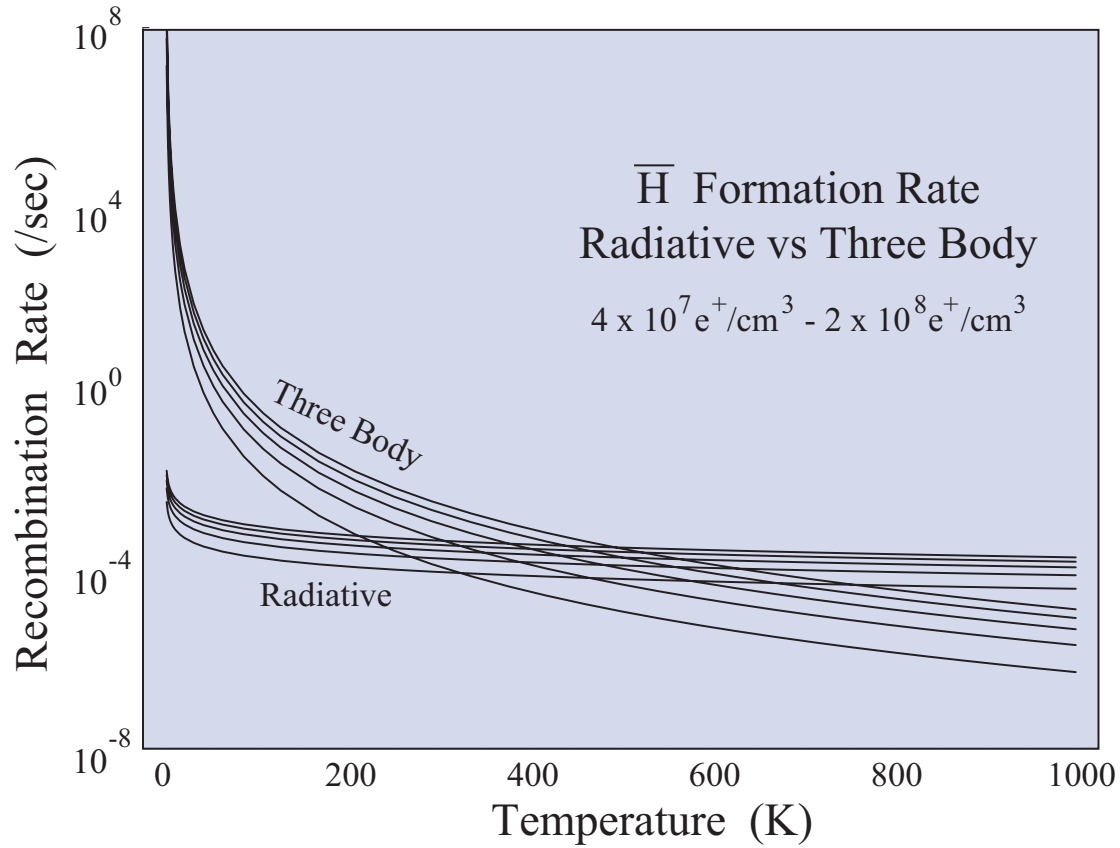
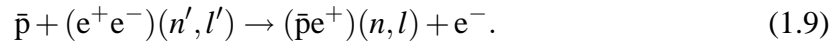


Figure 1.3: Antihydrogen atom formation rate for radiative recombination and three body recombination against various positron density, 4×10^7 , 6×10^7 , 8×10^7 , 1×10^8 and $2 \times 10^8/\text{cm}^3$.

which may increase the rate by a factor of 10–100 [7].

(4) Charge exchange collision with positronium [29]

This is a variation of the three body recombination where the third particle is an electron instead of positron, and positron and electron are bound together in an excited state, which is described as



Although the recombination cross section is many orders of magnitude larger than the abovementioned processes, it is quite difficult to prepare high density of positronium target because of its short life time. However, when the positronium is in high Rydberg states, the life time becomes longer and also the recombination cross section is larger than in proportion to n^4 [30][31].

Antihydrogen atom synthesis

Antihydrogen atoms were produced in 1996 at CERN [14] and in 1998 at Fermilab [15], in collision of relativistic antiprotons with gaseous target, where a positron in a virtual positron-electron pair creation was captured by a relativistic antiprotons. In the former case, 1.2 GeV antiprotons were injected on a Xe gas jet and nine antihydrogen atoms flying with relativistic velocity were detected. Unfortunately such high-speed antihydrogen atoms are not suitable for spectroscopy or anything.

In order to prepare somewhat cold antihydrogen atoms, a so-called nested trap scheme has been adopted by two groups, and in fact they had succeeded in synthesizing a large number of antihydrogen atoms in year 2002 [16] [17]. The nested Penning trap which is a variation of open-end cylindrical Penning trap, can confine positively and negatively charged particles simultaneously [32].

Figure 1.4 shows schematically the procedure to produce antihydrogen with the nested trap, which consists of a Penning trap for positrons and two Penning traps for antiprotons on both ends of the positron Penning trap. When antiprotons are given proper kinetic energy, they oscillate between the two Penning traps passing the positron area many times losing their kinetic energies via Coulomb scattering with positrons [33]. In both cases, positrons with energies of a few electronvolts were obtained by degrading megaelectronvolt positrons from a ^{22}Na source with a solid Ne moderator, which are then cooled by buffer gas and stored in a Penning trap [34].

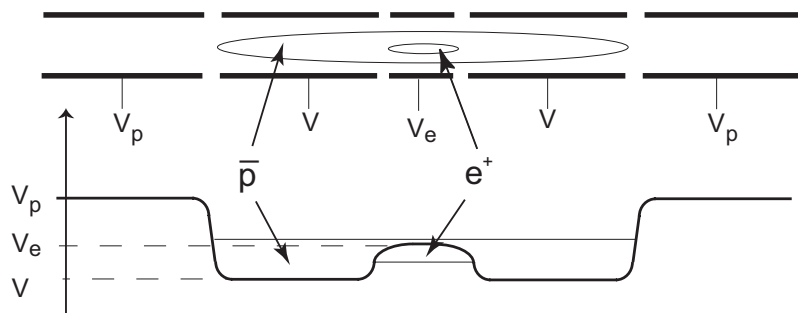


Figure 1.4: Nested Penning trap for synthesis of antihydrogen atom [7].

Antihydrogen trap

Because antihydrogen is a neutral atom, it is not trapped any more in an electromagnetic trap and drifts out of the trapping region, which eventually hits one of the trap electrodes. The antiproton and the positron constituting the the antihydrogen annihilate simultaneously emitting several energetic pions and two 511 keV gamma rays, respectively. Actually, the first report [16] confirmed the production of a large number of antihydrogen through monitoring this simultaneous annihilation from the same spot.

In order to confine antihydrogen atoms, several schemes other than the nested trap, which cannot trap neutral particles, have been proposed [35] [36] [37] [38]. Once antihydrogen is trapped and cooled, a high-precision laser spectroscopy becomes applicable, which would provide one of the most stringent CPT tests in a future. In the case of hydrogen atoms, the 1S-2S transition was measured with the accuracy as high as 10^{-14} [39], where 10^{13} hydrogen atoms at 4K were used.

Another possible CPT test is the comparison of the magnetic moments between proton and antiproton which had been discussed time to time [40]. The proton spin magnetic moment has been determined to the accuracy of 10^8 through measurements of a ground-state hyperfine splitting of hydrogen atom [41]. On the other hand, the magnetic moment of antiproton is known only with the accuracy of 10^{-3} through antiprotonic X-ray spectroscopy [42]. Recently, a measurement of the ground-state hyperfine splitting of antihydrogen atom has been discussed with a nested Penning trap in a split solenoid [43] and with a magnetic cusp trap [38].

The number of antiprotons available with the "thick" degrader methods is fairly limited although the number of positrons is getting quite reasonable for antihydrogen synthesis [34] [44] [45]. It is therefore quite important to develop a new scheme that can prepare a large number of cold antiprotons suitable for physics experiments of antihydrogen.

1.3 Charged particle trap

Charged particle trap is one of the most important key techniques of this work, where antiprotons should be confined and cooled. For confinement of charged particles, several trapping techniques have been known as summarized in Tab. 1.1. Although the optical trap is known for confinement of atoms and ions, it works only for particles with internal structure(s), and not applicable to antiprotons.

	advantage	disadvantage
Penning trap	harmonic	small volume
Cylindrical Penning trap with open-endcaps	harmonic free access to the center	small volume
Penning-Malmberg trap	large volume free access	rectangular short confinement time
Multi-ring trap	large volume free access no dependency on length	many cables
Paul trap	no field at the center	micromotion heating single particle

Table 1.1: Advantages and disadvantages of some traps for confinement of antiprotons.

The combination of static electric and magnetic fields are often used to trap charged particles. Figure 1.5 schematically shows a cross section of electrodes of such a trap.

When an electrostatic potential expressed as

$$\phi = \frac{\phi_0}{2\rho_0}(2z^2 - \rho^2), \quad (1.10)$$

is formed between the endcaps and the ring (see Fig. 1.5), the force on a particle with a charge q is given by,

$$\mathbf{F} = -q\nabla\phi \quad (1.11)$$

$$= \frac{\phi_0}{2\rho^2}(-4\mathbf{z} + 2\rho). \quad (1.12)$$

It is seen that the particle is trapped in the z -direction by the harmonic potential. The trapping in the ρ -direction is realized by two different methods.

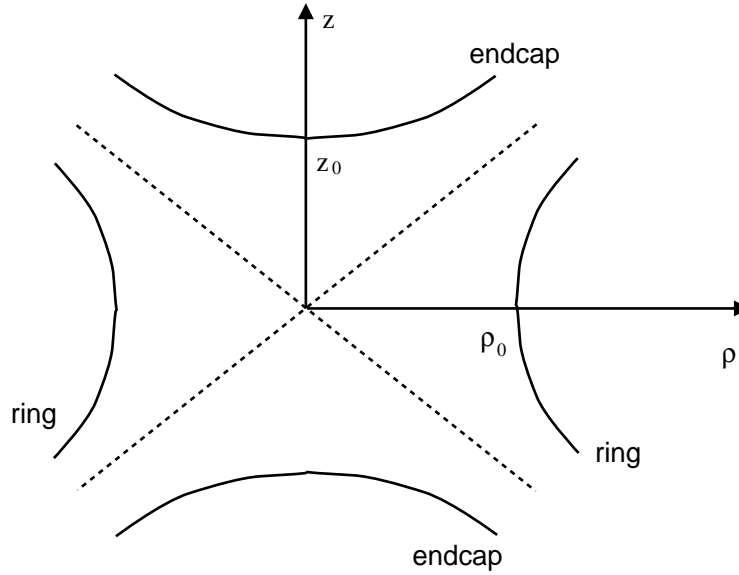


Figure 1.5: Cross section of electrodes of a charged particle trap.

In the case of the Paul trap [46], a radio frequency (RF) field

$$\Psi = U_0 + \psi_0 \cos \Omega t \quad (1.13)$$

is applied between the endcaps and the ring electrodes to trap charged particles, which effectively provides an attractive force on the charged particles independent of their charge polarities; the pseudo potential is given by,

$$\psi_{\text{pseudo}} = \frac{q}{4m\Omega^2} |\nabla \psi_0|^2. \quad (1.14)$$

However, a micromotion is superimposed on the particle motion due to the time-varying electric fields [46]. At the center of the trap where the fields are zero, the pseudo potential of the particle is minimum. When a single particle is trapped, it can be localized in the field-free region, which is ideal for laser spectroscopy.

Penning trap [47] with a static magnetic field applied along the z -direction generates a force given by

$$\mathbf{F} = -q\nabla\phi + q\mathbf{v} \times \mathbf{B}. \quad (1.15)$$

In this case, there is no mechanism to heat up the trapped particles, which is suitable

for high-resolution mass spectroscopy [48]. It is noted however that the introduction of charged particles into the trap is not easy.

In order to solve this practical but important difficulty, a cylindrical Penning trap has been developed using several cylindrical electrodes, which is suitable to introduce particles in the trap and at the same time allows to confine a large number of charged particles. When a quadratic electrostatic field like Eq. (1.10) is superimposed on a uniform magnetic field with its symmetry axis common to the z-axis, charged particles can be confined in the field (See App.B.1). One of the well-known stationary states has a uniform density and a spheroidal shape rotating with a uniform frequency ω_r , i.e., rigid rotor equilibrium (see App. C.3), when particles are cold enough to form a plasma [49]. When the number of particles are very large and the image charge induced is not negligibly small, the electric potential distribution of the open-end cylindrical trap [50] is deformed and does not give an equilibrium any more.

In a Penning-Malmberg trap [51], the generated potential, like square well, can not realize such an equilibrium condition. Furthermore Penning-Malmberg trap has a length dependent confinement feature of the plasma along the magnetic field axis [52]. On the other hand, the Multi-Ring trap (MRT) can prepare a harmonic potential using a train of many ring electrodes, compensating the image charge potential not only due to a small number of particles but also due to a large number of particles [53]. A large and long plasma can be settled in the MRT much more stably than the Penning-Malmberg trap.

Advantages and disadvantages to confine a large number of antiprotons for several traps are summarized in Table 1.1.

1.3.1 Antiproton confinement in the trap

Antiproton trapping technique has been developed by the Harvard University group as was described in Sec. 1.1.1, which employed the combination of a "thick" degrader foil and a cylindrical Penning trap. Although the trapping efficiency is not great such as 10^{-4} , this has been the unique technique, which could realize trapping of antiprotons. In fact, the

charge to mass ratio of the antiproton was determined to a precision of 9×10^{-11} [13] using antiprotons trapped by this method. It is noted that a single antiproton is necessary to make such a measurement, i.e., the "thick" degrader method is eventually a suitable technique for the above purpose. Later on, studies with trapped antiprotons had been extended for other subjects, particularly the antihydrogen synthesis and high precision spectroscopy of antihydrogen. Although a large number of antiprotons are necessary for the latter subjects, there have been no innovation regarding the scheme of antiproton trapping (see e.g., [16] [17] and [54]).

Gabrielse et al. (PS196 collaboration) captured antiprotons in a cylindrical Penning trap for the first time on 1986 at CERN LEAR [11], where "thick" ($\sim 70\,000\mu\text{g}/\text{cm}^2$) energy degrading foils were used for further deceleration of ~ 5 MeV antiprotons. Therefore most of the injected antiprotons, i.e., more than 99%, annihilated in the foil. The maximum number per one AD shot (containing 3×10^7 antiprotons of ~ 5 MeV) has been 2.5×10^4 [44]. Gabrielse et al. also succeeded in keeping 10^3 antiprotons in their trap for two months [55], which revealed that the life time of antiproton is longer than 3.4 months. The PS200 collaboration once stored $\sim 1 \times 10^6$ antiprotons by trapping one LEAR shot that contained more than 10^9 antiprotons. In any case, the trapping efficiency of the "thick" degrader scheme has been 10^{-3} or so at the maximum. The energy of trapped antiprotons were measured by time-of-flight measurement. Gabrielse et al. demonstrated transportation of antiprotons in the strong magnetic field to measure the temperature of the antiproton cloud with time-of-flight technique [11].

In the present work, we have developed a completely new scheme of antiproton accumulation combining the AD, the RFQD (radio frequency quadrupole decelerator), and the MRT, and proved that the efficiency was improved by 50 times or more. With this large number of antiprotons in the MRT together with electrons, it becomes possible to monitor the electron plasma's electrostatic mode. In fact, we have succeeded in nondestructive monitoring the cooling process of antiprotons in the trap, which was performed for the first time. The details are described in following Chap. 3 and 4. To perform antipro-

tonic atom formation experiments, cold antiprotons should be extracted and transported from the strong magnetic field to the “non-”magnetic field region, which have never been performed. Chapter 5 describes the beam transport system and first demonstration of ultra-slow antiproton transport.

Chapter 2

Apparatus

A sequential combination of the AD (Antiproton Decelerator), the RFQD (Radio Frequency Quadrupole Decelerator), the MRT (Multi-Ring electrode Trap), and the transport beam line were used to produce ultra-slow antiprotons.

Figure 2.1 shows a schematic diagram of the accelerator complex at CERN, where

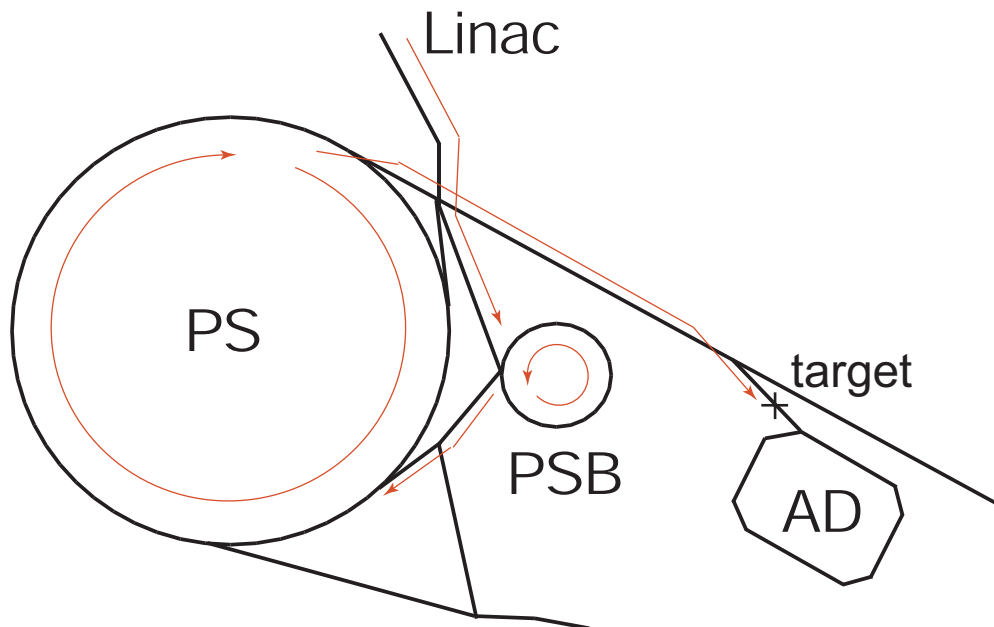


Figure 2.1: The PS-complex at CERN. The proton beams are injected from the Linac to the PS via PSB (PS Booster). The beam accelerated to $26 \text{ GeV}/c$ is incident on the target area and produces antiprotons.

Machine	Antiproton kinetic energy
from target area	2.7 GeV
AD	5 MeV
RFQD	10–120 keV
MRT	< 10 eV
Extraction beam line	10–500 eV

Table 2.1: Scheme for production of ultra-slow antiprotons

3.5 GeV/ c antiprotons are produced, collected and injected into the AD. Table 2.1 summarizes the energy of antiprotons handled in each stage. The antiprotons collected in the AD are cooled and decelerated down to 100MeV/ c (5.3MeV). Antiprotons from the AD are then decelerated by the RFQD down to 10–120 keV, which are eventually injected in the MRT.

Antiprotons in the MRT were cooled with electrons preloaded in the MRT. They were then extracted from the MRT as a beam with the energy ranging 10–500 eV. For transportation of the ultra-slow antiprotons a special transport beam line was designed and constituted for atomic collision experiments described in App. A.

In order to monitor antiprotons during their transportation, various detectors were developed and used, which were secondary emission beam profile monitors, a delay line position sensitive detector combined with MCPs (microchannel plate), and track detectors consisting of two scintillator bars.

2.1 The Antiproton Decelerator

Antiprotons of gigaelectronvolt-scale energy are decelerated at the CERN Antiproton Decelerator (AD) using stochastic- and electron-cooling techniques [56]. The AD ring and hall layout is shown in Fig. 2.2. Figure 2.3 schematically shows the AD deceleration cycle: A 26 GeV/ c beam of 1.5×10^{13} protons from the PS (Proton Synchrotron) is injected in an Ir block, yielding 4×10^8 antiprotons with their peak energy at 3.57 GeV/ c . The antiprotons are then collected and stochastically cooled to $5 \pi \text{mm} \cdot \text{mrad}$ in the transverse planes

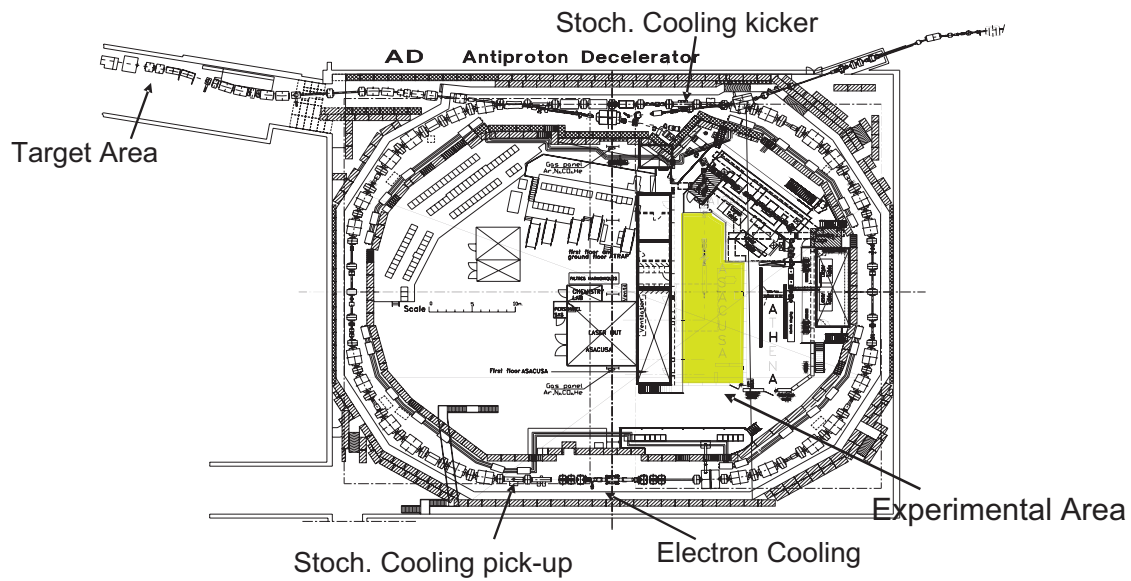


Figure 2.2: The AD ring and hall layout. In this ring, antiprotons are collected, cooled and decelerated. Filled region is the experimental area for the present work.

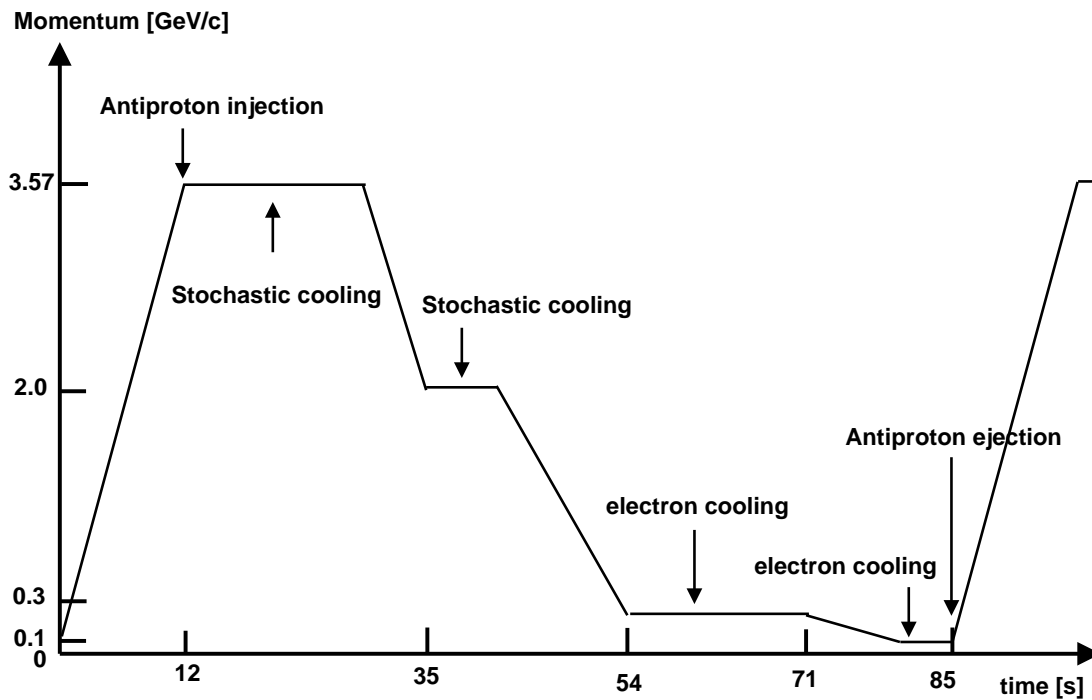


Figure 2.3: AD deceleration cycle.

and a momentum spread of 0.1% in the AD. The beam is then decelerated to 2.0 GeV/ c , which is again stochastically cooled. Then the beam is decelerated to 300 MeV/ c , where the transverse emittance is grown to $33 \pi \text{mm} \cdot \text{mrad}$ and the momentum spread to 0.2%. The 300 MeV/ c antiprotons are electron-cooled, decelerated, and electron-cooled again, eventually to obtain 100 MeV/ c (5.3 MeV kinetic energy) antiprotons with transverse emittance of $1 \pi \text{mm} \cdot \text{mrad}$ and momentum spread of 0.1%. The overall time duration of the AD cycle was 85 s at the shortest, and it varied slightly depending on the so called super-cycle of the PS machine.

2.2 The Radio Frequency Quadrupole Decelerator

A Radio Frequency Quadrupole Decelerator (RFQD) was designed and constructed to further decelerate antiprotons, while an RFQ accelerator is usually used as an injector to accelerate particles. In the present work on the other hand, to the contrary, the same system is operated to decelerate particles [57] [58].

The RFQD is located between the MEBT (medium energy beam transport line) and LEBT (low energy beam transport line) as is shown in Fig. 2.4. The MEBT is composed of beam buncher (“1” in Fig. 2.4), two magnetic quadrupoles lenses (“6” and “7”), two horizontal and vertical steering dipoles (“8” and “9”), two beam diagnostic boxes (“10” and “11”), and the energy corrector (“13”).

A bunching cavity (“1”) installed 6.15 m upstream of the RFQD shapes the 100 ns antiproton pulse into a train of 20 micro-pulses, each 0.3 ns long with a separation $\Delta t = 5$ ns, which comes from the frequency of the RF, 202.5 MHz. Because the distance between the buncher and the RFQD itself was 6.15 m, the buncher phase of 2π means about 60 keV energy difference.

Each of two beam diagnostic boxes contains two removable scintillator plates called watchdogs, one with 5 holes and the other without holes. The images of the beam spot on the watchdogs were monitored by CCD cameras and digitized, which were used to evaluate the beam parameters like position and radius. Examples of such beam images are shown

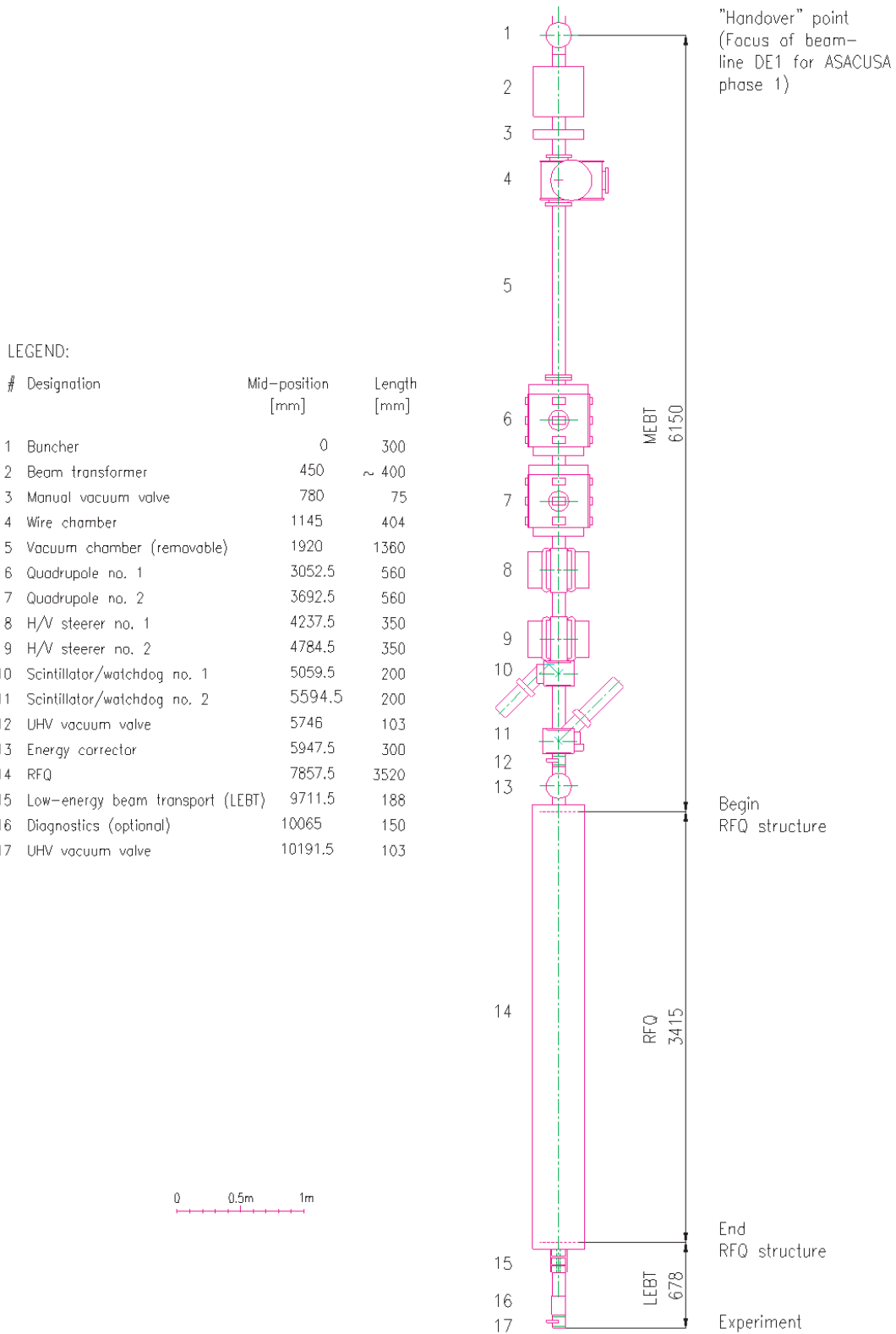


Figure 2.4: Beam line from the AD to the superconducting solenoid including the RFQD. The antiproton beam is injected from the upper side in this figure.

Emittance [$\pi\text{mm}\cdot\text{mrad}$]	Upstream Aperture ϕ [mm]	Downstream Aperture ϕ [mm]
10.0	21.0	14.0
5.8	25.5	10.6
3.3	12.0	8.0
1.9	9.2	6.1
1.1	7.0	4.7

Table 2.2: Upper limit of the beam emittance estimated for various combinations of hole sizes.

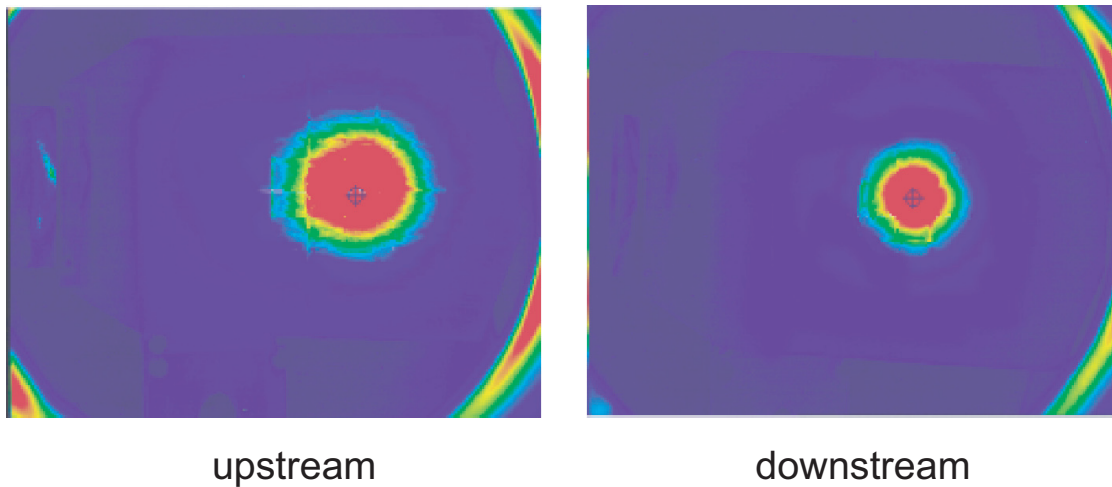


Figure 2.5: Example of beam images at the watchdog screens.

in Fig. 2.5. Estimated values of the maximum beam emittance for scintillator plates with various hole diameter are given in Table. 2.2. When the beam was tuned as described in the following Chap. 3.2, the beam passed through small holes as shown in Fig. 2.6, where the beam was focused by the quadrupoles (“6” and “7”).

The energy corrector cavity (“13”) is installed at the entrance flange of the RFQD to compensate for this DC potential difference between the RFQD grounded cover and the floated inner structure. Because the DC bias for varying the output energy not only affects the output beam energy itself but also shifts the input energy.

Figure 2.7 shows the structure of the RFQD. All assembly housed in a cylindrical tank located between the upstream diagnostics (a part of the MEBT) and the LEBT. The RFQD consists of 3.5-m long, four-rod electrodes producing an average decelerating field

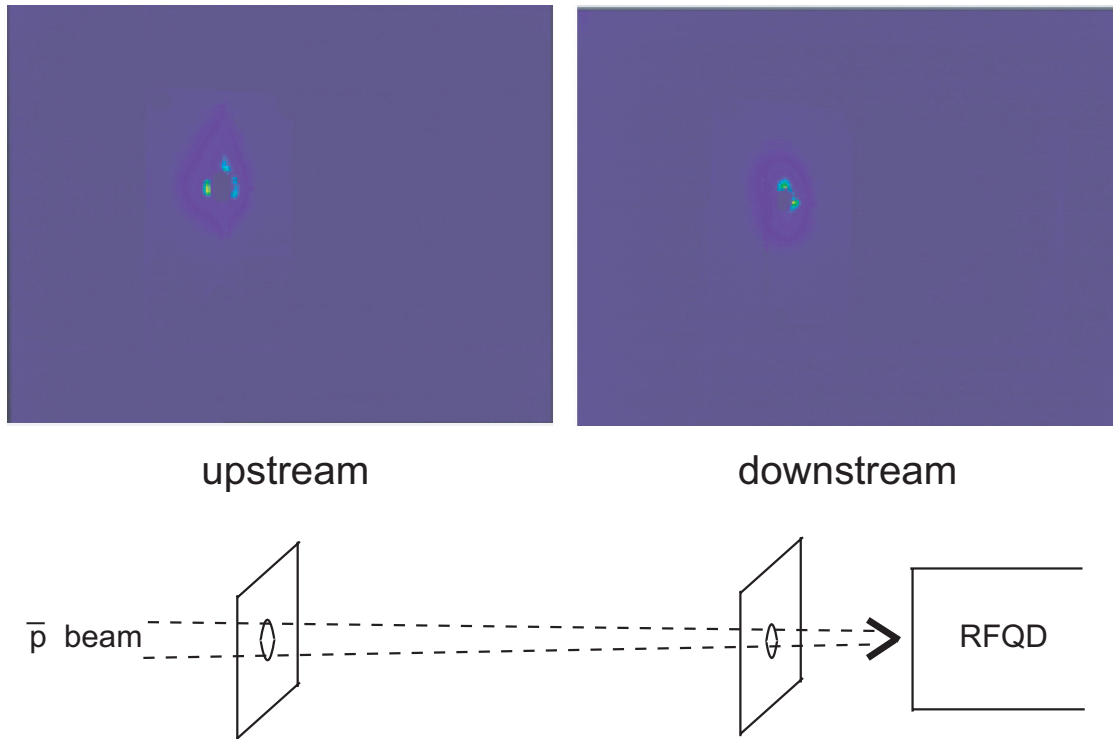


Figure 2.6: Example of beam image at scintillators with the smallest hole combination with schematic figure of the beam transport.

$E \approx 2 \text{ MV/m}$ at frequency $f = 202.5 \text{ MHz}$. The four rods are mounted at $\pm 45^\circ$ in a symmetric, ladder like RF resonating and supporting structure (Fig. 2.8). The ladder is composed of 34 RF cells with a total length of 3.415 m and is held in place by ceramic insulators (Fig. 2.8).

The RF applied on the four rods creates a transverse quadrupole electric field providing alternating gradient focusing of the beam. The longitudinal field component is produced by sinusoidal shape of the electrodes. By this longitudinal electric field modulation the injected antiprotons are decelerated from 5.3 MeV down to 63 keV. Although the RFQD is in principle a fixed-energy decelerator, the energy of antiprotons was made variable from $\sim 10 \text{ keV}$ to $\sim 120 \text{ keV}$ by biasing the whole assembly.

The RFQD was tested using a proton beam at the tandem accelerator, Aarhus University, and the deceleration efficiency obtained was about 45% [59]. The remaining fraction undergoes no or little deceleration.

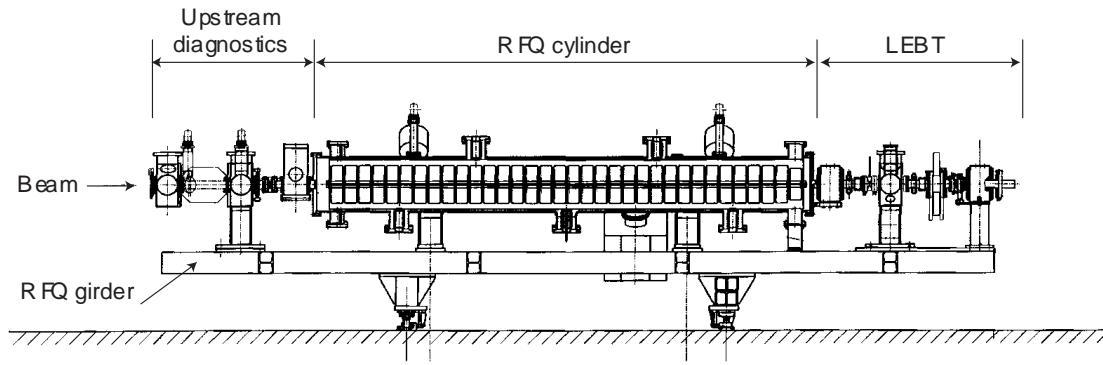


Figure 2.7: The structure of RFQD.

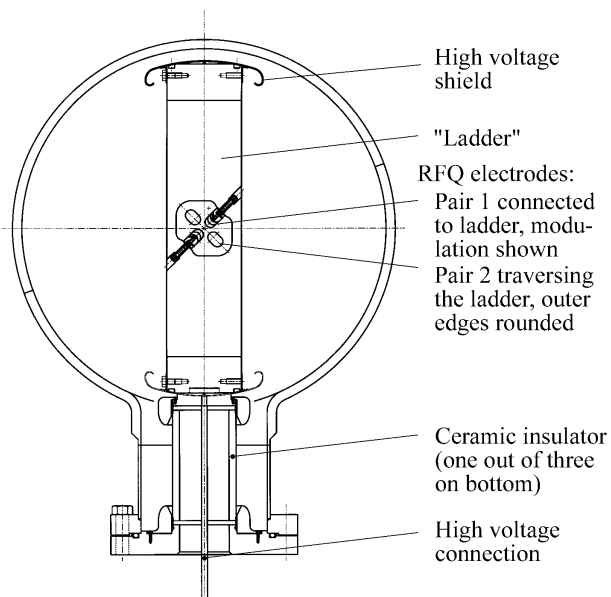
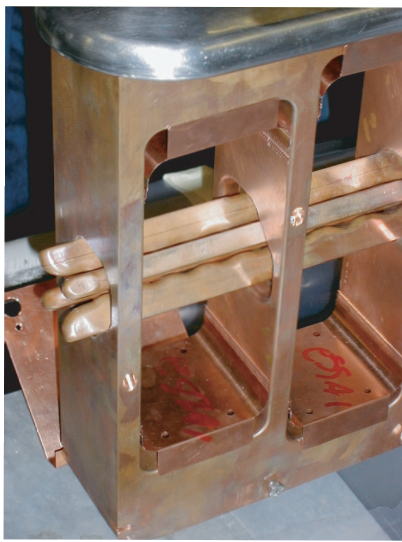


Figure 2.8: Picture of the four-rod structure (left) and cross section of the RFQD (right) [59].

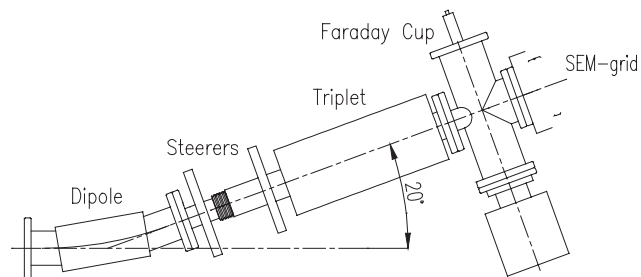


Figure 2.9: Layout of the RFQD spectrometer line

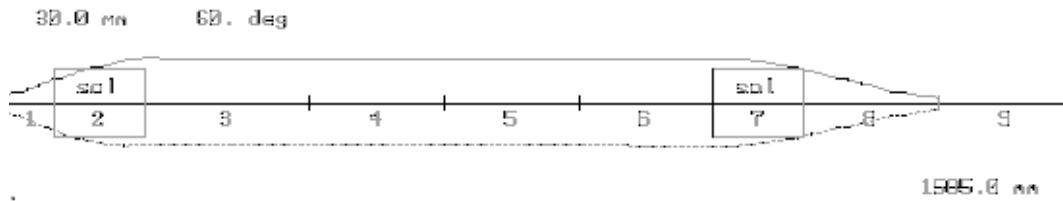


Figure 2.10: Calculated antiproton beam envelop in two LEPT solenoids. The position of $z = 0$ is the exit of the RFQD.

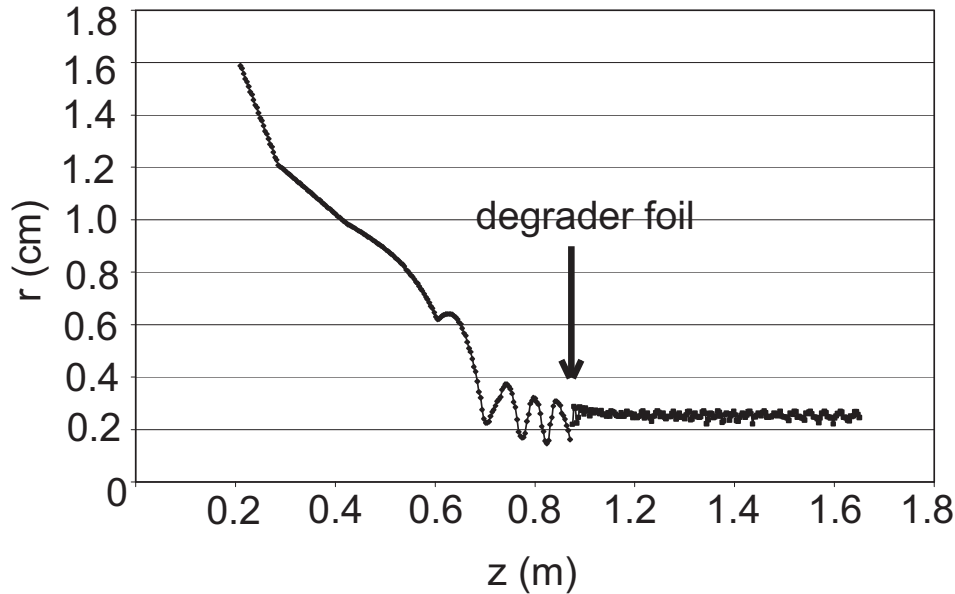


Figure 2.11: Calculated antiproton beam envelope injected to the superconducting solenoid. The position of $z = 0$ is the exit of the RFQD.

In order to assess the RFQD performance at CERN, an additional spectrometer line (shown in Fig. 2.9) has been set downstream of the LEPT. It is comprised of a 20° bending magnet (dipole), a pair of steerers, a quadrupole triplet, a Faraday cup and a multi-wire profile monitor. This spectrometer line permits to transmit an energy-selected antiproton beam. The efficiency was measured as the ratio of the number of decelerated particles which was counted by an activation of a thin Al foil at the end of the spectrometer line to the number of antiprotons in the AD ring just before ejection at 5.3 MeV [59]. The deceleration efficiency was initially about 25% [59], and had recently improved up-to 30% [60] primarily because the beam quality from AD got better.

The LEBT consists of two pulsed solenoids, two horizontal and vertical beam steering dipoles, and two secondary emission beam profile monitors (See Sec. 2.5). The trajectories of antiprotons from the RFQD to the superconducting solenoid via the LEBT were calculated to optimize the beam transport parameter [61]. The envelope of the optimized trajectories is shown in Fig. 2.10, where the first pulsed-solenoid makes a diverging beam from the RFQD parallel and then the second pulsed-solenoid focuses the beam at the entrance of the superconducting solenoid. In the superconducting solenoid the injected beam is focused around 2.5 mm in radius by the LEBT solenoid and the magnetic field of the superconducting solenoid itself as shown in Fig. 2.11.

2.3 Antiproton trap

The antiprotons transported and focused by the superconducting solenoid are finally injected in the MRT via thin degrader foils. In the MRT, the antiprotons were further cooled to sub-electronvolt with preloaded electrons, which cool themselves via synchrotron radiation.

Various techniques have been developed to cool charged particles. A so-called buffer gas cooling has been well known as an efficient and handy cooling technique of charged particles such as positrons [62] and radioactive ions [63] [64] [65]. In the case of the antiprotons however, they will annihilate via antiprotonic atom formation as soon as they are cooled, i.e., the buffer gas cooling method is not applicable for antiprotons. Although the laser cooling method can cool atoms and ions down to a microkelvin range without any buffer gas, it works only for particles with internal structure(s), and not applicable to antiprotons. On the other hand, the electron cooling is suitable for antiprotons [66]. Antiprotons can coexist with electrons which lose their energy by synchrotron radiation in a strong magnetic field. As is discussed in Sec. 1.3, a Multi-Ring trap (MRT) [53] consisting of a number of electrodes was chosen for confinement of electrons and antiprotons, because

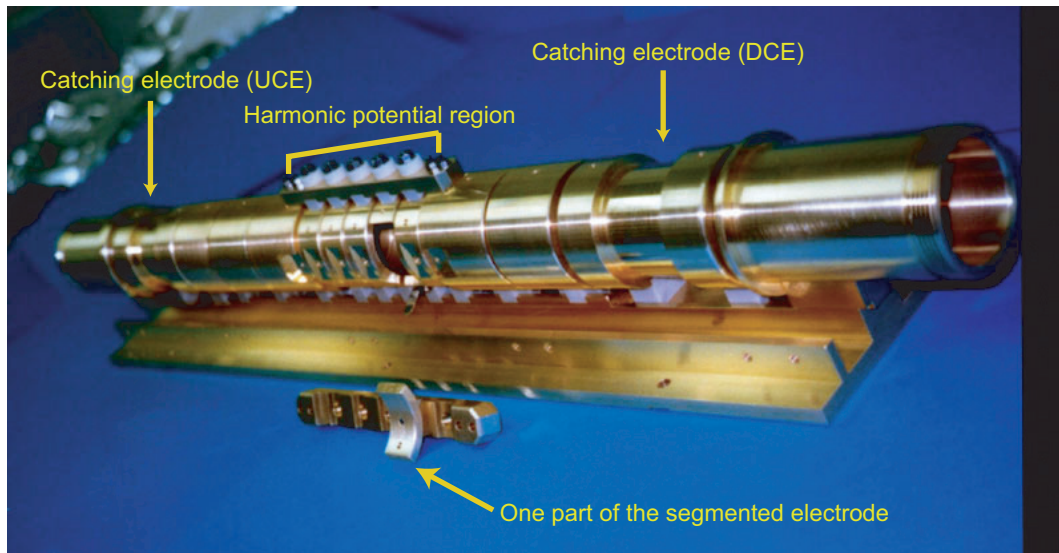


Figure 2.12: Picture of the MRT.

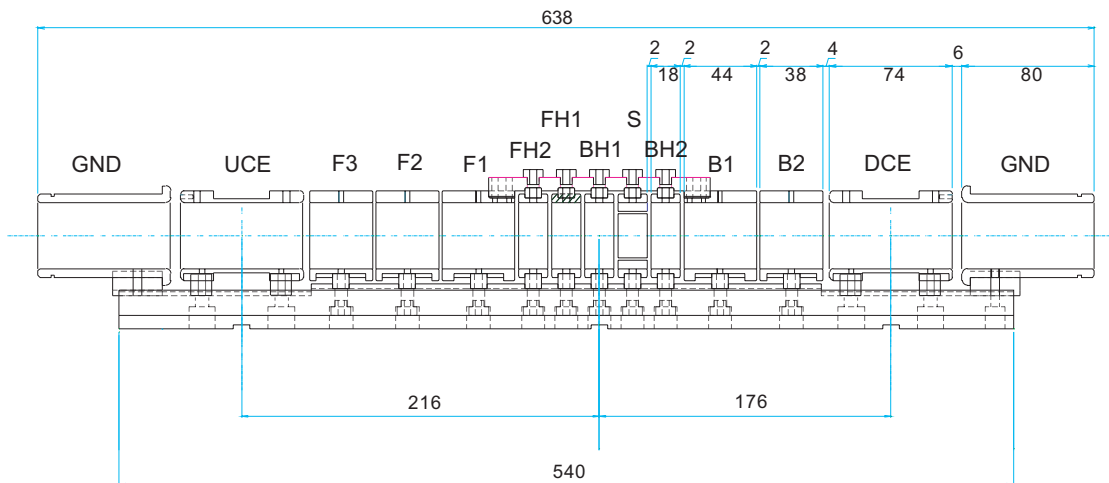


Figure 2.13: MRT electrodes.

it can stably confine a large number of particles.

2.3.1 Multi-ring trap

Figure 2.12 is a photo of the MRT. Figure 2.13 shows the drawing of the MRT used in the present research which consists of 14 ring electrodes with the inner diameter of 40 mm and its total length is 638 mm. All the electrodes were machined with an accuracy of $10\ \mu\text{m}$, which were configured on a CuBe plate machined with an accuracy of $20\ \mu\text{m}$. The electrodes on both ends shown as two “GND” were grounded. High-voltages were applied to

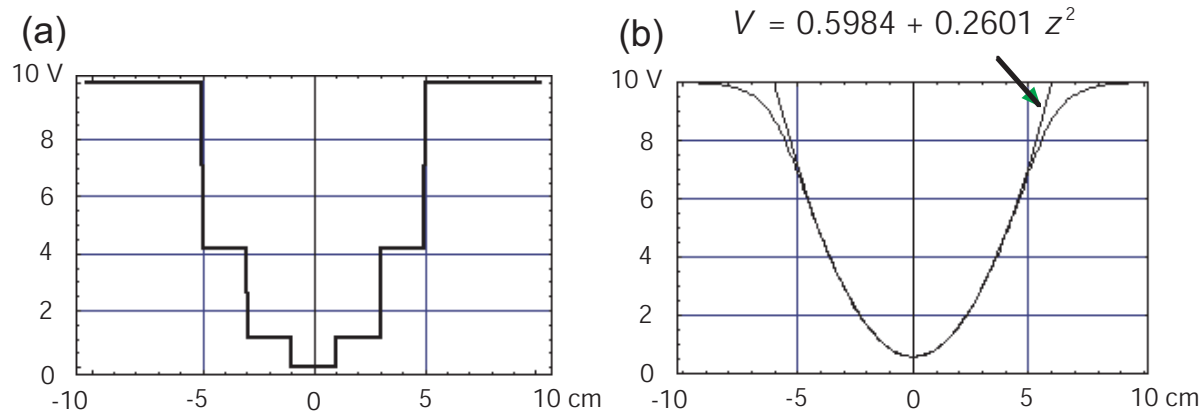


Figure 2.14: (a) Potential given at the electrodes surface of the MRT. (b) Potential along the trap axis and the fitting quadratic function.

the UCE (upstream catching electrode) and DCE (downstream catching electrode) to catch energetic antiprotons from the RFQD via the degrader foils. The five electrodes, FH2, FH1, BH1, S and BH2, were assembled with particular care to form precise harmonic potential for stable antiprotons confinement. Because the harmonic potential can compensate the image charge effects, the plasma in the MRT is confined more stable than in a square well potential. Such trapping potential is generated by the five electrodes. In the Fig. 2.14 (a), the potentials applied on the five electrodes are shown. Figure 2.14 (b) shows that the superposition of the calculated potential on the axis of the MRT and the fitting by a quadratic function. One of them, S, is azimuthally segmented into four to apply a rotating electric field to control radial distribution of the trapped charged particles (See App. B.2). In Fig. 2.12, one of the segmented electrode is disassembled. The position of the BH1 which corresponds to the center of the harmonic potential well was 10 cm downstream from the center of the superconducting solenoid.

In the MRT, charged particles are axially confined by electrostatic field and radially by magnetostatic field as was explained in App. B.1. When a large number of particles are confined, the space charge dominates. Nevertheless charged particles cloud, i.e., nonneutral plasma, is confined stably for a long time [67], that is known as rigid rotor equilibrium (See App. C.3).

2.3.2 Superconducting solenoid

The superconducting solenoid has its length of 1.8 m and the diameter of 22 cm, which yields a uniform magnetic field as high as 5 T with a uniformity within $\pm 0.5\%$ over the region of 1100 mm (length) \times 100 mm (diameter). The bore tube which houses the MRT has the diameter of 164.5 mm with a uniformity of less than 10 μm . The inner wall of the bore tube can be cooled down to several kelvin so that the vacuum around the MRT is low enough to avoid annihilation of antiprotons with residual gases.

Whenever the non-parallel component of electric field to the magnetic field exists, charged particles move with a constant velocity in the plane normal to the magnetic field, i.e., $\mathbf{E} \times \mathbf{B}$ drift. The bore tube is connected to the end flanges via nested bellows, so that it can be moved ± 2 mm with 1 μm step. This figure permits the alignment of the MRT axis to the axis of the transport beam line, to minimize this drift.

The cryostat consists of two parts, a main large container of liquid helium above the solenoid and a smaller one around the coil, whose total volume is 330 l.

2.3.3 Energy degrading thin foil

The vacuums at the LEBT and at the MRT were around 10^{-9} Torr and better than 10^{-12} Torr, respectively. The latter value is essential to avoid annihilation of antiprotons during trapping and cooling [11]. Because the annihilation cross section of antiproton is the same as the formation cross section of antiprotonic atom. When antiprotons were trapped in, the bore tube was cooled to below 10 K and the residual gas was H_2 or He. As is seen in Fig. 1.1 [22], the formation cross section of antiprotonic helium is about 2×10^{-16} cm^2 at the antiprotons temperature of 1000 K (≈ 0.1 eV). As the required life time of antiproton in the MRT is ~ 100 s, the pressure should be less than 10^{-12} Torr. Therefore, it is essential to isolate the trap vacuum from the LEBT vacuum, which was actually realized by preparing double PET (polyethylene terephthalate) foils of 90 $\mu\text{g}/\text{cm}^2$ each at 70 cm upstream from the center of the MRT.

The energy of antiprotons from the RFQD were tuned so that the energy is high enough

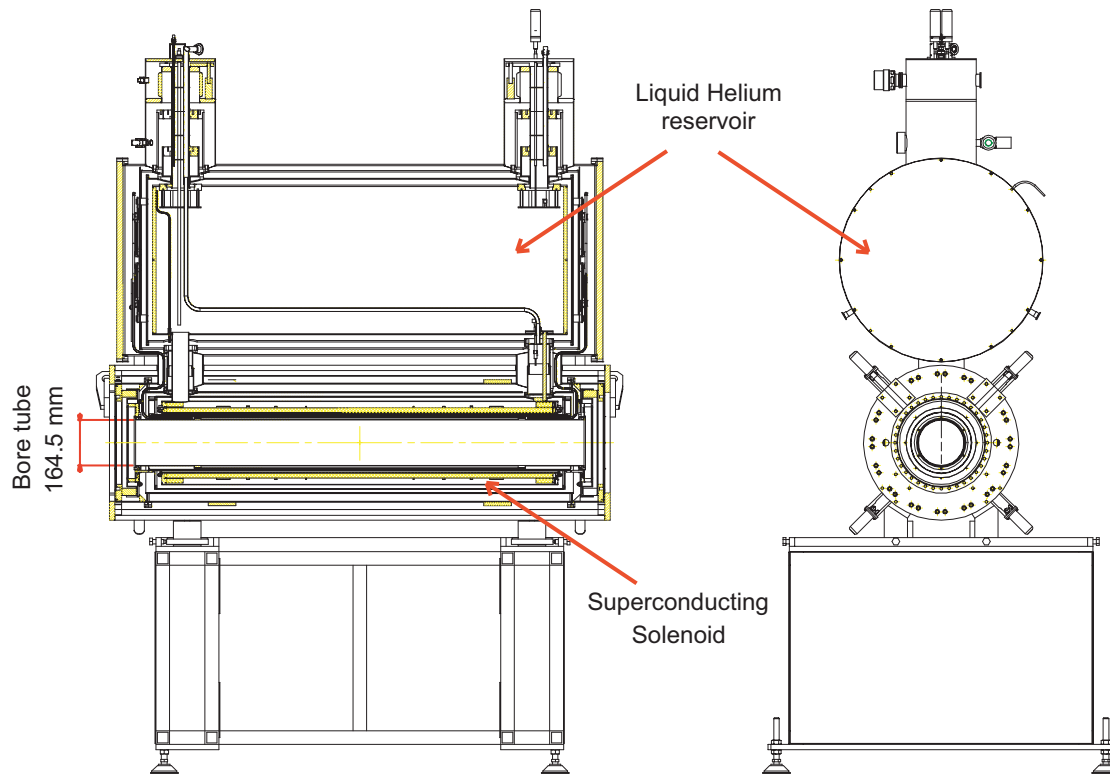


Figure 2.15: Design of the superconducting solenoid with liquid helium reservoir.

to pass the degrader foils and at the same time is low enough to be captured by the UCE and DCE biases, which are 10 kV.

As is discussed later, thin metal strips were evaporated on the foil, which were used as a 2-dimensional profile monitor of the incoming antiprotons (See Sec. 2.5.1).

2.3.4 MOS-FET high-voltage transistor switch

For an efficient confinement of antiprotons, the UCE high-voltage bias should be turned on within a short time with a high precision. This is realized with a MOS-FET high-voltage switch, a schematic circuit of which is given in Fig. 2.16. The pulse height was 10 kV, so that the antiprotons whose longitudinal energies were less than 10 keV were captured by the high-voltage potential. After passing through the first ring (UCE, see Fig.2.13), initially grounded, the injected antiproton pulse proceeded along the MRT axis to the position of the last one (DCE), which being biased at -10 kV and returned to the first electrode. The trap was closed around the pulse by a switch which changed bias of this upstream electrode

to -10 kV before the first antiprotons in the pulse reached it on their return trip.

The antiproton beam length injected from the AD is about 100 ns, and the antiproton velocity at 10 keV is about 0.14 cm/ns. The distance between UCE and DCE is 31.8 cm, so that the traveling length of antiprotons reflected at DCE is 63.6 cm. For catching antiprotons, the rising time of the fast high-voltage switch should be shorter than $350 \text{ ns} \approx 63.6 \text{ cm}/(0.14 \text{ cm/ns}) - 100 \text{ ns}$. In this experiment, it was about 300 ns as shown in Fig. 2.17.

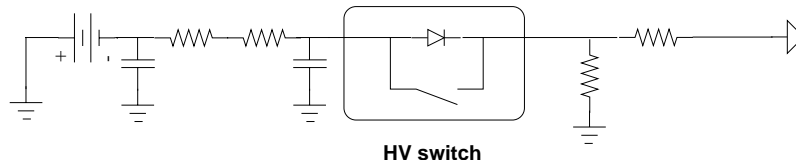


Figure 2.16: Circuit diagram of high-voltage transistor switch

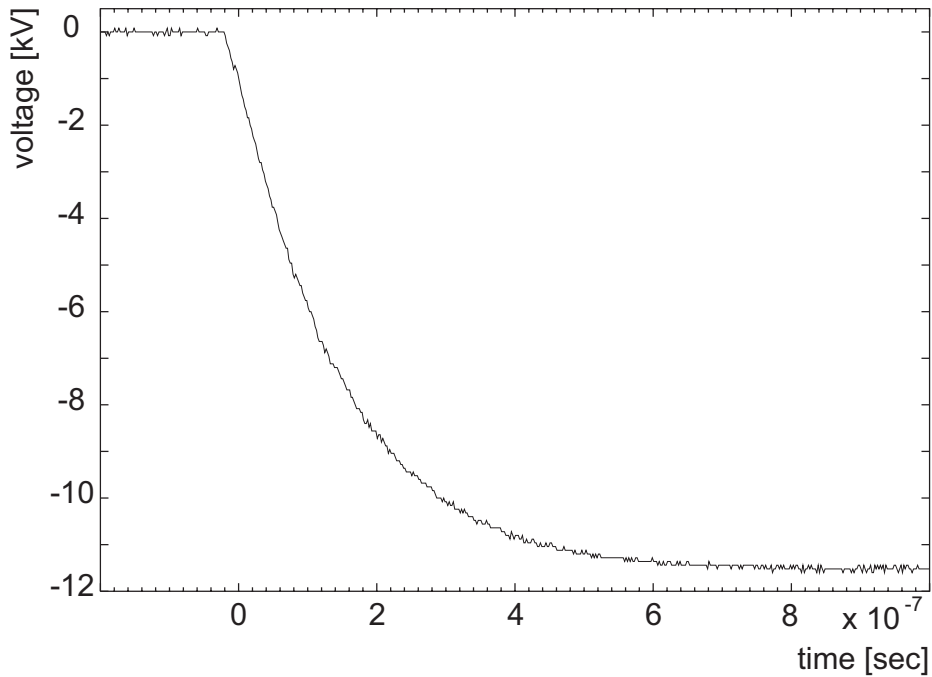


Figure 2.17: Rising time of the fast HV switch.

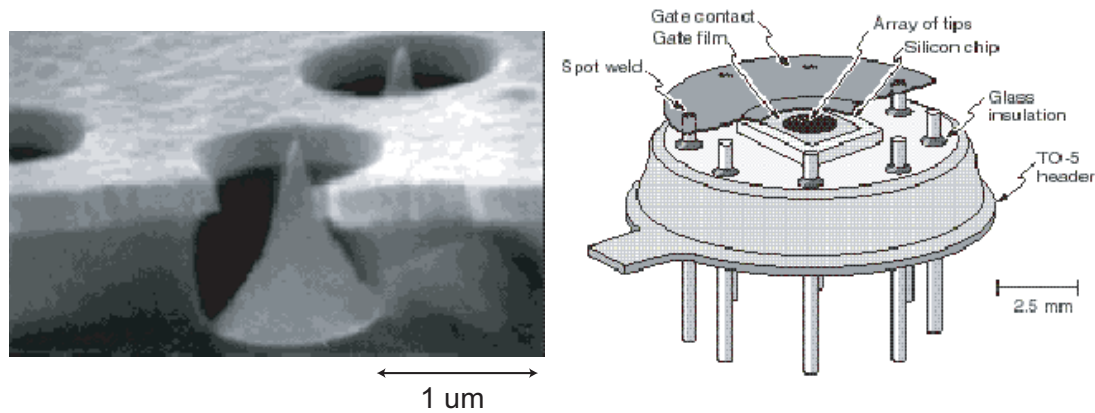


Figure 2.18: SEM micrograph of Spindt emitter array (left) and cutaway view of cathode mount (right).

2.3.5 Electron emitter

The injected antiprotons are cooled by collisions with preloaded electrons in the MRT. In the present study, a Spindt type field emission array shown in Fig. 2.18 [68] was used as the electron emitter. The emitter was mounted on a linear feedthrough 95 cm downstream from the center of the MRT and 4 cm off axis from the MRT axis, where the magnetic field strength was a few tens millitesla when the superconducting solenoid was energized to 2.5 T. The radius of the electron plasma containing $(1-3) \times 10^8$ electrons was about 5 mm.

2.4 Transport beam line

The transport beam line was specially designed to efficiently transport ultra-slow antiprotons from the MRT to an experimental chamber without affecting the vacuum in the MRT.

The atomic collision experiments under consideration will use a gas jet (See App. A) with its density as high as $10^{13}/\text{cm}^3$, which guarantees the reaction rate of 0.1% or so. With a reasonable pumping system, the pressure in the target chamber becomes 10^{-6} Torr in the present case. On the other hand, the pressure around the MRT should be kept less than 10^{-12} Torr because the survival life time of antiprotons against annihilation with the residual gas should be longer than the time necessary for cooling and manipulation of antiprotons in the MRT, which is typically several tens of seconds (See Sec 3.4.3).

Considering the above conditions, the requirements of the transport beam line are summarized as follows:

1. The low energy antiproton beam should be transported from the MRT in the strong magnetic field to the target area with a high efficiency.
2. The beam size at the target position should be less than several millimeters.
3. The pressure difference between the trap area and the target area should be larger than six orders of magnitude.
4. The beam energy at the target should be variable from 10 eV to 1000 eV.

In order to maintain a pressure lower than 10^{-12} Torr in the trap region while the pressure in the target chamber is around 10^{-6} Torr, the transport beam line for ultra-slow antiprotons is equipped with a three stage differential pumping system.

Extraction of charged particles from the strong magnetic field has difficulties since the trajectories tend to follow the field lines, which causes strong divergence. To satisfy the above requirements, high transport efficiency and a large pressure difference, the configuration of ion optics was surveyed employing computer simulations [69]. It was found that the antiproton cloud in the MRT with a cylindrical shape of 2 mm in diameter can be transported keeping the pressure difference of six orders of magnitude. Figure 2.19 shows the optimized configuration, which consists of two sets of x and y deflectors, two Einzel lenses (L1 and L2), and one asymmetric lens (L3) (Fig. 2.20 is a picture of the variable aperture consisting of a lens). Five gaps for three gate valves (GV1–3) and two beam profile monitors (MCP1 detector and wire chamber detector) are also prepared, where turbomolecular pumps (TMP 400 l/s and 1000 l/s) are connected for differential pumping.

As was discussed in Sec. 2.2 and shown in Fig. 2.11, the radius of the antiproton cloud in the MRT is simulated to be 2–3 mm. Therefore the expected extraction efficiency from the MRT is $\sim 25\text{--}35\%$. When the radial distribution of antiproton cloud in the MRT is

compressed either by the rotating wall or the sideband cooling method (See Sec. 5.3 and App. B), the efficiency will be improved considerably.

As is expected the transverse energy of the antiproton cloud in the MRT has only a minor effect on the final beam parameters, but the initial radius of the cloud plays dominant role [69].

The beam transport simulation revealed that the antiproton beam of 10–1000 eV at the target chamber can be transported with a high efficiency.

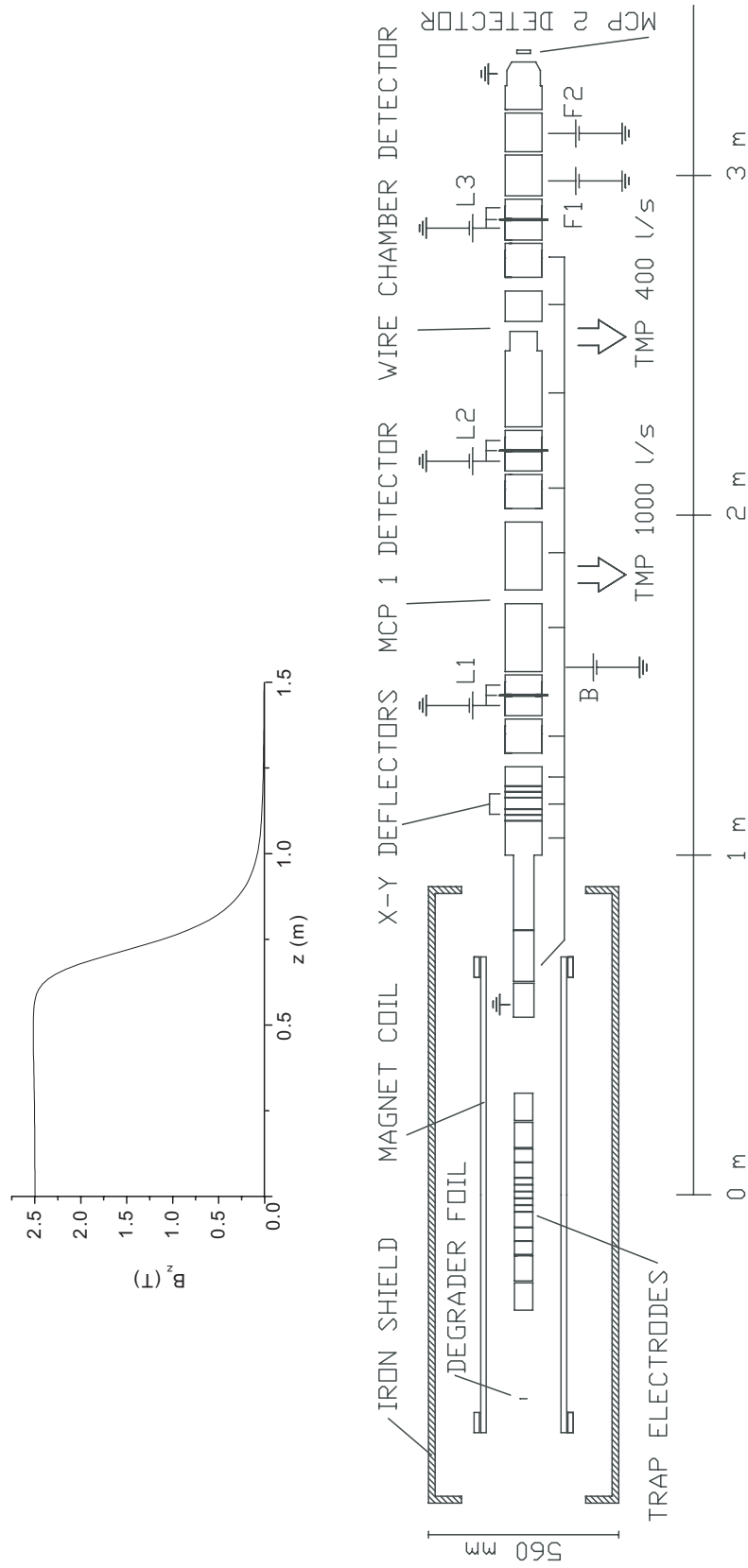


Figure 2.19: Design of the transport beam line. The calculated magnetic field is also shown at 2.5 T. L1–3: electro static lens, TMP: turbomolecular pump.



Figure 2.20: Picture of the variable and floatable aperture.

2.5 Detection system

To monitor the beam profile of antiprotons and to detect the annihilation position of antiprotons, five different kinds of detectors were prepared, which were three sets of multi-wire secondary emission beam profile monitor (two “Multiwire detector” in Fig. 2.21 and on “WIRE CHAMBER” in Fig. 2.19), an ultra-thin foil detector (“Foil detector” in Fig. 2.21), two sets of delay-line 2-dimensional position sensitive detectors with microchannel plates (“MCP 1” and “2” in Fig. 2.19), two sets of Čerenkov detectors (“Čerenkov detector” in Fig. 2.21), and two sets of track detectors (only superconducting solenoid side is shown, “Scinti. bar” with “PMT”’s in Fig. 2.21).

2.5.1 Beam profile monitor

The multi-wire secondary emission beam profile monitor consists of 32 horizontal and vertical gold-plated tungsten wires, which has 95% transmission (See Fig. 2.22). Each wire is followed by a charge-sensitive preamplifier.

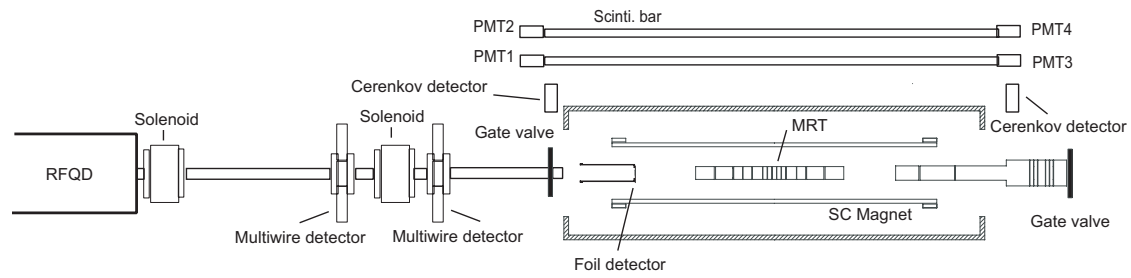


Figure 2.21: Configuration of detectors around our experimental beam line.

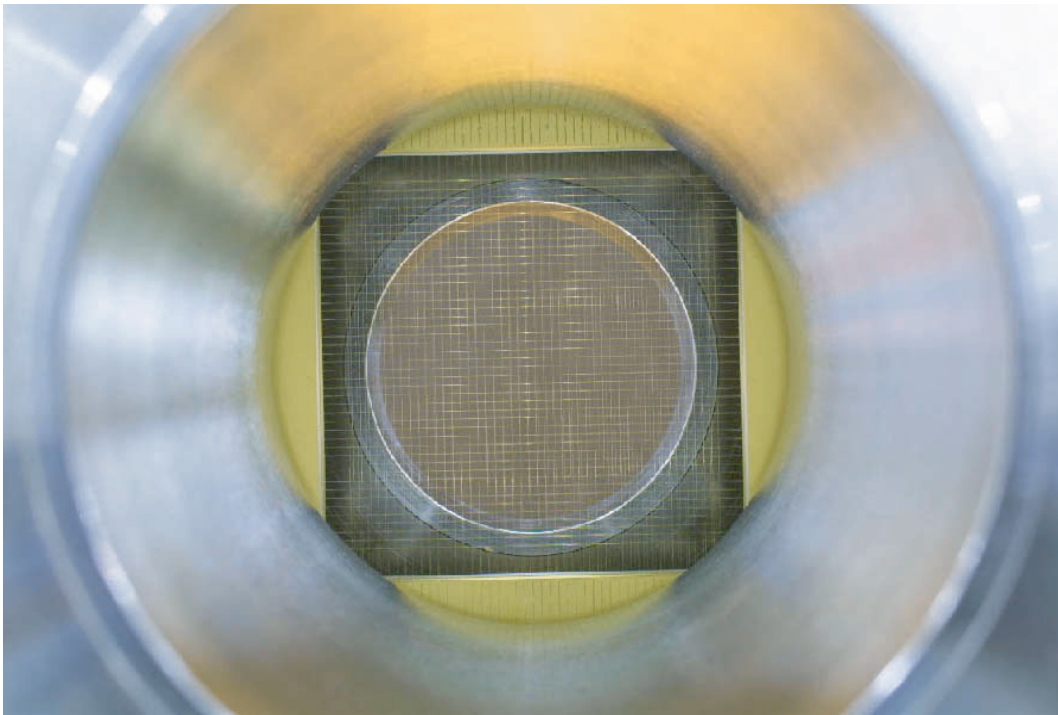


Figure 2.22: Picture of secondary emission beam profile monitor consists of 2-dimensional wires ($20\mu\text{m}\phi$).

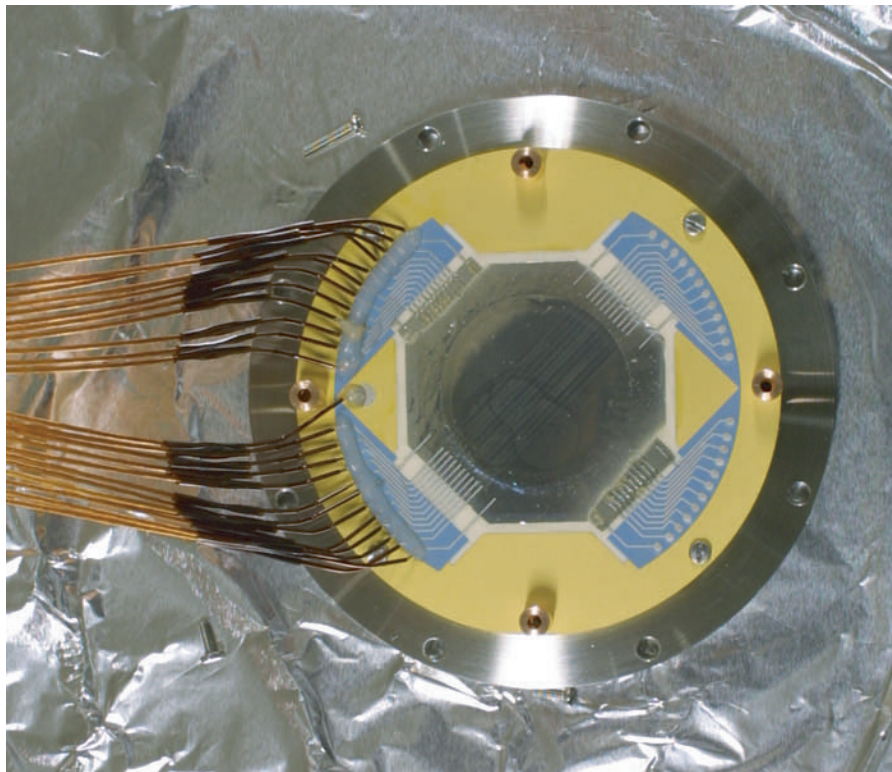


Figure 2.23: Top view of X-Y patterned ultra-thin foil electrode.

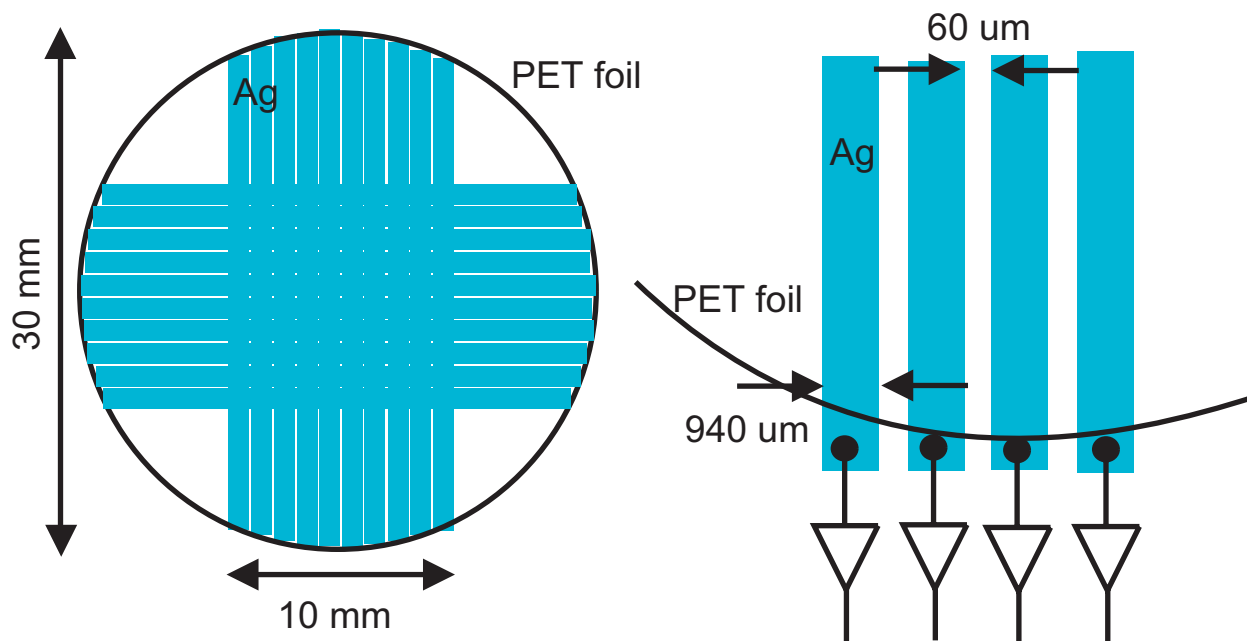


Figure 2.24: Schematic of the foil detector.

Two sets of multi-wire secondary emission beam profile monitor were installed in the LEBT to monitor the beam profile of antiprotons from the RFQD (Fig. 2.21). One more monitor was also installed in the extraction beam line (“WIRE” in Fig. 2.19).

The foil detector is made of double thin PET degrader foils of 10 mm in diameter (Fig. 2.23) on which ten thin Ag strips of 50 nm thick and 940 μm width are printed (Fig. 2.24). The foil detector is installed at 30 cm from the entrance of the superconducting solenoid and monitors the antiproton beam profile in front of the MRT. By monitoring an image from this ultra-thin foil detector, the beam was focused and transported to the axial center of the MRT.

2.5.2 Microchannel plate with delay-line anode

A microchannel plate (MCP) of 47mm in active diameter combined with two dimensional delay line assembly was used to monitor the extracted antiprotons at relatively low rate, 10 kHz.

The delay line anode is made of two sets of parallel helical wires oriented in x - and y -directions. The position information is obtained from the the time difference of each delay line. The signal propagation time on the delay line is about 1 ns per mm, and the corresponding position resolution was ≈ 0.1 mm. The time difference of the signals are measured through time-to-amplitude converters (TAC).

2.5.3 Čerenkov detector

Čerenkov detectors made of acrylic plates with the refractive index of $n = 1.49$ with fine-mesh photomultipliers [70] were installed at the entrance of the superconducting magnet and also at the exit as shown in Fig. 2.21. These detectors were operated in analogue mode.

The pulse height of the signal due to annihilation products is proportional to the annihilation rate and accordingly the time spectrum of the incident antiproton pulse. The transport efficiency from the RFQD to the MRT was evaluated with the Čerenkov detectors.

The timing to turn on the high-voltage MOS-FET switch was determined referring to the signal from the entrance Čerenkov detector.

2.5.4 Track detector

In order to measure annihilation position of antiprotons, two sets of track detectors were prepared. One set of track detectors consisted of two 2-m long plastic scintillator bars with a cross section of $4 \times 6 \text{ cm}^2$. They were located parallel to the trap axis with photomultipliers on both ends. The distances of the scintillator bars from the MRT axis are 40 cm and 74 cm, respectively, as shown in Fig. 2.25, thus subtending overlapping solid angle seen from the MRT axis is 0.12 steradians. From the Monte-Carlo simulation, the detection efficiency of the track detector was found to be 5% for antiprotons annihilated at the center of the MRT [71]. The other set of track detector with a similar configuration was also installed along the extraction beam line at the distance of 56 cm and 90 cm from the axis of the extraction beam line. The solid angle was about 0.09 steradians.

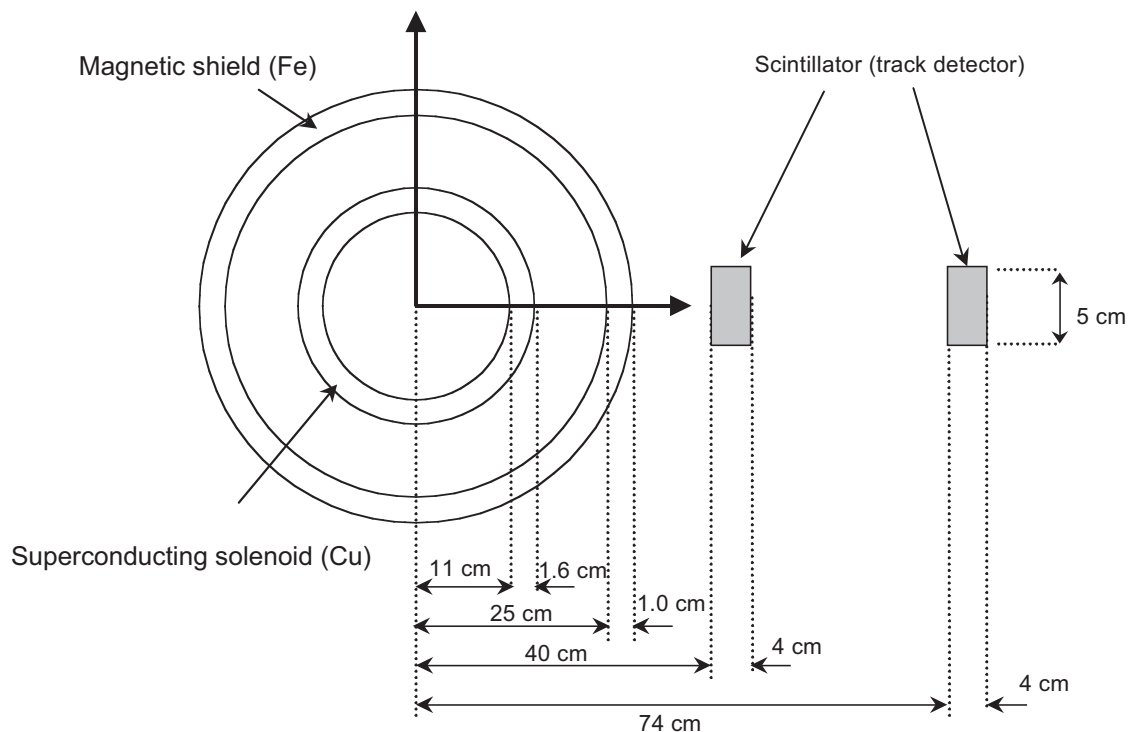


Figure 2.25: Configuration of track detector along the superconducting solenoid.

The position of antiproton annihilation was evaluated from the arrival time differences of the light pulses between two photomultipliers on both ends.

1. Light pulses produced in scintillators by passage of charged particles due to antiproton annihilations were detected by photomultipliers at both ends of the scintillator bars (PMT 1, 2, 3 and 4 in Fig. 2.26).
2. The hitting positions of the charged particle on the scintillator bars (position “a” and “b” in the figure) were calculated from the time difference.
3. The annihilation position was evaluated as the intersection (“z” in the figure) of the trap axis and the line connecting points “a” and “b”.

The photomultiplier used were of a 2-inch line-focus type (Hamamatsu Photonics R329-PSX) with a magnetic shield.

Figure. 2.27(a) shows an example of the annihilation position distribution for antiprotons trapped in the MRT for more than 1 hour and annihilated in the MRT by collisions with residual gasses. The full-width at half-maximum was about 15 cm. As is seen, the spectrum shows a long tail, which originates from Compton scattered electrons in materi-

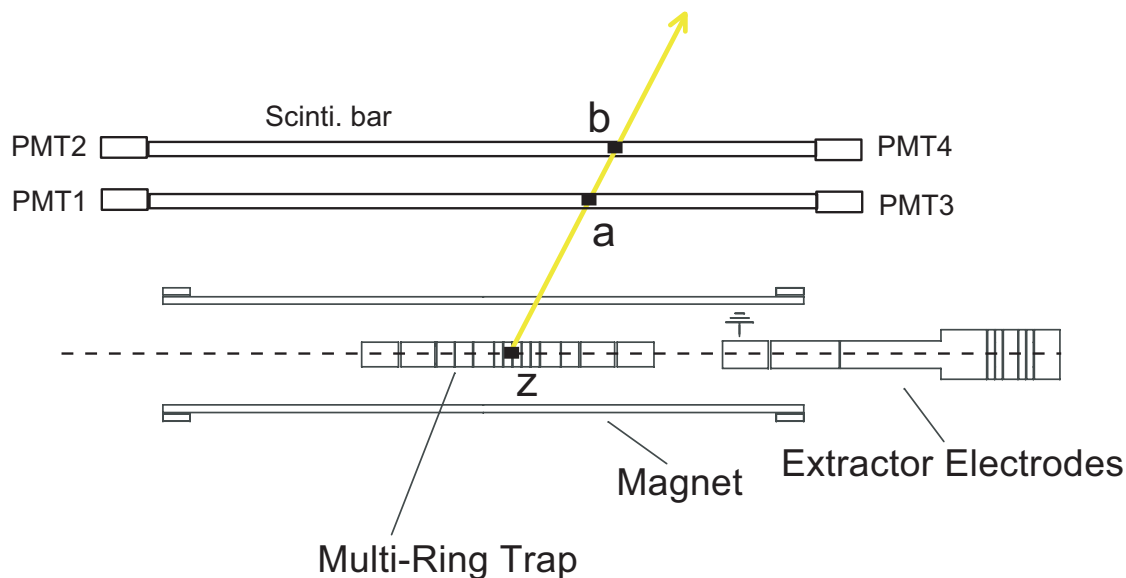


Figure 2.26: Schematic view of track detector.

als, i.e., electrodes, solenoid coils, magnetic shields and so on, as shown by a simulation results (Fig. 2.27(b)) using the GEANT simulation package [72] [71].

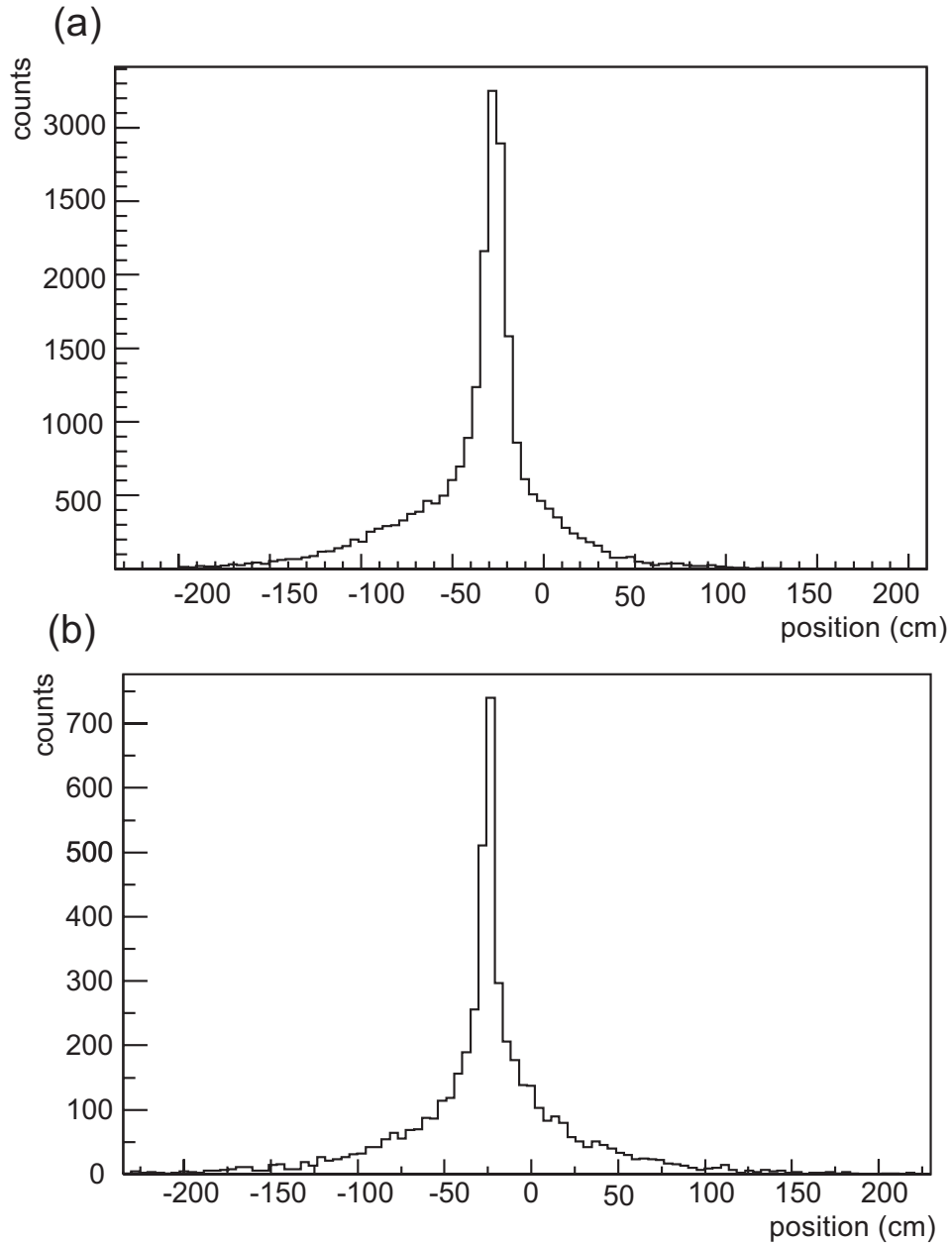


Figure 2.27: (a) Experimentally obtained annihilation positions of antiprotons. (b) Calculated positions of antiprotons annihilations in the MRT.

2.6 Control and data acquisition system

Almost all equipments were controlled synchronized to the trigger pulse just 6 ms before the antiproton injection from the AD. The schematic diagram of control and data acquisition system is shown in Fig. 2.28.

For the detector system, outputs of the secondary emission monitor, ultra-thin foil detector, two sets of track detectors and the MCP-PSD were acquired through CAMAC registers to a PC (IBM-PC/AT compatible personal computer) via GPIB or SCSI interface. The outputs from the Čerenkov detectors were recoded by a digital oscilloscope (LeCroy LC584A), and were transferred to another PC.

The magnetic field of superconducting solenoid, a steeping motor for alignment of the axis of the bore tube, voltages for electrodes of the MRT and the extraction beam line, field emission array for electron injection and the variable apertures were controlled by PCs via GPIB or RS-232C interface and also synchronized to the AD trigger.

The high-voltage switch was synchronized via a digital delay generator for adjustment of the ramp up timing.

The PCs connected to GPIB- or RS-232C-controlled equipments communicate through the TCP/IP 6656 port each other. And also all PCs are running under Labview Ver. 6.1 (National Instruments) on Linux.

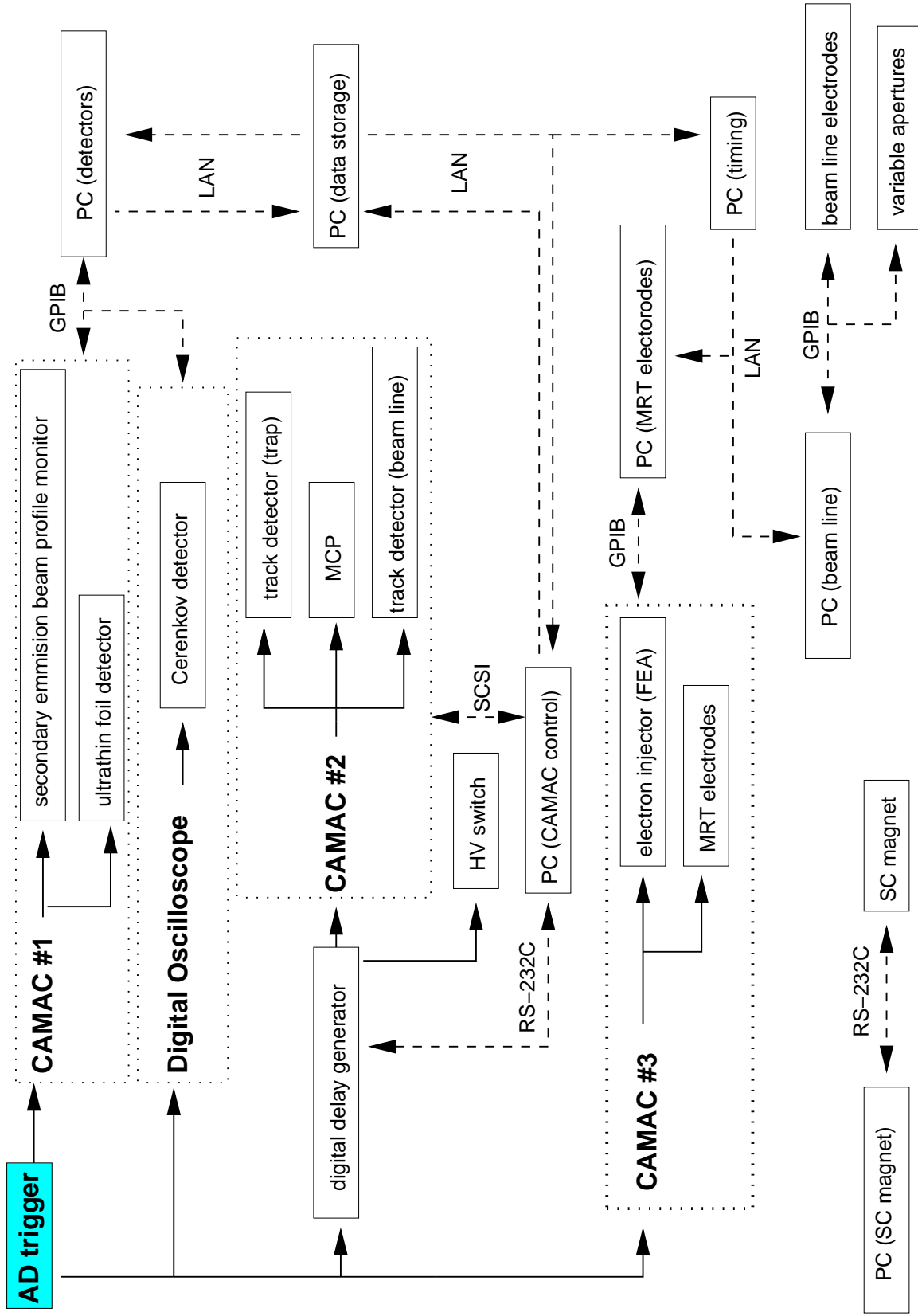


Figure 2.28: Schematic of the control system

Chapter 3

Confinement of antiprotons

Antiprotons from the RFQD was transported to the MRT and confined there. In this chapter, the scheme of antiproton trapping is explained. Then the effect of the beam transport parameters tuning on the capture efficiency of antiprotons is described. Finally, the experimental results of capture and stable confinement of antiprotons in the MRT are described.

3.1 Scheme of the confinement of antiprotons in the MRT

Figure 3.1 shows a flowchart of the procedures taken during the antiproton trapping employed in the present work, which is explained one by one below. Figure 3.2 schematically shows the potential configuration during the antiproton trapping procedures.

1) Electron injection and preparation The magnetic field is ramped up first to 2.5 T, which was kept during the experiments. Before the injection of antiprotons from the AD, a harmonic potential was formed at the center of the MRT, then electrons are injected and trapped in the MRT. The 10 kV high-voltage is applied to the electrode DCE for reflection of antiprotons.

2) Setup detectors Detectors are initialized. Then PCs controlling the MRT and the extraction beam line pauses until the antiproton pulse arrives.

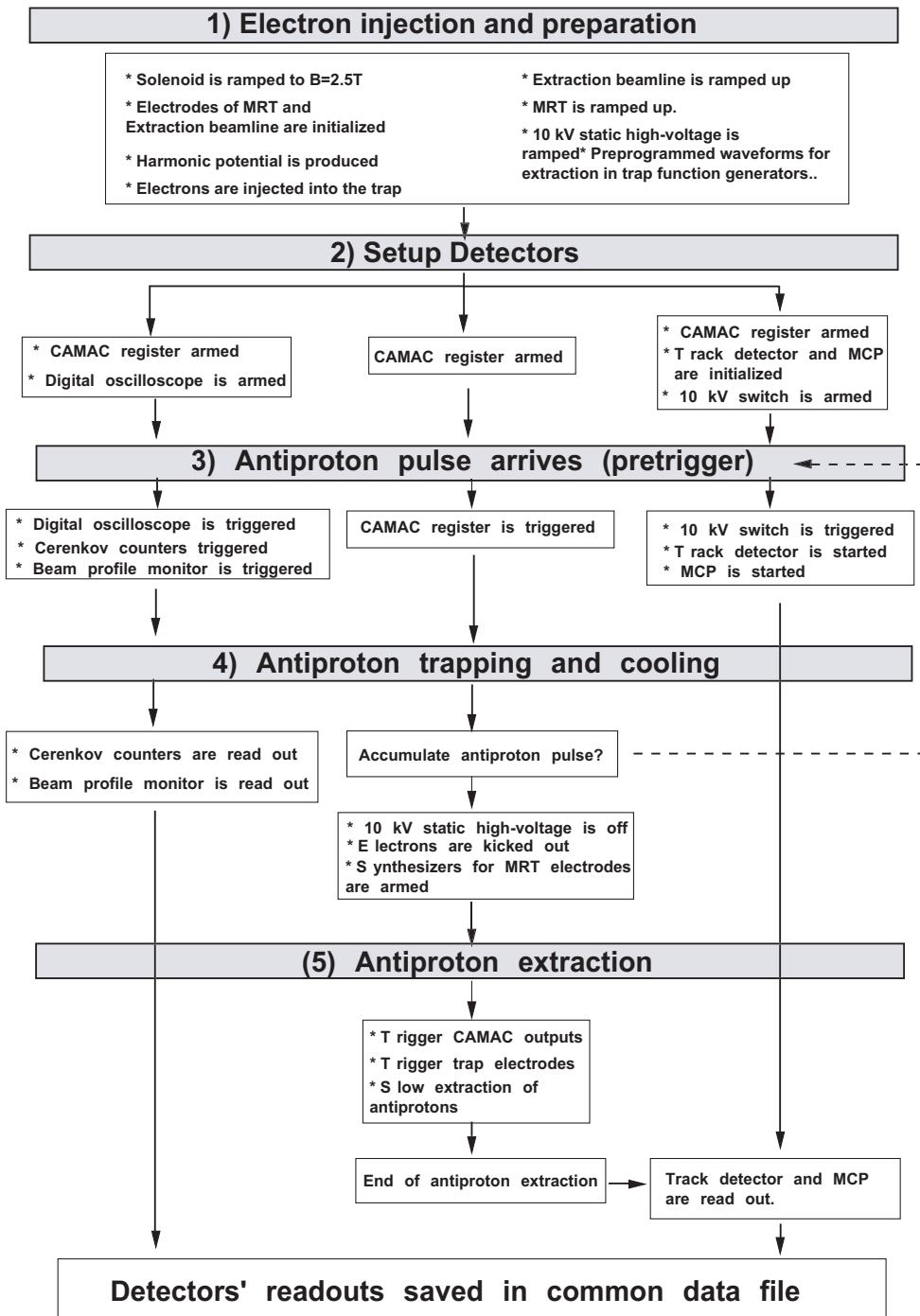


Figure 3.1: Flowchart of the cycle of antiproton trapping, cooling and extraction.

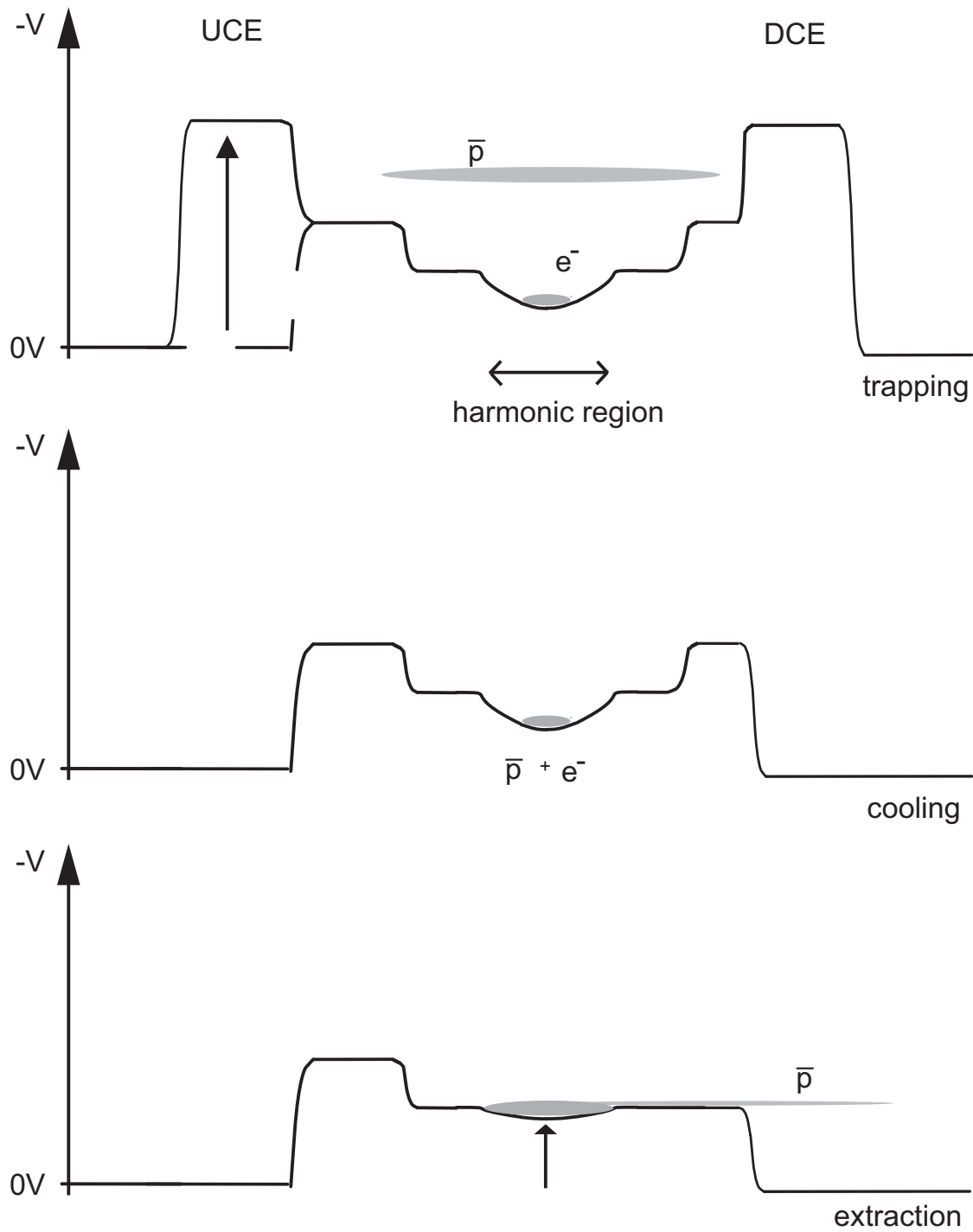


Figure 3.2: The scheme of antiprotons trapping, cooling and extraction.

3) Antiproton pulse arrives When a TTL pulse $6 \mu\text{s}$ before the antiprotons injection arrives, the secondary emission beam profile monitors, the foil detector, and the Čerenkov detectors start to record signals via a digital delay generator for monitoring antiproton injection. The semiconductor high-voltage switch is also triggered to capture antiprotons.

The antiprotons delivered from the AD are decelerated by the RFQD. Antiprotons ejected from the RFQD were transported and focused through the LEBT to the MRT located in the strong magnetic field of $B = 2.5 \text{ T}$. At the entrance of the MRT (70 cm upstream from the MRT center), energy degrading foils are located, which degraded their energy down to $\sim 10 \text{ keV}$. The antiprotons passing through the degrader foils entered the MRT and were captured between two high-voltage electrodes (“trapping” in Fig. 3.2).

4) Antiproton trapping and cooling Then the pulse unlocks the paused PCs controlling the MRT and the extraction beam line electrodes. Some detectors monitoring antiproton injection are read out. The captured antiprotons are cooled via collisions with electrons confined in the harmonic potential (“cooling” in Fig. 3.2).

5) Antiproton extraction Before the extraction of ultra-slow antiprotons, electrodes of the MRT and the extraction beam line are electrically floated, whose voltage define the energy of extracted ultra-slow antiprotons.

The detectors on the extraction beam line are triggered. After the electron cooling, antiprotons were ejected to the downstream by ramping the trapping harmonic potential, and transported via the beam line (“extraction” in Fig. 3.2).

All detector readouts are saved in the common data file on the PC. (see also Fig.2.28)

3.2 Antiproton beam transport to the MRT

From the AD to the MRT located in the 2.5 T superconducting solenoid, antiprotons were transported through some steering and focusing elements as were shown in the Fig. 2.4. The effect of beam steering before the injection to the RFQD (Sec. 3.2.1), the beam bunch-

ing (Sec. 3.2.2) and the beam transport after the RFQD (Sec. 3.2.3) are discussed in this section.

3.2.1 Beam transport at the MEBT

The antiproton beam ejected from the AD was transported via the beam line as shown in Fig. 2.4. As was described in Sec. 2.2, antiproton beam was bunched at the buncher (“1” in Fig. 2.4) and injected into the RFQD. The beam profile was observed at the “watchdog” (“10” or “11”) beam profile monitors.

When the beam was off axis, the number of captured antiprotons was drastically decreased. The focusing of the beam was also effective; in fact, when the beam was under-focused or over-focused the efficiency of capturing the antiprotons became worse.

The transport parameters to the RFQD were surveyed by monitoring beam images on the watchdog screens when the beam did not hit the periphery of the scintillators’ holes and the trapping number was maximized. After the steering and focusing using dipole and quadrupole magnets, the antiproton beam passed through the center. Figure 2.6 shows an example that the major fraction of the beam passed through the scintillator holes, where the beam emittance was about 1.1π mm · mrad (Tab. 2.2).

3.2.2 Tuning of the buncher phase

The bunching cavity transforms the antiproton pulse into micro-pulses suitable for surfing on the RF wave for effective deceleration in the RFQD.

Figure 3.3 shows the fraction of decelerated antiprotons against the buncher phase. By tuning the buncher phase, the deceleration efficiency of the RFQD varied more than 5 times.

One rotation of the buncher phase means 60 keV energy difference (See Sec. 2.2). From the Fig. 3.3 the observed width was 32° FWHM which corresponds to ~ 5 keV energy spread of the incident beam.

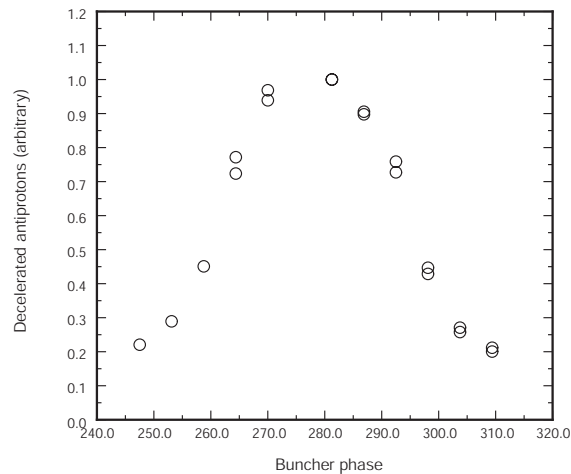


Figure 3.3: The ejected 110 keV antiprotons v.s. buncher phase in degrees.

3.2.3 Transport of 110 keV antiproton beam at the LEBT

After the deceleration in the RFQD, antiprotons were delivered via the LEBT to the MRT. The decelerated beam was diagnosed by the beam profile monitor in LEBT. To focus the antiprotons injected to the MRT, two sets of pulsed solenoid ($B \approx 1$ T) were used. Figure 3.4 shows examples of the beam cross sections monitored by the two beam profile monitors. At the position of these monitors, the beam transport simulation [61] shows, as was described in Sec. 2.2, that the profile of the transported beam should not be focused, but be in parallel to the axis (See Fig. 2.10).

Figures 3.5 (a) and (b) show examples of x - and y -projected beam profiles at the monitor embedded in the degrader foils. The beam was tuned using the last set of steering dipoles so that the radial distribution was as small as possible at the center of the thin foil detector. The center of the detector corresponds to the axis of the MRT. After the tuning, the beam was centered with its diameter of about 2–3 mm FWHM as shown in Figs. 3.5 (a) and (b). In Fig. 3.5 (c), the time evolution of integrated annihilation counts of antiprotons detected by the track detector is shown. The initial annihilation counts $N_{i,1}$ from the injection $t = 0$ s to $t \sim 10$ s was about 6 000 and the number of antiprotons remained till the last moment $N_{t,1}$, which were confined in the harmonic potential, was about 7 000.

If the beam was off-axis, the results are shown in Fig. 3.6. The profiles are in Fig. 3.6 (a) and (b). The beam was 5 mm off along x axis and 2.5 mm off along y axis. In this case, the initial annihilation counts $N_{i,2}$ became larger and the number of trapped antiprotons $N_{t,2}$ was smaller.

To confine the antiprotons in the harmonic potential, the antiproton beam had to be injected on axis to the MRT.

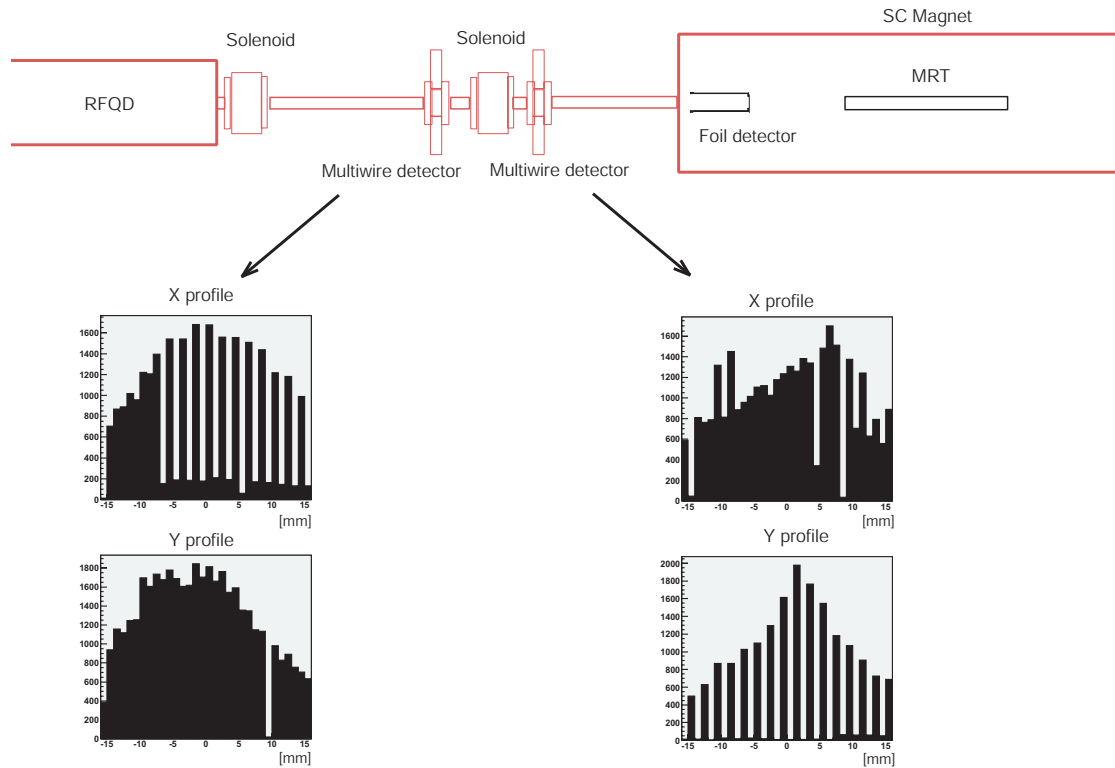


Figure 3.4: Antiproton beam profile detected at LEPT.

3.3 Degrading antiproton beam energy through thin foils

3.3.1 Energy loss in the PET foils

Examples of the annihilation spectra observed by the upstream Čerenkov detector are shown in Fig. 3.7. Figure 3.7 (a) shows the spectrum when the “Gate valve 1” located at the entrance of the MRT was closed for the decelerated antiproton energy of 91.5 keV. The first peak corresponds to the non-decelerated 5.3 MeV antiprotons. The second peak

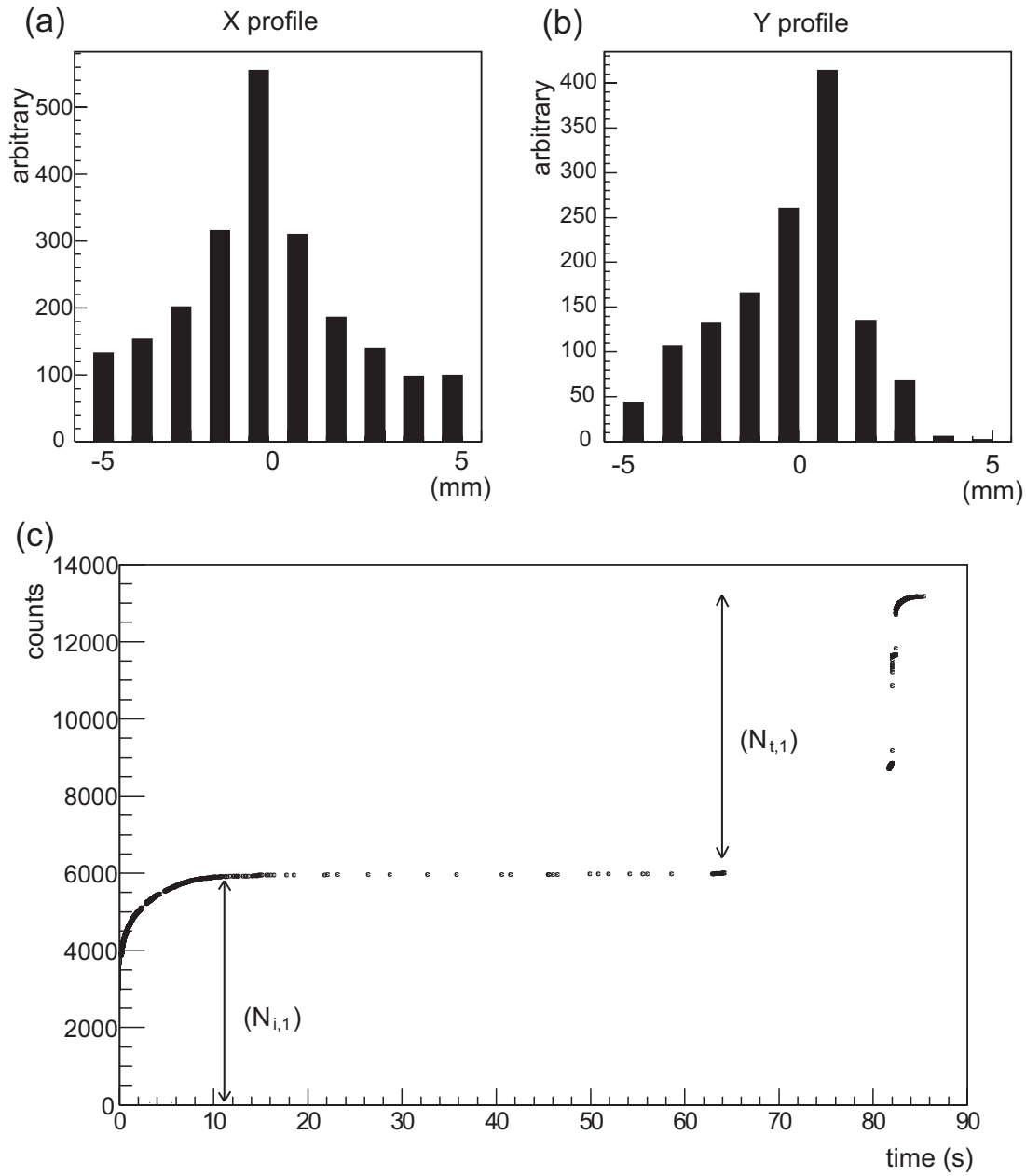


Figure 3.5: Beam profiles and the number of trapped antiprotons. In this case the beam was well focused and on-axis.

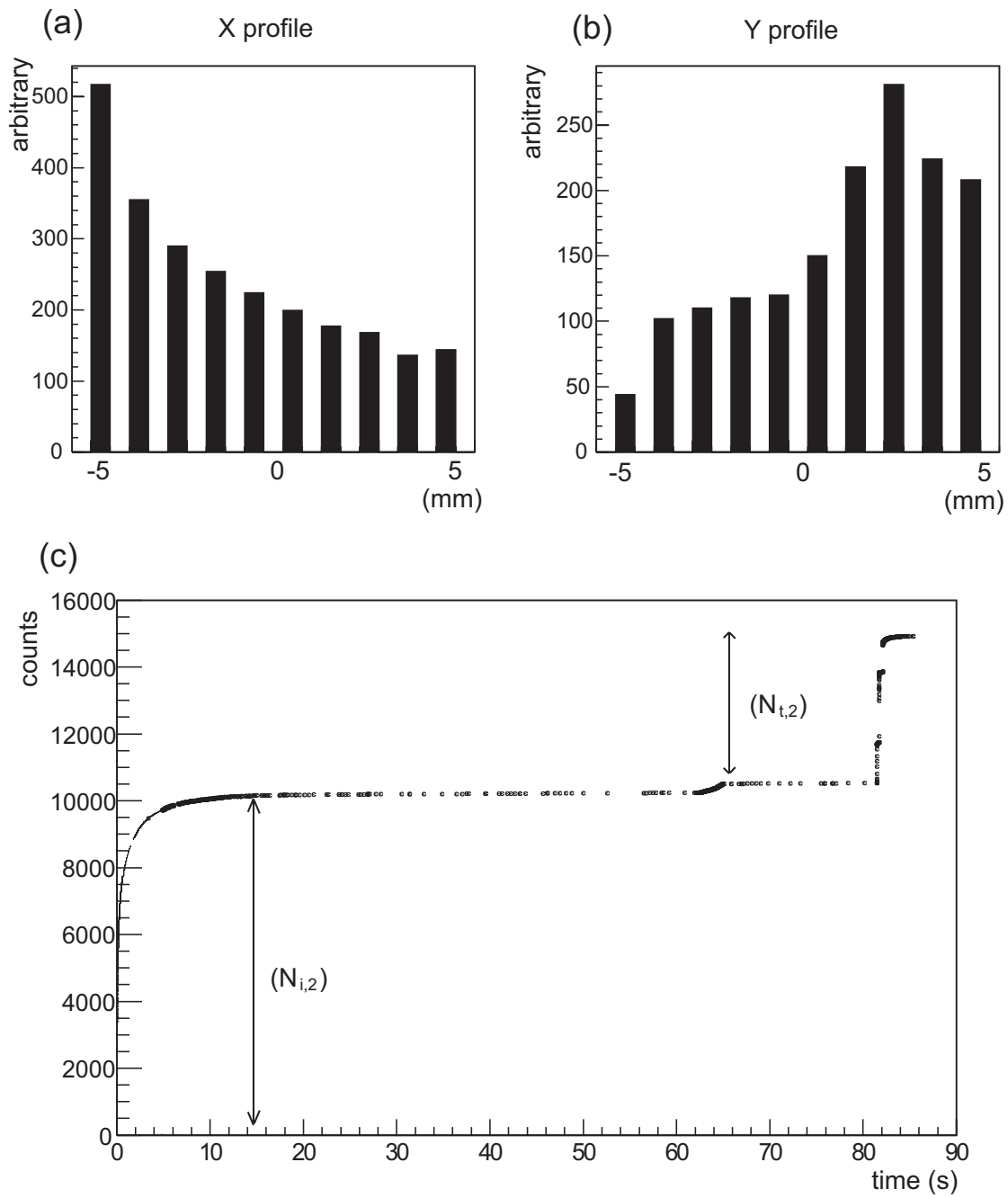


Figure 3.6: Beam profiles and the number of trapped antiprotons. In this case the beam was not focused at the foil.

observed at $1.250 \mu\text{s}$ corresponds to the decelerated components by the RFQD. Figure 3.7 (b) shows the spectrum when the gate valve was opened, where the second peak observed at $1.320 \mu\text{s}$, which corresponds to annihilations of decelerated antiprotons in the PET foils, indicated that the antiproton energy of 91.5 keV is not high enough to pass the foils. When the ejection energy of the RFQD was increased to 121.5 keV, the second peak decreased drastically as shown in Fig.3.7 (c). Figure 3.8 shows the spectra observed by the downstream Čerenkov detector for (a) 91.5 and (b) 121.5 keV antiprotons, respectively, when the “Gate valve 2” was closed.

Figure 3.9 shows the annihilated fraction in the foils as a function of the incident antiproton energy, which were evaluated from the area of the second peak of the upstream Čerenkov detector. When the injection energy was 91.5 keV, all the decelerated antiprotons annihilated in the foils. This was confirmed because no antiprotons were observed in the downstream side. Figure 3.9 shows that the fraction decreases monotonically as the incident energy is increased with a slight indication of a flat off at $\sim 115 \text{ keV}$.

3.3.2 Energy distribution of the degraded antiprotons

Figure 3.10 shows signals of the downstream Čerenkov detector without and with 10 kV barrier applied to the electrode DCE when antiprotons were injected. The first peak corresponds to 5.3 MeV antiprotons which were not decelerated by the RFQD. The components of last broad peaks are the decelerated antiprotons which passed through the degrader foils. When the reflection high-voltage ($V \text{ kV}$) on the DCE was turned on, the antiprotons whose longitudinal energy was less than $V \text{ keV}$ were reflected to the upstream.

The difference of the time spectra with and without the reflection voltage corresponds to the reflected component. Figure 3.11 shows the reflection ratio of antiprotons by the high-voltage barrier for 106.5, 111.5 and 121.5 keV antiprotons. The red curve in Fig. 3.12 is the energy distribution obtained by deriving the curve for 111.5 keV in the Fig. 3.11.

Figure 3.11 shows as the input energy decreased the ratio of the reflected antiprotons increased. It is noted that the high-voltage switch to plug the reflected antiprotons between

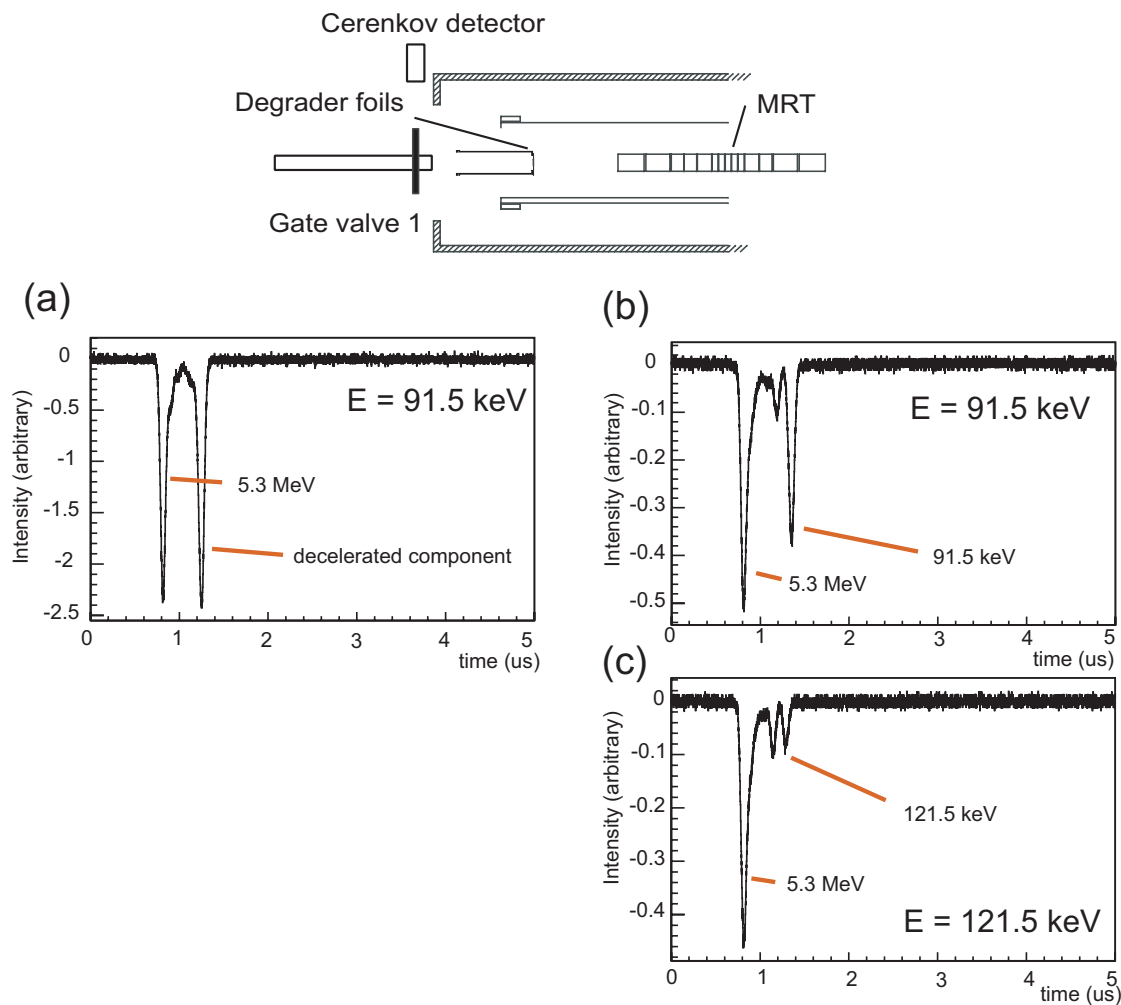


Figure 3.7: Time spectra observed by upstream Čerenkov detector. (a) Gate valve located at the entrance of the MRT was closed (See Fig. 2.21). (b) Gate valve was opened. (c) Same as (b), but the injection energy of antiprotons was higher.

UCE and DCE can produce only 10 kV. Therefore antiprotons whose longitudinal energy was less than 10 keV could be captured by the switch. Figure 3.11 shows that 85% of 106.5 keV antiprotons passing through the degrader foils were reflected by the 10 kV high-voltage barrier. For 111.5 and 121.5 keV injection energies, the ratio was 75% and 60%, respectively.

On the other hand, for lower energies more antiprotons annihilated in the degrader foils as was described in the previous section. Figure 3.13 shows the ratios of reflected antiprotons against the incident antiprotons from the AD, which were $\sim 38\%$, $\sim 49\%$, $\sim 47\%$

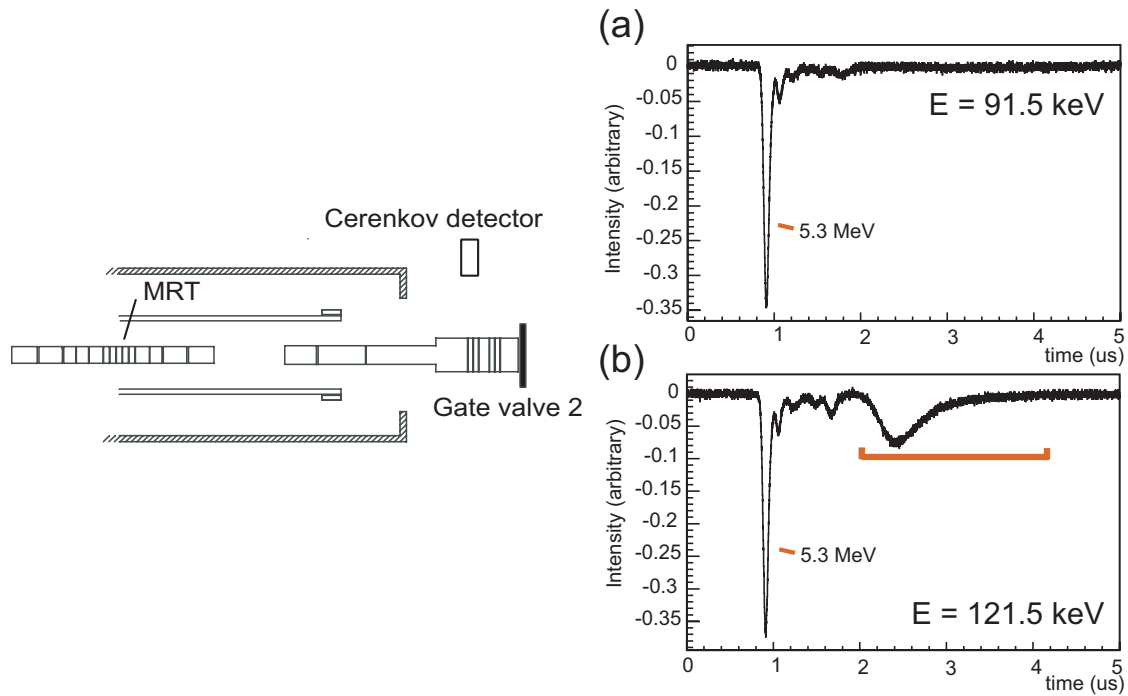


Figure 3.8: Spectra observed by downstream Čerenkov detector. (a) The injection energy was 91.5 keV. (b) 121.5 keV.

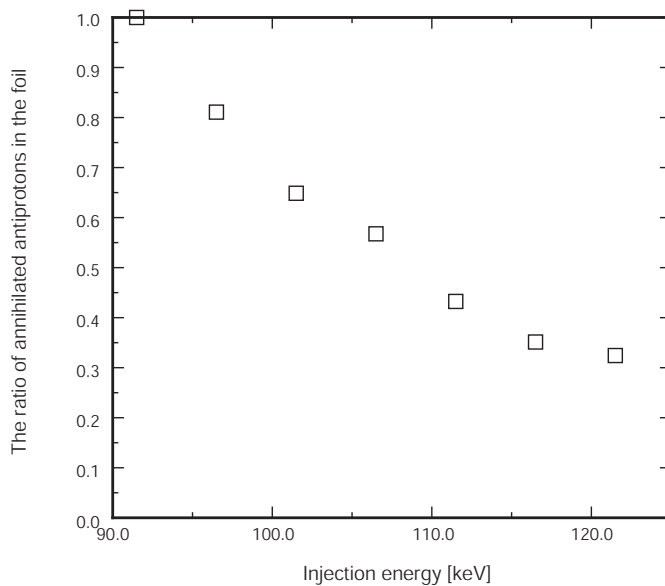


Figure 3.9: Annihilated fraction of antiprotons in the degrader foil against their injection energy.

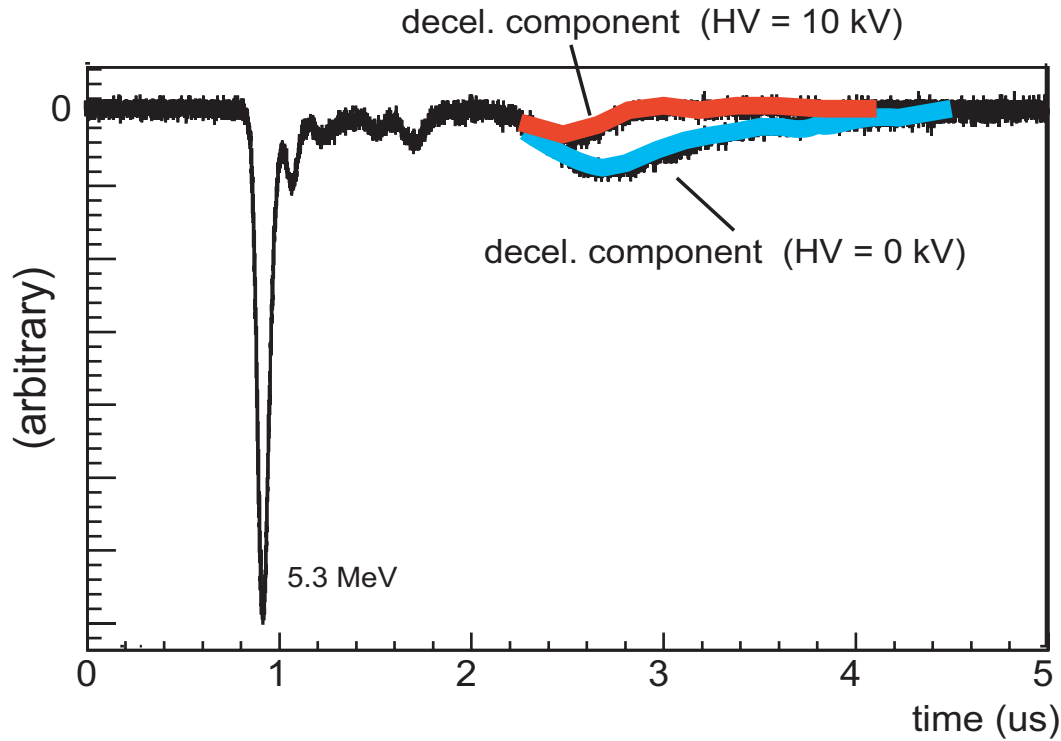


Figure 3.10: Antiprotons annihilations signal observed by the downstream Čerenkov detector. First sharp peak corresponds to 5.3 MeV non-decelerated antiprotons. The last broad peaks come from the decelerated and transmitted antiprotons. Here, two time spectra were superimposed, one with the high-voltage barrier off (HV = 0 kV) and the other with 10 kV barrier.

and $\sim 42\%$ for 106.5, 111.5, 116.5 and 121.5 keV incident antiproton beams, respectively. Thus the input energy of antiprotons from the RFQD was chosen to be 111.5 keV to maximize the number of trapped antiprotons.

3.4 Confinement in the MRT

Antiprotons thus decelerated to below 10 keV by passing through the degrader foil were captured by a set of catching electrodes. The following section discusses the optimization of the timing of the pulsed high-voltage potential and the number of confined antiprotons in the MRT.

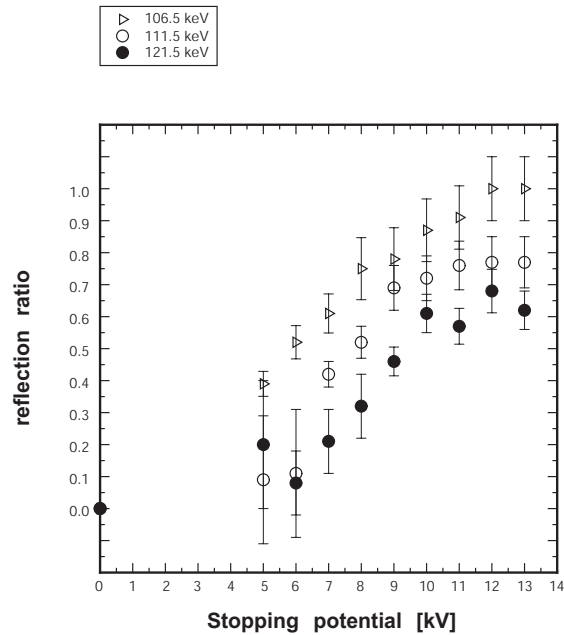


Figure 3.11: Ratio of reflected antiprotons at electrode DCE against various reflection voltage for injection energies of 106.5 keV, 111.5 keV and 121.5 keV.

3.4.1 Capture of the 10 keV antiprotons

The decelerated antiprotons were captured with a 10 kV high-voltage switch, which confines antiprotons whose longitudinal energy was less than 10 keV.

Figure 3.14 shows the capturing efficiency as a function of the high-voltage switch timing. A plateau is recognized from $373.25 \mu\text{s}$ to $374.00 \mu\text{s}$. The optimum timing was selected when the number of antiprotons was maximized.

3.4.2 Confinement of antiprotons in the MRT

The number of trapped antiprotons were observed by their annihilations using the track detectors (Sec. 2.5).

Here we define that the number of trapped antiprotons is the number remained till the antiprotons were extracted or dumped from the MRT (See Fig. 3.15 (a)). The detection efficiency of the track detector was 5% at the center of the MRT. But in most of cases, antiprotons were extracted to the downstream side and annihilated at around 80 cm down-

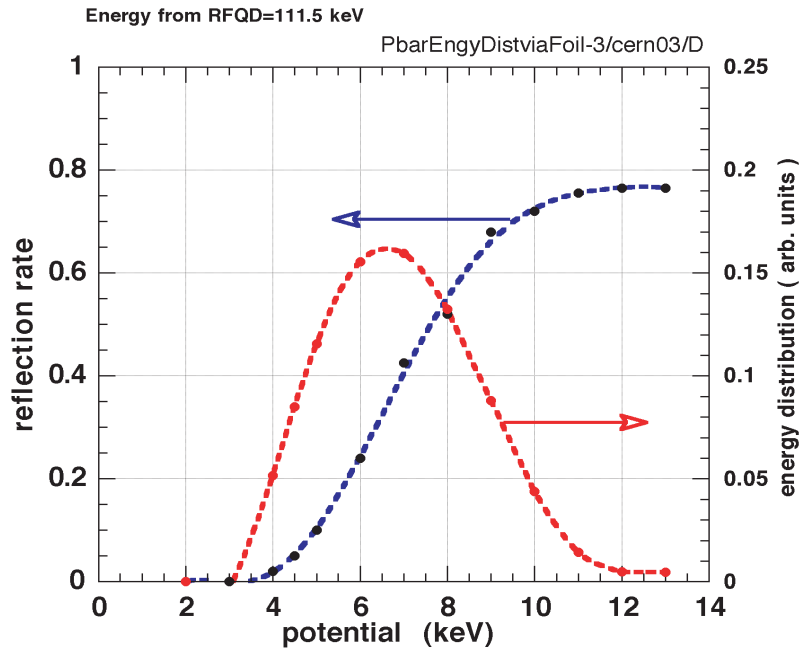


Figure 3.12: The energy distribution of 111.5 keV antiprotons beam which passed through the degrader foil from the RFQD (red points and curve). Blue points and curve show the reflection ratio (same in Fig. 3.11).

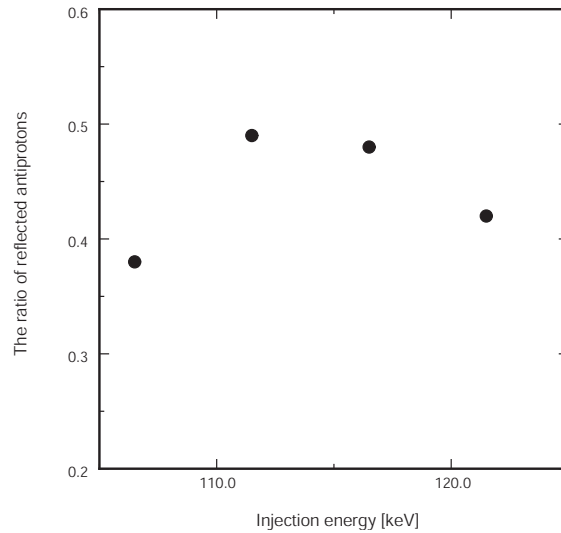


Figure 3.13: The ratio of reflected antiprotons against the total number of antiprotons decelerated by the RFQD.

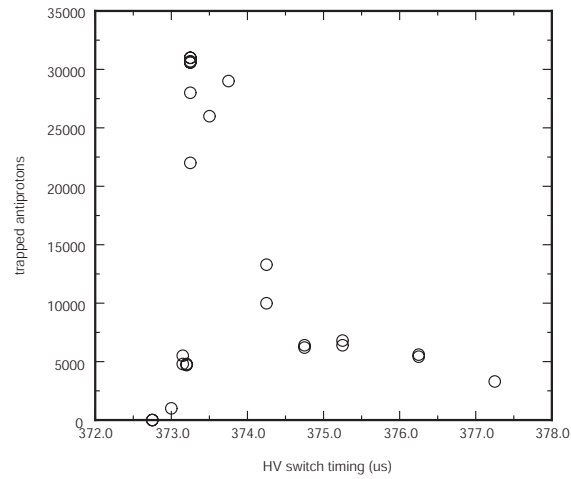


Figure 3.14: The number of captured antiprotons vs. the HV switch timing.

stream from the center where the efficiency was about 3%. In the best case, the number of annihilations counted by the track detector was 36 000, namely the estimated number of trapped antiprotons was $3.6 \times 10^4 / 3\% = 1.2 \times 10^6$. At that time, the total number of delivered antiprotons from the AD was 3×10^7 . Consequently, the trapping efficiency was 4%, a factor of 50 higher than that obtained using simple degrader foil method [44].

Figure 3.15 shows the integrated annihilation counts during (a) one AD shot and (b) 5 AD shots. For the case of the Fig.3.15, $3.1 \times 10^4 / 3\% = 1.0 \times 10^6$ antiprotons were confined per one AD shot. When 5 shots were accumulated, $1.45 \times 10^5 / 3\% = 4.8 \times 10^6$ antiprotons were trapped, which was about 5 times larger than the single AD shot, confirming that the total number of trapped antiprotons was in proportional to the number of the accumulated AD shots. Figure 3.16 shows the total number of antiprotons as a function of the number of AD shots.

3.4.3 Vacuum condition for stable confinement

In the MRT, antiprotons annihilate with residual gases. Since the formation cross section of antiprotonic atom becomes larger at lower temperature as described in Sec 1.2.1, it can suppose that antiprotons annihilate as soon as they are cooled. To cool antiprotons in the MRT, collisions between antiprotons and electrons play a dominant role (See [66]

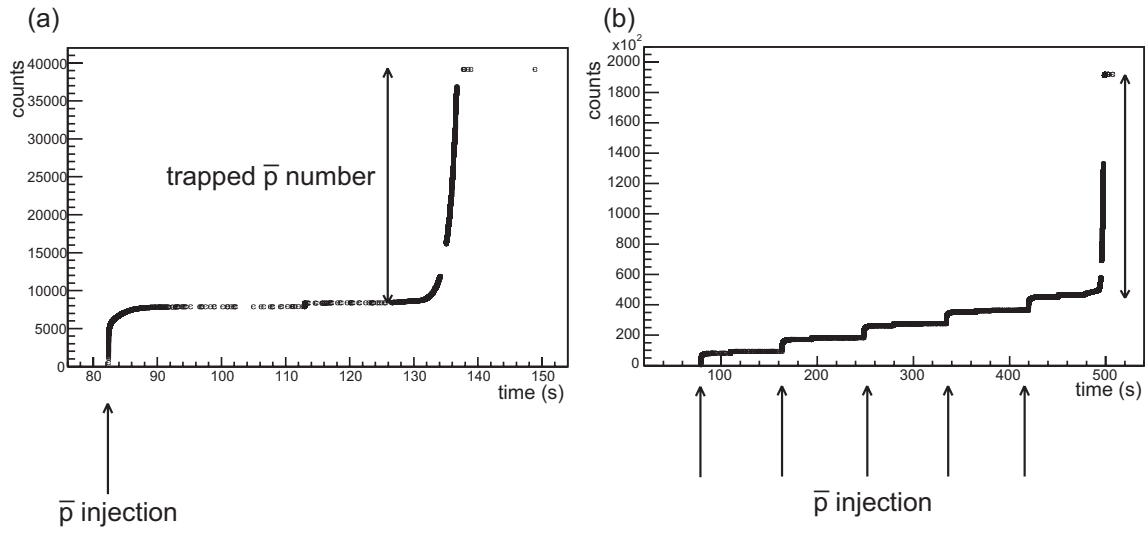


Figure 3.15: Antiproton annihilation counts during (a) a cycle and (b) a 5-shots accumulation.

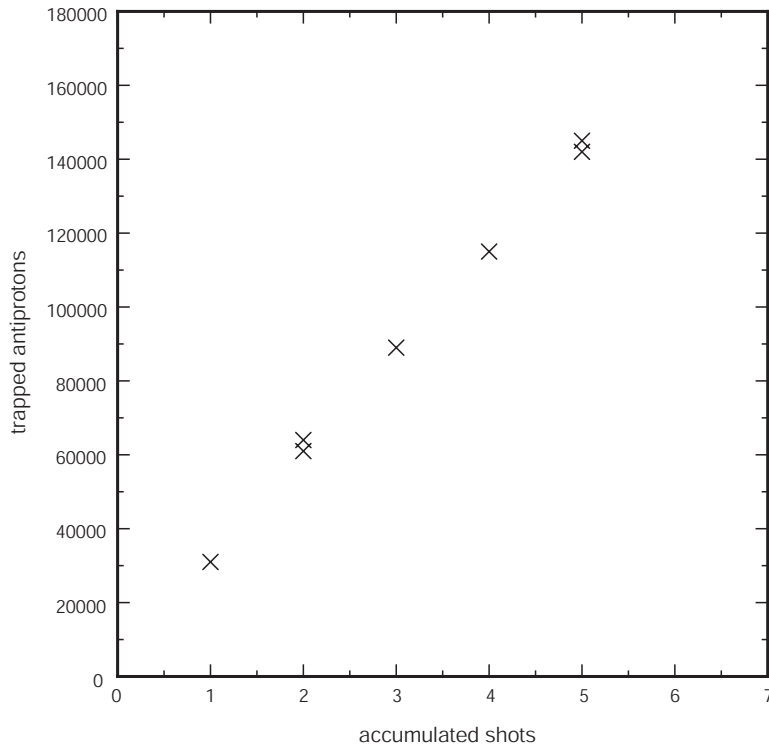


Figure 3.16: Trapped antiproton number vs. accumulation number.

and also Sec. 4.2). These electrons were preloaded before antiproton injection from the emitter (See Sec. 2.3.5). Moreover electrons were produced through ionization of residual gases by energetic antiproton, whose number was decided by the number of residual gas atoms and/or molecules. The pressure of residual gases depends on the environmental temperature, at lower temperature the pressure of residual gases becomes small.

Therefore the vacuum around the MRT is one of the key issue for stable confinement of antiprotons. As described before, the required vacuum is less than 10^{-12} Torr which was realized by cooling down the bore tube less than 10 K. The vacuum gauge was mounted outside, the reading was around 1×10^{-10} Torr at that time. Since the cold bore tube behaves as a cryo-pump, the real pressure around the MRT should be much less than 10^{10} Torr.

Figures 3.17 and 3.18 show the time evolution of integrated annihilation counts for various temperatures of the bore tube with and without cooling electrons, respectively. In these experiments, high-voltages for catching antiprotons were kept on. When the temperature of bore tube was high as shown in Fig. 3.17 (a), antiprotons annihilated in the trap soon after the injection. When the electron plasma was prepared which is in the case of Fig. 3.17, captured antiprotons settled in the harmonic potential well soon and then started to annihilate. At 32 K, it took about 15 s until the antiprotons started to annihilate. As the temperature went down, the time duration with the start of annihilation get longer: for example, at 9 K, it took more than 25 s. The duration depends on the number of the electrons. Of course, same number of electrons were injected at each case, but additional electrons were produced by ionization of the residual gases by the antiproton injection. The slope which corresponds to the annihilated events per unit time is also different, which primary depends on the residual gas density. When the vacuum was better, the annihilation count was almost negligible.

In Fig. 3.18, the electron plasma was not prepared. Due to the lack of coolant, antiprotons were not cooled. At 18 K, antiprotons never cooled for longer than 125 s, most of them annihilated when the 10 kV catching potential was turned off. On the other hand,

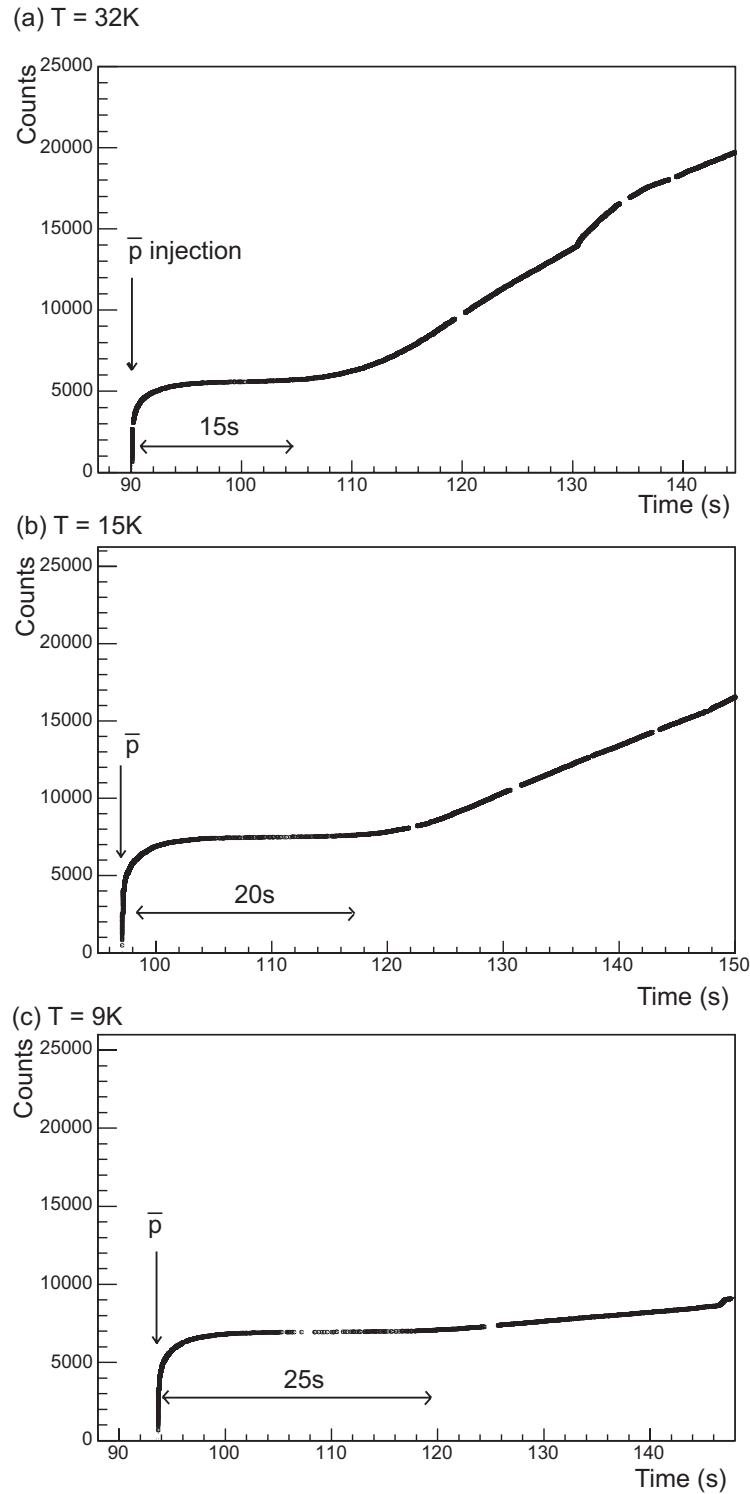


Figure 3.17: Integrated annihilation counts of antiprotons with preloaded electrons: (a) the bore tube temperature was around 32 K, (b) 15 K and (c) 9K. When the temperature became lower, the antiprotons stay alive for longer time.

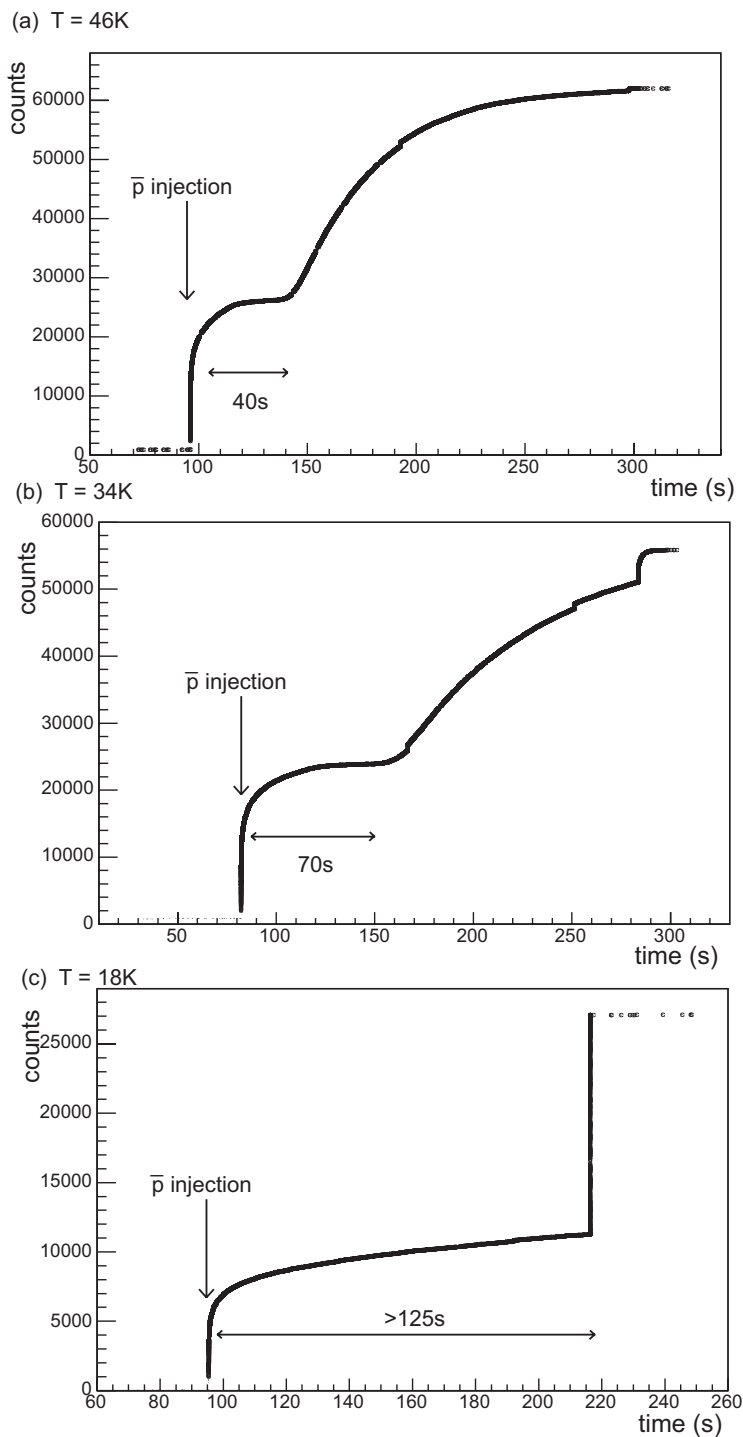


Figure 3.18: Integrated annihilation counts of antiprotons without electrons: (a) the bore tube temperature was around 46 K, (b) 34 K and (c) 18K. When the temperature was lower, the antiprotons were not cooled because no coolants existed in the MRT.

at higher temperatures, 34 K and 46 K, antiprotons were somehow cooled, because electrons were produced through ionization of residual gases. The time duration before the start of annihilation was longer than the preloaded case in Fig. 3.17, because the number of produce electrons were much smaller.

Chapter 4

Cooling of antiprotons in the MRT

In the MRT, a cloud of well cooled charged particles cloud behaves as a nonneutral plasma. Here the cooling feature of antiprotons in the MRT and the behavior of electron-antiproton two component nonneutral plasma are discussed.

4.1 Electrostatic modes of the electron plasma

4.1.1 Axially symmetric electrostatic modes

In this work, electrons were confined in the MRT installed in the cold bore tube whose temperature was less than 10 K. At such cryogenic temperature the Debye length $\lambda_D \equiv \sqrt{\epsilon_0 k_B T / n q^2}$ (App. C.2) is usually smaller than the size of the charged particles' cloud, so that the cloud can be taken as a plasma. (Typically, $\lambda_D \sim 3 \times 10^{-2}$ mm, the radius of plasma $b = 5$ mm and the axial half length $a = 30\text{--}45$ mm.)

The normal modes of a cold pure ion plasma, that is to say, nonneutral plasma, have been studied [73] [74]. The dispersion relation of a nonneutral plasma is analytically known for only two cases, a uniform infinity long column, which is called Trivelpiece-Gould mode [75], and a cold spheroidal plasma derived by D.H.E. Dubin [76].

In the following, the mode frequency of a nonneutral spheroidal plasma with a finite temperature is discussed.

Assume a two component plasma consisting of electrons and antiprotons with uniform densities, n_e and $n_{\bar{p}}$, in a uniform magnetic field, \mathbf{B}_0 , in stationary state. For disturbance

expressed as $\exp(i(\mathbf{k} \cdot \mathbf{r} - \omega t))$, electric and magnetic fields (\mathbf{E} and \mathbf{B}') are induced together with a current given by

$$\mathbf{j} = n_e q_e \mathbf{v}_e + n_{\bar{p}} q_{\bar{p}} \mathbf{v}_{\bar{p}}. \quad (4.1)$$

The electric displacement \mathbf{D} and current \mathbf{j} are

$$\mathbf{D} = \epsilon_0 \mathbf{E} + \mathbf{P} \equiv \epsilon(\mathbf{k}, \omega) \cdot \mathbf{E}, \quad (4.2)$$

$$\mathbf{j} = \frac{\partial \mathbf{P}}{\partial t} = -i\omega \mathbf{P}, \quad (4.3)$$

respectively, where \mathbf{P} is electric polarization, ϵ_0 is a dielectric constant of vacuum. Therefore \mathbf{D} is rewritten as

$$\mathbf{D} = \epsilon_0 \mathbf{E} + \frac{i}{\omega} \mathbf{j}. \quad (4.4)$$

The equation of motions for a single particle is

$$m \frac{d\mathbf{v}}{dt} = q(\mathbf{E} + \mathbf{v} \times \mathbf{B}), \quad (4.5)$$

where $\mathbf{B} = \mathbf{B}_0 + \mathbf{B}'$. Here \mathbf{v} , \mathbf{E} and \mathbf{B}' are of first order minuteness. Then the above equation is reduced to

$$-i\omega m \mathbf{v} = q(\mathbf{E} + \mathbf{v} \times \mathbf{B}_0). \quad (4.6)$$

From the Eqs. (4.1),(4.2),(4.4) and (4.6), the dielectric tensor elements along the magnetic field axis, $\hat{z} \parallel \mathbf{B}_0$, is expressed as

$$\epsilon(\mathbf{k}, \omega) = \epsilon_0 \begin{pmatrix} \epsilon_1 & -\epsilon_2 & 0 \\ \epsilon_2 & \epsilon_1 & 0 \\ 0 & 0 & \epsilon_3 \end{pmatrix}, \quad (4.7)$$

where

$$\epsilon_1 = 1 - \left[\frac{\omega_{pe}^2}{\omega^2 - \omega_{ce}^2} + \frac{\omega_{p\bar{p}}^2}{\omega^2 - \omega_{c\bar{p}}^2} \right], \quad (4.8)$$

$$\epsilon_2 = i \left[-\frac{\omega_{ce} \omega_{pe}^2}{\omega(\omega^2 - \omega_{ce}^2)} - \frac{\omega_{c\bar{p}} \omega_{p\bar{p}}^2}{\omega(\omega^2 - \omega_{c\bar{p}}^2)} \right], \quad (4.9)$$

$$\epsilon_3 = 1 - \left[\frac{\omega_{pe}^2}{\omega^2} + \frac{\omega_{p\bar{p}}^2}{\omega^2} \right]. \quad (4.10)$$

Here $\omega_{cj} = |q_j B_0|/m_j$ is cyclotron frequency for particle- j (e or \bar{p}), and $\omega_{pj} = \sqrt{n_j q^2/m_j \epsilon_0}$ is the plasma frequency (App. C.1).

In the case where the Debye length is sufficiently short compared with the plasma radius a , *i.e.*, $\lambda_D = \sqrt{\epsilon_0 k_B T / (q^2 (n_e + n_{\bar{p}}))} \ll a$, the plasma boundary can be regarded as a surface. As far as this condition is satisfied, Dubin's method to find the dispersion relation of cold spheroidal plasma is applicable to the finite temperature plasma. This dispersion relation is found by connecting the electric field inside and outside the plasma at the boundary [76]. It is thus written as

$$\epsilon_3 + m\alpha \left(\alpha^2 - \frac{\epsilon_3}{\epsilon_1} \right)^{\frac{1}{2}} \frac{P_l^m}{P_l^{m'}} \epsilon_2 = \left(\frac{\alpha^2 - \epsilon_3/\epsilon_1}{\alpha^2 - 1} \right)^{\frac{1}{2}} \frac{P_l^m Q_l^{m'}}{P_l^{m'} Q_l^m}, \quad (4.11)$$

where $\alpha = b/a$ is the aspect ratio of the plasma defined as the ratio of the axial half length, b , to the radius, a . The Legendre functions of the first and second kinds are

$$P_l^m = P_l^m \left(\frac{\alpha}{\sqrt{\alpha^2 - \epsilon_3/\epsilon_1}} \right), \quad (4.12)$$

$$Q_l^m = Q_l^m \left(\frac{\alpha}{\sqrt{\alpha^2 - 1}} \right), \quad (4.13)$$

where $P_l^{m'}$ and $Q_l^{m'}$ denote their derivatives. The index (l, m) denotes an axial and azimuthal dependence on the plasma modes, respectively.

We are interested in high frequency modes where $\omega \gg \omega_r$. Here ω_r is a rigid rotor frequency of the plasma (See App. C.3). Under the strong magnetic field condition, $\omega_r/\omega_c \ll 1$, then the tensor elements, Eqs.(4.8)–(4.10) are approximated as

$$\epsilon_1 \sim 1, \quad (4.14)$$

$$\epsilon_2 \sim 0, \quad (4.15)$$

$$\epsilon_3 \sim 1 - \frac{\omega_{pe}^2}{\omega^2} \quad (4.16)$$

Since the density of antiprotons in the plasma was typically two orders of magnitude smaller in this work, the rigid rotor frequency for antiproton plasma, $\omega_{p\bar{p}}$ can be neglected in Eq. (4.16).

Combining Eqs. (4.11), (4.14), (4.15) and (4.16), the dispersion relation of cold spheroidal plasma for axially symmetric case ($m = 0$) has been derived to be [73]

$$\varepsilon_3 = \left(\frac{\alpha^2 - \varepsilon_3}{\alpha^2 - 1} \right)^{\frac{1}{2}} \frac{P_l(k_1)Q_l'(k_2)}{P_l'(k_1)Q_l(k_2)}, \quad (4.17)$$

for a strong magnetic field at finite temperature T_e , where $k_1 = \alpha(\alpha^2 - \varepsilon_3)^{-1/2}$, $k_2 = \alpha(\alpha^2 - 1)^{-1/2}$. Equation (4.17) shows that the dispersion relation formulated for a cold spheroidal plasma depends on the aspect ratio.

Here suppose the plasma temperature is finite. Equation (4.5) can be rewritten as

$$m \frac{d\mathbf{v}}{dt} = q(\mathbf{E} + \mathbf{v} \times \mathbf{B}) + \nabla p_e^{\parallel}, \quad (4.18)$$

where p_e^{\parallel} is anisotropic pressure parallel to the z -direction. The adiabatic equation is

$$\frac{1}{p_e^{\parallel}} \frac{dp_e^{\parallel}}{dt} = \frac{\gamma}{n_e} \frac{dn_e}{dt}, \quad (4.19)$$

γ is the ratio of specific heats for one-dimensional expansion. Then Eq. (4.16) are rewritten as

$$\varepsilon_3 \sim 1 - \left(\frac{\omega_{pe}^2}{\omega^2 - \gamma k^2 k_B T_e / m_e} \right), \quad (4.20)$$

where $k \approx \pi(l-1)/(2b)$ is the longitudinal wave number for $(l,0)$ mode, ω is the angular frequency of the electrostatic oscillation of the plasma, k_B is the Boltzmann constant, and T_e is the temperature of the electron plasma. Then ε_3 is approximately given by

$$\varepsilon_3 \approx 1 - \frac{\omega_{pe}^2}{\omega^2} \left(1 + \frac{k_B T_e}{m_e} \frac{3k^2}{\omega^2} \right), \quad (4.21)$$

where $\gamma = 3$ [77] [78].

From Eqs. (4.17) and (4.21), the relation between ω and T_e is derived. Since the plasma frequency, ω_p , depends on its density, ω depends on its density, as well as on the aspect ratio of the plasma as described above.

Figure 4.1 shows a schematic drawing of the normal modes of a spheroidal nonneutral plasma. As is seen, $(1,0)$ mode corresponds to the center of mass motion of the plasma.

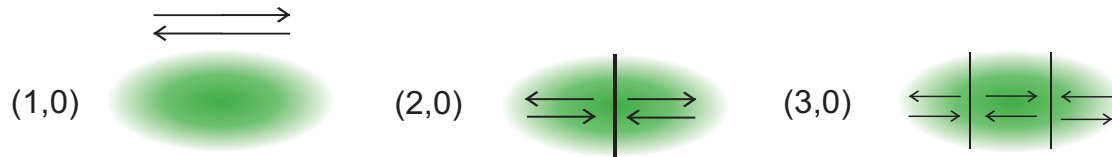


Figure 4.1: Schematic drawing of axially symmetric modes.

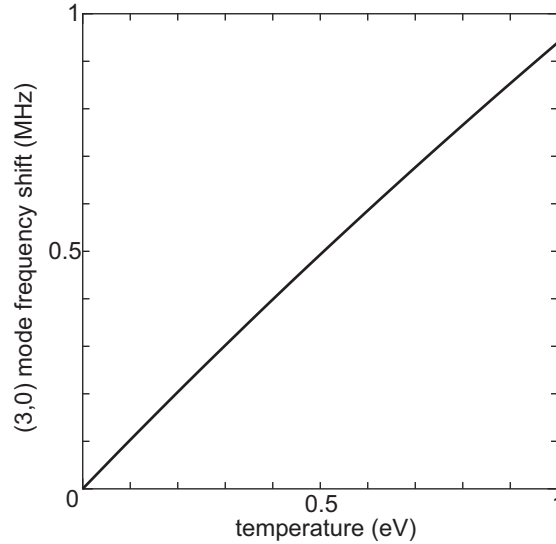


Figure 4.2: (3,0) mode frequency shift against the temperature of the electron plasma.

The charge distributions of these modes are axially symmetric and have zero, one and two nodes along the axial direction, respectively.

Figure 4.2 shows the electron plasma's (3,0) mode frequency shift against the temperature of the plasma derived from Eqs. (4.17) and (4.21).

4.1.2 Observed axially symmetric modes of electron plasma

The frequencies of ($l,0$) modes ($l = 0-7$) were measured by exciting these modes with white noise applied to the electrode BH2 of the MRT. The asterisks plotted in Fig. 4.3 show the observed frequencies.

The squares, circles and triangles are the mode frequencies calculated for the plasmas with diameter 5, 10 and 20 mm, respectively, containing 3×10^8 electrons in a harmonic potential of 50 V and of 12.5 cm long. In the calculation, the plasma temperature was

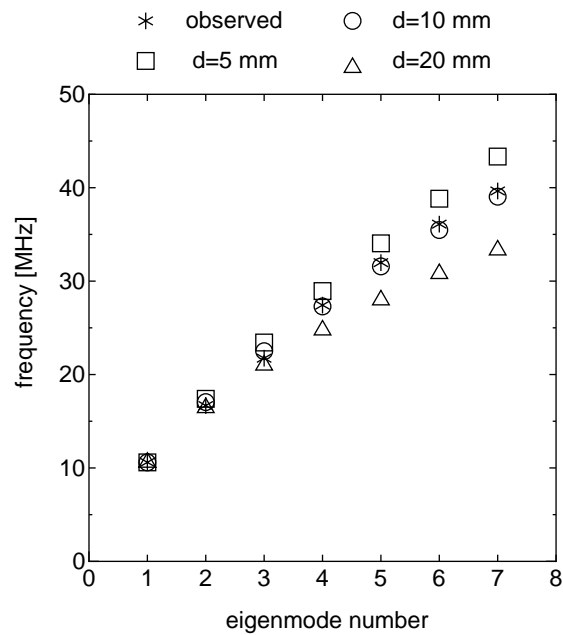


Figure 4.3: Electrostatic eigenmodes v.s. their frequencies for observed (*) and calculated values for various diameter of the plasma, $d = 5$ mm (square symbol), 10 mm (circle) and 20 mm (triangle).

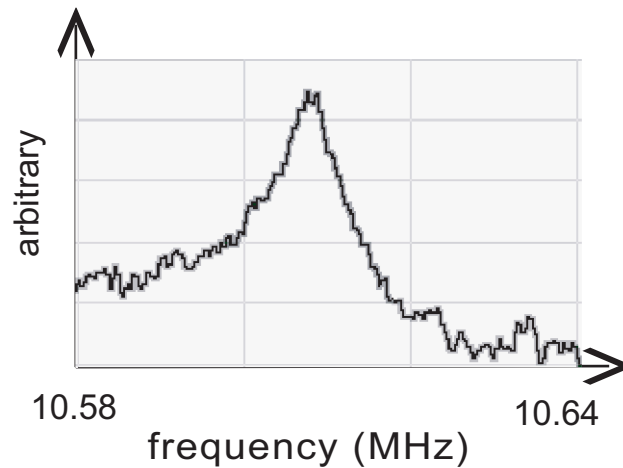


Figure 4.4: An example of power spectra of the (1,0) mode obtained by applying a white noise. In this case the shape of the spectrum was like a peak.

assumed to be 10 K, the environmental temperature of the MRT. It is seen that the electron plasmas formed had the diameter of about 10 mm.

Figure 4.4 shows an example of power spectra of the (1,0) modes when a noise was

applied. The shape of the (1,0) mode spectrum appeared as a simple a peak. On the other hand, in the case of (2,0) and (3,0) modes, the peaks were followed by dips on the high-frequency side (a Fano-profile), which are explained as the difference of impedance of the electron plasma for absorption of applied noise [79].

By this way, the plasma modes were monitored during the antiproton injection and the cooling. Figure 4.5 is an example of the time evolution of the power spectrum where the resonances corresponding to the (1,0), (2,0) and (3,0) modes are clearly observed. The resonance frequency of the (1,0) mode was almost constant during and after the antiproton injection. This figure is compared with the frequencies of the (2,0) and (3,0) modes, which increased after the antiproton injection, reached a maximum in a few seconds, and then slowly returned to the initial frequencies. Such a frequency variation is due to heat-up of the electron plasma by the antiproton injection followed by the cooling with synchrotron radiation. As has already been explained, the (1,0) mode frequency has no temperature dependence.

4.2 Electron cooling feature

Antiprotons injected to the MRT decrease their energy via Coulomb collisions with electrons. The preloaded electrons lose their energy continuously via synchrotron radiation in the strong magnetic field and are in a thermal equilibrium with surrounding wall (~ 10 K). This feature is called “electron cooling”.

As has been shown in the previous subsection, several plasma modes were observed by continuously applying noise during the antiproton injection and the cooling, which allowed to estimate the temperature evolution and accordingly the cooling feature of antiprotons nondestructively. However, the application of noise inevitably increased the plasma temperature and did not allow precise measurements.

In order to monitor the plasma modes still minimizing the heat-up, we used a pulse excitation technique described in Sec. 4.2.1.

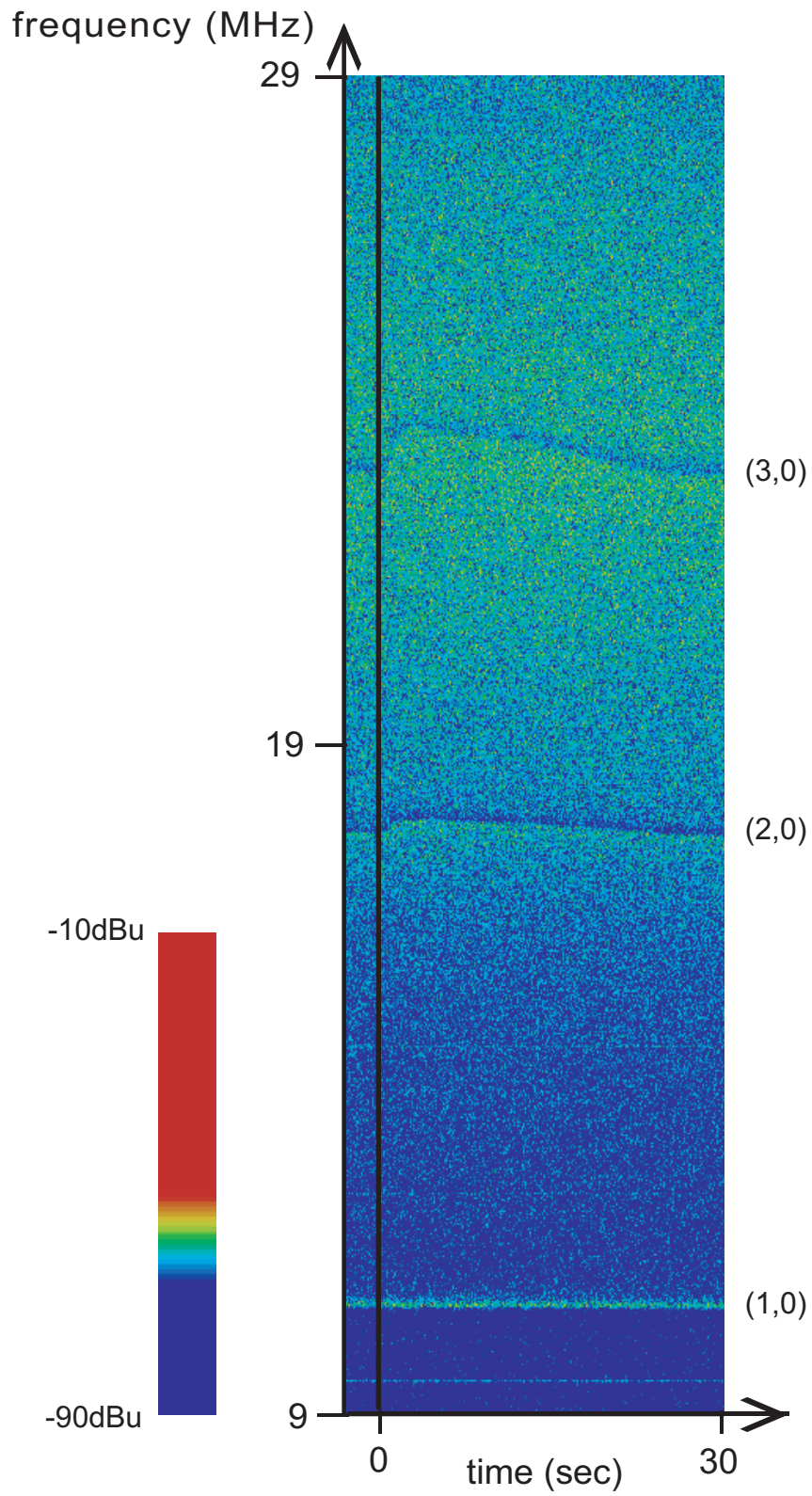


Figure 4.5: Experimentally obtained (1,0), (2,0) and (3,0) modes of electron plasma.

4.2.1 Experimental setup

To measure the frequency shift of the electron plasma mode minimizing heat-up, a pulse excitation technique was applied, which schematically shown in Fig. 4.6.

A pulse train of a few tens microseconds with the repetition rate of 1 Hz was applied to an electrode, e.g., BH1 of the MRT, and the induced oscillations were monitored by another electrode, say BH2, of the MRT. The pulse width was chosen to be the shortest still allowing the observation of the plasma mode. Figure 4.7 shows an example of the excitation pulse and the induced oscillation, the amplitude of which decreased with a time constant of $\sim 30 \mu\text{s}$ corresponding to the life time of the mode. The amplitude of the induced oscillation was measured as a function of the frequency of the excitation pulse to find the resonance frequency correctly. The frequency of the mode was analyzed using FFT (Fast Fourier Transformer) after the excitation pulse had over (the time region transformed was indicated by “FFT” in Fig. 4.7).

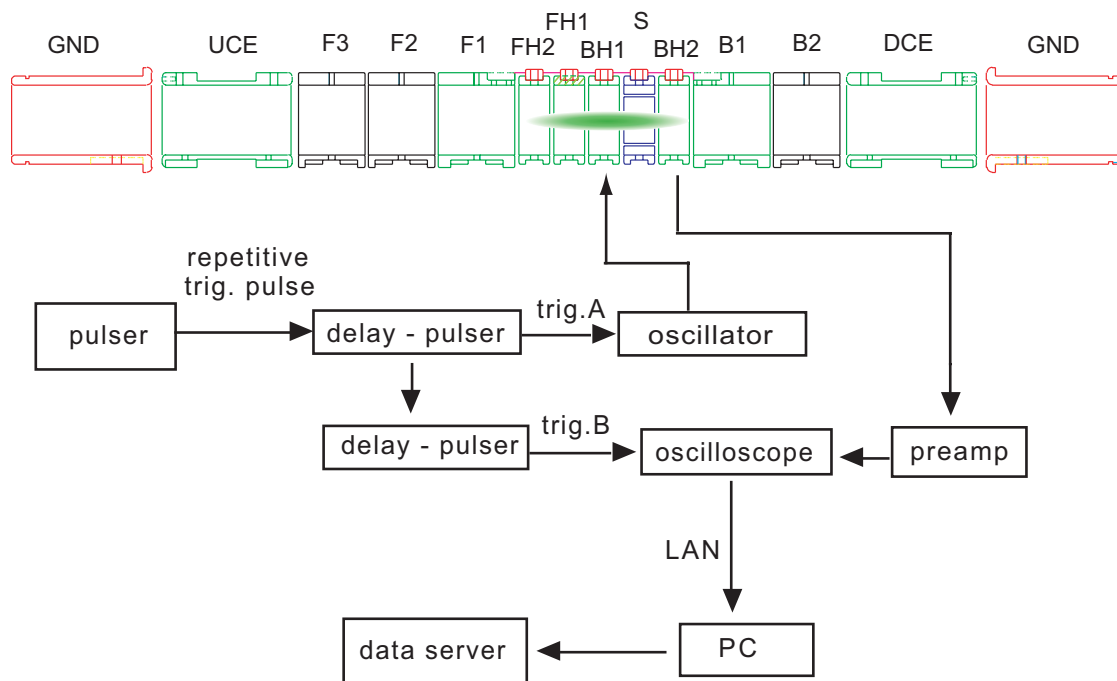


Figure 4.6: The experimental scheme of electrostatic mode detection



Figure 4.7: An example of the excitation pulse (1) and the induced mode (2).

4.2.2 Synchrotron radiation cooling of electrons

A single classical electron makes a circular motion in a uniform magnetic field, namely cyclotron motion. The cyclotron frequency is 70 GHz at 2.5 T with its Larmor radius $r_c = v_{\perp}/\omega_c \sim 30$ nm for a 1 meV (≈ 10 K) electron. The energy loss rate at $v \ll c$ is given by [80]

$$\frac{dE_{\perp}}{dt} = -\frac{q^2}{6\pi\epsilon_0 c^3} \dot{v}_{\perp}^2 = -\frac{2q^2 \omega_c^2}{3\pi\epsilon_0 m_e c^3} E_{\perp}, \quad (4.22)$$

where $\dot{v}_{\perp} = \omega_c v_{\perp}$ and $E_{\perp} = m_e v_{\perp}^2/2$. When the velocity distribution of electrons in the plasma is assumed to be as a Maxwellian distribution, Eq. (4.22) is reduced to

$$\frac{dT_{\perp}}{dt} = -\frac{3T_{\perp}}{2\tau_c}, \quad (4.23)$$

where $T_{\perp} = \langle E_{\perp} \rangle$ and τ_c , the synchrotron radiation cooling time, is defined by

$$\tau_c \equiv \frac{3\pi\epsilon_0 m_e c^3}{q^2 \omega_c^2}. \quad (4.24)$$

The synchrotron radiation cooling time was experimentally estimated with the present experimental setup. The temperature relaxation time from 2.5 eV to 0.3 eV was measured by monitoring the (2,0) mode frequency shift after heating up the electron plasma [53] [77]. It was found that the cooling time is given by $\tau_c \sim 6/B[\text{T}]^2$ s, which is 1.5 times longer than the prediction of Eq. (4.24) in a free space. This originates from the fact that the electron plasma was surrounded by metallic walls with finite size, which suppress the longer wavelength synchrotron radiation (a cavity QED) [53] [80].

4.2.3 The frequency shift of the (3,0) mode

In this subsection, we concentrate on the (3,0) mode, because the (3,0) mode is more sensitive to the plasma temperature than the (2,0) mode as is seen in Fig. 4.5.

Figure 4.8 shows the time evolution of the (3,0) mode frequency of the electron plasma as a function of time. It is seen that the frequency increased within the first 5 s, kept the frequency for 10 s or so, and then returned to the original frequency with a time constant of more than ten seconds which is longer than the synchrotron radiation cooling time $\tau_c \sim 6/B^2$ s. The maximum frequency shift corresponds to the temperature rise of ~ 0.6 eV.

The frequency shifts were simulated dividing the electron cooling process into two phases. In the first phase, antiprotons were energetic enough and confined between the UCE and DCE as shown in Fig. 4.9, where the injected antiproton beam is decelerated by the electron plasmoid. During the deceleration, the antiproton beam gradually diffuses in its velocity-space. The velocity parallel to the magnetic field $v_{\bar{p}\parallel}$ diffuses to the perpendicular component $v_{\bar{p}\perp}$. In the present condition, the diffusion time from $v_{\bar{p}\parallel}$ to $v_{\bar{p}\perp}$ is much longer than the deceleration time of the longitudinal energy. For the antiproton with $E_{\bar{p}} = 10$ keV, the diffusion time becomes $\sim 10^4$ s [81], while the deceleration time is ~ 10 s. Therefore the energy deposit of the antiproton beam to the electron plasma is estimated by considering only the deceleration process of the longitudinal energy.

The second phase starts when the antiproton energy is decreased enough, i.e., the Larmor radius r_c becomes shorter than the Debye shielding length λ_D , and antiprotons uni-

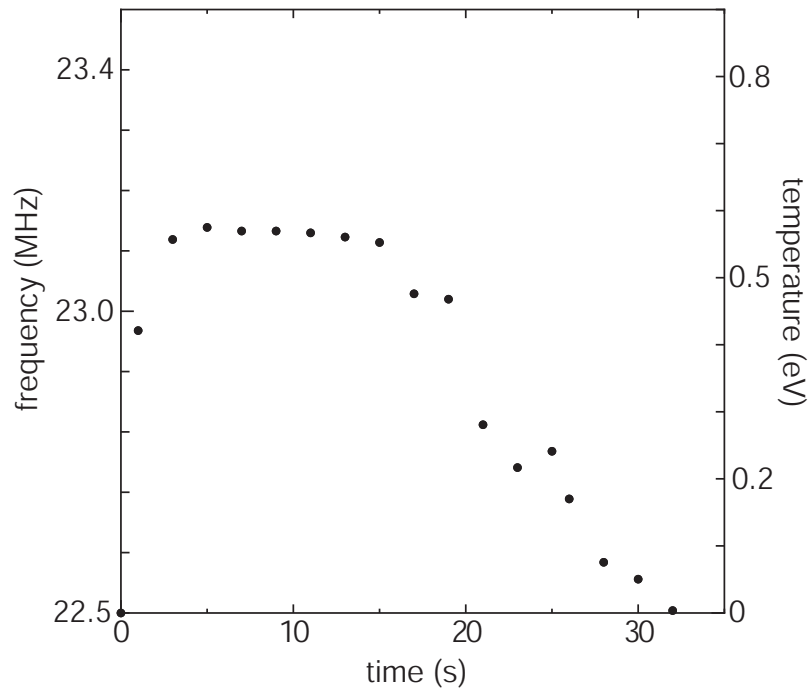


Figure 4.8: Observed frequency shift of the (3,0) mode. Right vertical axis shows the temperature translated from the frequency shift.

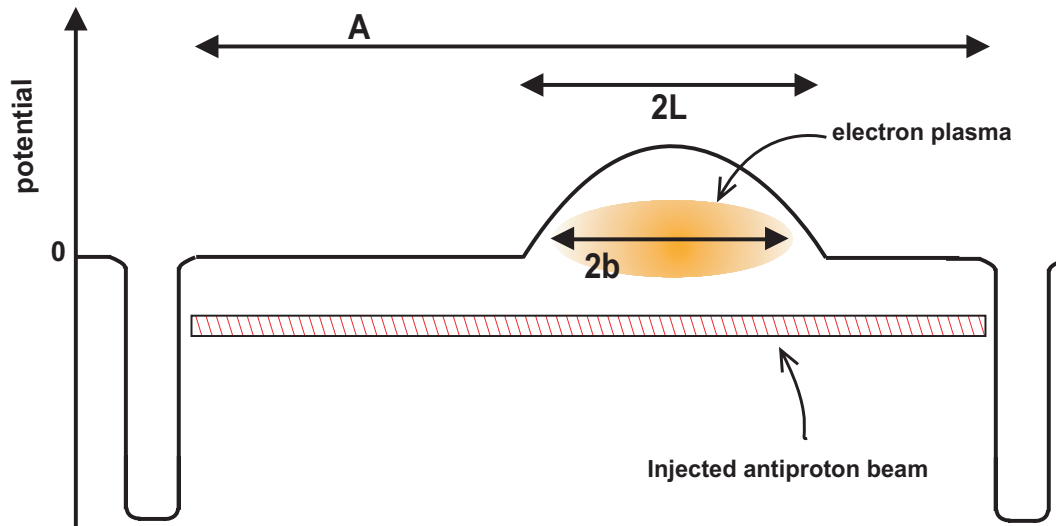


Figure 4.9: Potential distribution along the trap axis.

formly mixed with electrons, the energy equipartition [82] between electrons and antiprotons should be taken into account.

Deceleration of antiproton beam

Here the energy deposition of the injected antiproton beam to the electron plasma is considered for the first phase. We considered the energy exchange between a beam of antiprotons and one of the electron plasma components, which consists of identical particles characterized by a Maxwellian velocity distribution. Then the energy transfer rate from the beam to the plasma, S , is given by [83]

$$S(T_e, E_{\bar{p}}) = a \frac{n_e q^4 \log \Lambda(T_e, E_{\bar{p}})}{4\pi \epsilon_0^2 m_e v_{\bar{p}}(E_{\bar{p}})} f(T_e, E_{\bar{p}}), \quad (4.25)$$

where T_e is the temperature of the electron plasma, $E_{\bar{p}}$ is the energy of antiprotons beam, n_e is the density of electrons plasma, v_e and $v_{\bar{p}}$ is the velocity of electron and antiproton, m_e and $m_{\bar{p}}$ is the mass of electron and antiproton, and q is the charge. Coupling factor a between the beam and the plasma is defined as

$$a = 2b/A \quad \text{for } E_{\bar{p}} \geq q\phi_s$$

$$a = b/L \quad \text{for } E_{\bar{p}} < q\phi_s,$$

where $A = 0.32$ m is the distance between the high-voltage electrodes, UCE and DCE, as shown in Fig. 4.9, $2L$ is the axial length of the harmonic region and $2b$ is the axial length of the electron plasma. The injected beam bounced between the electrodes UCE and DCE in the earlier deceleration phase, where $a = 2b/A$. However, when the energy of antiproton beam decreased to $E_{\bar{p}} < q\phi_s$ where $\phi_s = 28.6$ V is the harmonic potential including the image charge effect, antiprotons fall into the harmonic potential well with the length $2L$. Then the factor becomes $a = b/L$. The electron distribution supposed to be isotropic in velocity space is given by [83],

$$f(T_e, E_{\bar{p}}) = F \left(\sqrt{\frac{m_e}{2k_B T_e}} \right) v_{\bar{p}}(E_{\bar{p}}), \quad (4.26)$$

with Landau parameter and Coulomb logarithm,

$$L(T_e, E_{\bar{p}}) = \frac{q^2}{4\pi \epsilon_0 m_e (v_e + v_{\bar{p}})^2}, \quad (4.27)$$

$$\log \Lambda(T_e, E_{\bar{p}}) = \log \left(\frac{\lambda_D(T_e)}{L(T_e, E_{\bar{p}})} \right), \quad (4.28)$$

respectively. Here the calculation was carried out for electrons with Maxwellian velocity distribution by using the following functions including error function, $\Phi(x)$, and Coulomb collision cooling, $F(x)$, defined as follows;

$$\Phi(x) = \frac{2}{\sqrt{\pi}} \int_0^x \exp(-t^2) dt, \quad (4.29)$$

$$F(x) = \Phi(x) - \frac{2x}{\sqrt{x}} \left(1 + \frac{m_e}{m_{\bar{p}}} \right) \exp(-x^2), \quad (4.30)$$

where the velocity of antiproton, $v_{\bar{p}}$, that of electron, v_e and the Debye length λ_D at temperature T_e are

$$v_{\bar{p}}(E_{\bar{p}}) = \sqrt{\frac{2E_{\bar{p}}}{m_{\bar{p}}}}, \quad (4.31)$$

$$v_e(T_e) = \sqrt{\frac{k_B T_e}{m_e}}, \quad (4.32)$$

$$\lambda_D(T_e) = \sqrt{\frac{\epsilon_0 k_B T_e}{q^2 n_e}}. \quad (4.33)$$

The antiproton beam emerging from the degrader foils was not a monochromatic beam, and so the energy distribution of the beam is expressed by $G(E_{\bar{p}}, t)$. For simplicity, interactions among antiprotons with different momentum were neglected. Under this condition, the number of antiprotons of each momentum component $dN_{\bar{p}}$ is conserved during the deceleration process, that is to say,

$$dN_{\bar{p}} = G(E_{\bar{p}}, t) dE_{\bar{p}}(t) = \text{const}. \quad (4.34)$$

Considering the synchrotron radiation cooling time, $\tau_c \sim 6/B^2$, the energy transfer between the beam to the plasma is found by solving the following simultaneous equations with respect to time t :

$$\frac{dE_{\bar{p}}(t)}{dt} = -S(T_e(t), E_{\bar{p}}(t)), \quad (4.35)$$

$$\frac{dT_e(t)}{dt} = \frac{2}{3k_B} \left(\frac{N_{\bar{p}}}{N_e} \right) S(T_e(t), E_{\bar{p}}(t)) - \frac{T_e(t)}{\tau_c}, \quad (4.36)$$

with initial values $E_{\bar{p}}(0)$ and $T_e(0)$.

Here the following parameters were used as the initial conditions at $t = 0$; For the electron plasma,

$$\begin{aligned} N_e &= 3 \times 10^8, \text{ total number of electrons} \\ r &= 0.006 \text{ m, radius of the electron plasma} \\ \alpha &= 7.34, \text{ aspect ratio of the electron plasma} \\ n_e &= 4.4 \times 10^{13} / \text{m}^3, \text{ density of the electron plasma} \\ T_e(0) &= 10 \text{ K, temperature of the electron plasma} \end{aligned}$$

The total number of injected antiprotons:

$$N_{\bar{p}} = 3 \times 10^5.$$

And other parameters;

$$\begin{aligned} B &= 2.5 \text{ T, magnetic field strength} \\ \tau_c &\sim \zeta / B^2 = 6 / B^2 \text{ s, synchrotron radiation cooling time.} \end{aligned}$$

The energy variation of various initial energy components $G(E_{\bar{p}}, 0)$ of the injected antiproton beam bounced between the high-voltage potential barriers in the first deceleration phase is shown in Fig. 4.10 (a), where coupling factor $a = 2b/A$. It is seen that the lower the energy, the faster the energy loss, i.e., the low energy components shortens the rise time of T_e , while the higher energy components contribute to hold $T_e(t)$ by supplying energies to the electron plasma in the later phase of the cooling.

Equipartition between T_e and $T_{\bar{p}}$

Once the energy of the beam component decreased to $E_{\bar{p}} \leq q\phi_s$, the antiprotons fall into the harmonic potential well (“HPW” in Fig. 4.10). Suppose that the antiprotons were decelerated and mixed with the electron plasma completely but $T_{\bar{p}}$ is still higher than T_e , in this situation equilibration through Coulomb collisions between $T_{\bar{p}}$ and T_e proceeds. At this phase, the beam is replaced by an identical particles group subject to a Maxwellian

distribution with temperature T . It is difficult to determine an appropriate time at which equipartition model becomes applicable instead of the beam damping model. In this calculation this switching time is chosen as $t = 20$ s, when $T_e = 0.38$ eV, the component of $E_{\bar{p}}(0) = 3$ keV damped to 0.55 eV, where the Larmor radius was much smaller than Debye length. The equipartition process can be followed by solving the simultaneous equations;

$$\frac{dT_{\bar{p}}(t)}{dt} = -\frac{T_{\bar{p}}(t) - T_e(t)}{\tau_{\bar{p}e}(T_e(t), T_{\bar{p}}(t))}, \quad (4.37)$$

$$\frac{dT_e(t)}{dt} = \frac{T_{\bar{p}}(t) - T_e(t)}{\tau_{e\bar{p}}(T_e(t), T_{\bar{p}}(t))} - \frac{2(T_e(t) - T_{\text{wall}})}{3\tau_c}, \quad (4.38)$$

with the initial values $T_e(0)$ and $T_{\bar{p}}(0)$. Here $T_{\text{wall}} = 10$ K is the environmental temperature. The factor $2/3$ in the second term of Eq. (4.38) comes from the $T_{\perp} = T_{\parallel} = T$, which is a good approximation when the equipartition rate is enough longer than the synchrotron radiation cooling time. Here two functions giving equipartition times, $\tau_{\bar{p}e}$ and $\tau_{e\bar{p}}$, are defined as [83];

$$\tau_{\bar{p}e}(T_e, T_{\bar{p}}) = \frac{3\sqrt{2}\pi^{3/2}\epsilon_0^2 m_{\bar{p}} m_e}{n_e q^4 \log \Lambda(T_e, T_{\bar{p}})} \left(\frac{k_B T_e}{m_e} + \frac{k_B T_{\bar{p}}}{m_{\bar{p}}} \right)^{\frac{3}{2}}, \quad (4.39)$$

$$\tau_{e\bar{p}}(T_e, T_{\bar{p}}) = \frac{3\sqrt{2}\pi^{3/2}\epsilon_0^2 m_{\bar{p}} m_e}{n_{\bar{p}} q^4 \log \Lambda(T_e, T_{\bar{p}})} \left(\frac{k_B T_e}{m_e} + \frac{k_B T_{\bar{p}}}{m_{\bar{p}}} \right)^{\frac{3}{2}}. \quad (4.40)$$

By solving a series of equations Eq.(4.25)–(4.40), time evolution of $T_e(t)$ was obtained as a result shown in Fig. 4.10 (b).

It is seen that the variations of the plasma frequencies during cooling after the heat-up were consistently reproduced by the abovementioned calculation which took into account the beam damping and the equipartition model including synchrotron radiation cooling of electrons with the time constant $\sim 6/B[\text{T}]^2$ s.

4.3 The frequency shift of the (1,0) mode

The time evolution of FFT signals of (1,0) mode oscillation is shown in Fig. 4.11, where $\Delta f = 0$ was measured with respect to the (1,0) mode frequency for the trap depth of 50 V, $f_c = 10.59$ MHz if the image charge is neglected. The shift reached ~ 40 kHz at ~ 20 s

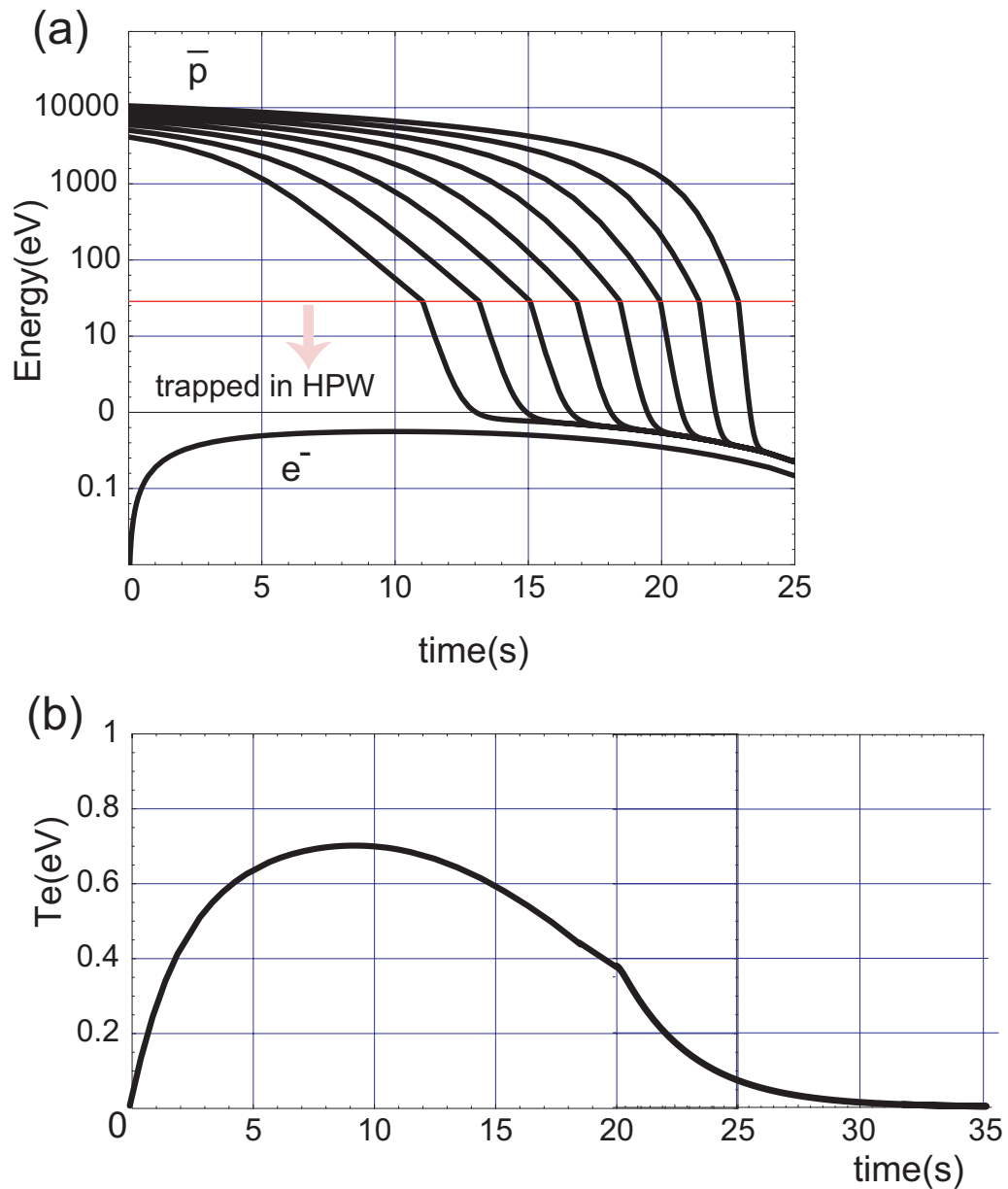


Figure 4.10: (a) Energy variation of the electron plasma and antiproton beam components whose initial energy was from 3 keV to 10 keV with 1 keV step, which calculated with beam deceleration model. (b) Temperature variation of the electron plasma calculated with beam deceleration model in $0 \leq t \leq 20$ and with equipartition model in $20 \leq t$.

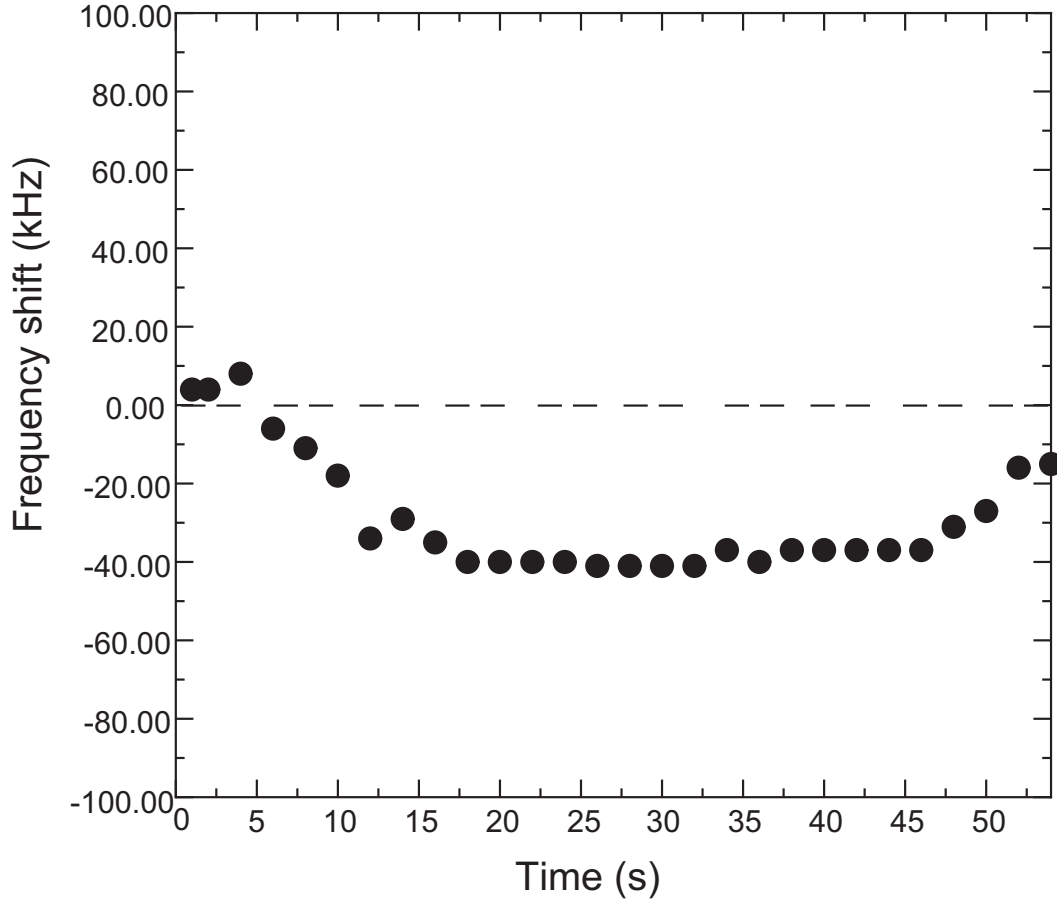


Figure 4.11: Frequency shift of (1,0) mode. Dashed line is the original frequency without antiproton injection.

after the antiproton injection. It is again noted that the (1,0) mode reflects the center-of-mass motion of the plasma, and has no dependence on the temperature.

The electron cloud in the plasma does the center-of-mass motion, i.e., (1,0) mode, in the combined field, the external field ϕ^{ext} and the self-field of antiprotons $\phi_{\bar{p}}^s$ which works as an additive external potential. Here the axial electric field is

$$E_z = -\frac{\partial}{\partial z} (\phi^{\text{ext}} + \phi_{\bar{p}}^s) \quad (4.41)$$

$$= -\frac{2\phi}{L^2} \left(1 - \frac{N_{\bar{p}}}{N_e + N_{\bar{p}}} \right). \quad (4.42)$$

Therefore the (1,0) mode frequency becomes

$$\omega_{(1,0)} = \omega_{(1,0)}^{\text{el}} \sqrt{1 - \frac{N_{\bar{p}}}{N_e + N_{\bar{p}}}}, \quad (4.43)$$

where

$$\omega_{(1,0)}^{\text{el}} = \sqrt{\frac{-q}{m_e} \frac{2\phi}{L^2}} \quad (4.44)$$

is the frequency for $N_{\bar{p}} = 0$. The downward frequency shift caused by the presence of the antiprotons is approximately given as

$$\Delta = -\frac{\delta\omega_{(1,0)}}{\omega_{(1,0)}^{\text{el}}} \sim -\frac{1}{2} \frac{N_{\bar{p}}}{N_e}, \quad (4.45)$$

for $N_{\bar{p}} \ll N_e$. The downward shift occurs in the mixed plasma composed of electrons and antiprotons.

In the case of Fig. 4.11, where $N_e \sim 7 \times 10^7$ and $N_{\bar{p}} \sim 5 \times 10^5$, $\delta\omega_{(1,0)}/2\pi \sim 38$ kHz, which more or less agree with the obtained frequency shift (Fig. 4.11).

After the cooling, at around 45 s the frequency of the (1,0) mode went to the original

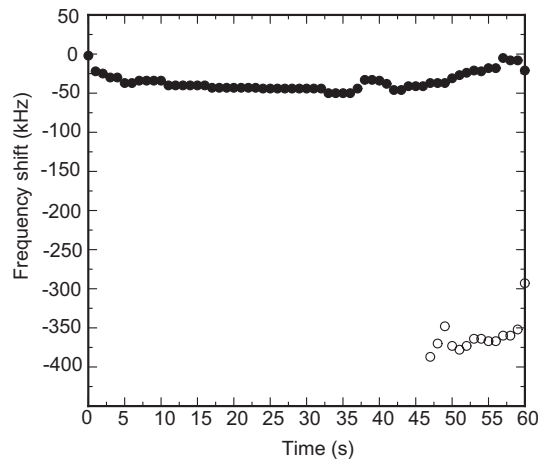


Figure 4.12: Time evolution of (1,0) mode frequency (filled circle) and second peak (opened circle) at the electron density $n_e \approx 7 \times 10^7/\text{cm}^3$.

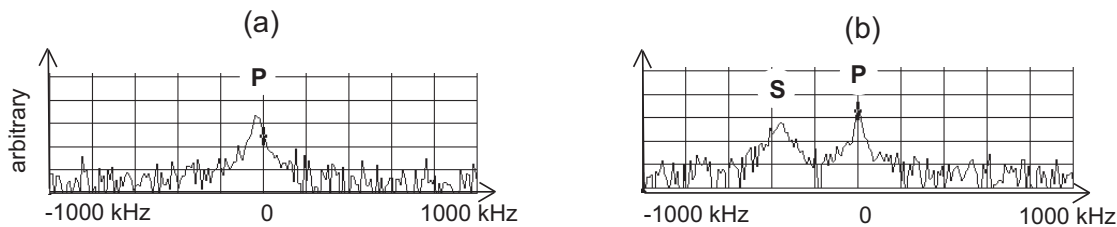


Figure 4.13: Experimentally obtained power spectra of (1,0) mode: (a) at $t = 30$ s, (b) at $t = 55$ s.

value. In a wider range, as shown in Fig. 4.12 and power spectra of the (1,0) mode of the electron plasma in Fig. 4.13, another peak (“S” in Fig 4.13) appeared at about 380 kHz lower than the (1,0) mode frequency for the pure electron plasma at the same time when the frequency shift went to zero. The reason for this is not revealed at this moment, but it may result from the localization of antiprotons around the periphery of the electron plasma by the centrifugal separation [84] [85] (See also Sec. 5.3).

Chapter 5

Extraction and transportation of ultra-slow antiprotons

The extraction and transport of slow antiprotons from the MRT in the strong magnetic field to the experimental target chamber (See App. A) is described.

5.1 Antiproton beam extraction from the MRT

5.1.1 Disturbance by electrons during the slow extraction

The slow extraction of antiprotons was achieved by ramping the harmonic potential well slowly. Figure 5.1 shows annihilation position distribution of antiprotons as a function of the time since their injection at $t = 0$. The annihilation position just after the antiproton injection (see in Fig. 3.15) was around the degrader foil and the MRT. Once the plasma consisting of electrons and antiprotons had stabilized, few additional annihilations were observed until the antiprotons were released over a 100 s long extraction period. The distribution in panels (a) and (b) of this figure refer respectively to cases in which the electron plasma was ejected after its cooling task had been fulfilled, or retained.

After electron cooling, i.e., antiprotons were trapped in the harmonic potential well, the high-voltage potentials were turned off, which timing was around 30 s as was described in the previous chapter. The depth of the harmonic potential was linearly ramped from 50 V to 0 V starting from $t = 55$ s over a period of some 100 s to extract antiprotons from the MRT. In the case of Fig. 5.1 (a), the stored electrons were ejected by opening and

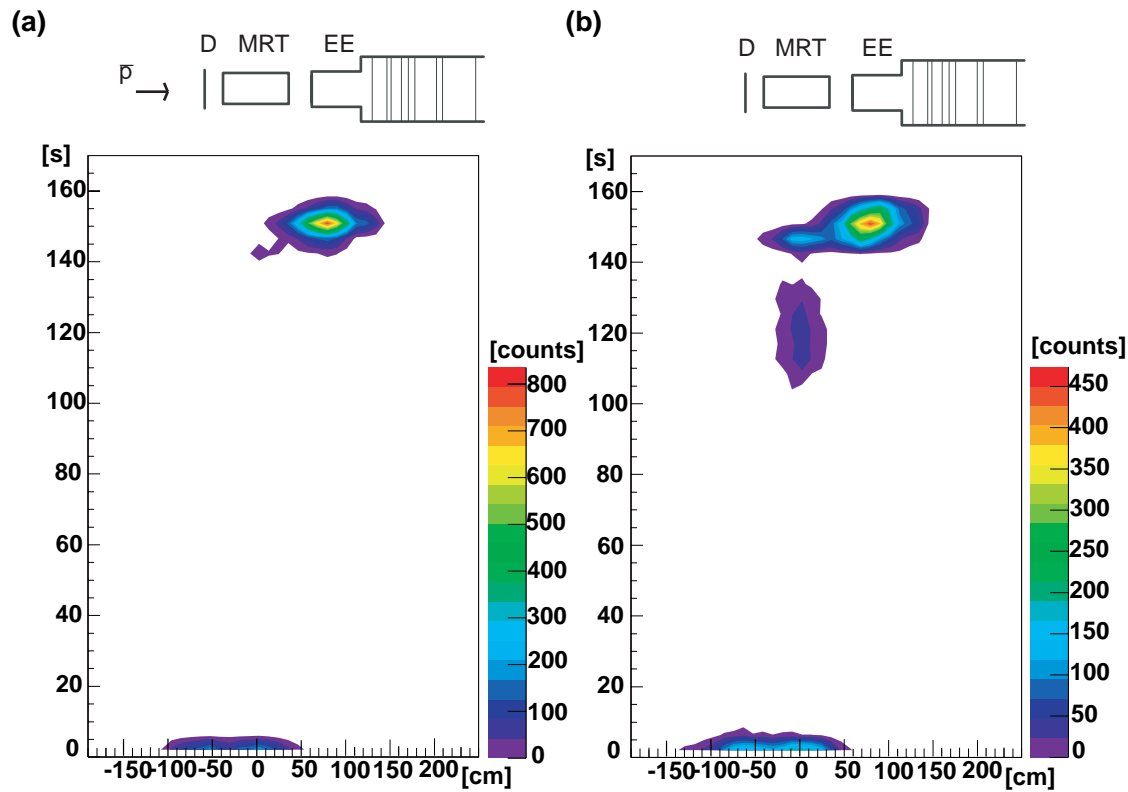


Figure 5.1: Distribution of antiproton annihilation position as a function of the elapsed time since their injection are shown for the case (a) with and (b) without release of electrons at 40 s.

closing the trap three times for 550 ns at $t \sim 40$ s before the extraction procedure. This time duration was long enough to allow the electrons to escape, but short enough to keep the antiprotons, which had much smaller velocity than the others. As expected, almost no annihilations appeared during electron ejection. The fact that none occur between $t = 55$ s when ramping started and $t \sim 140$ s confirms that the antiprotons had been cooled into the bottom of the potential well. The strong annihilation peak observed at $t \approx 150$ s, near the downstream extractor electrode (EE in the figure) contained $\sim 92\%$ of the entire sample of antiprotons trapped in the harmonic potential. From this observation, assuming that the density was constant over the antiprotons cloud, the diameter of the cloud in the MRT was estimated to be ~ 15 – 20 mm from the values of the magnetic field at the extractor electrode which is 10–20% of that around the MRT, and the inner diameter of the extractor electrode which is 50 mm.

Figure 5.1 (b) shows the annihilation pattern when antiprotons were extracted keeping electrons in the trap. Although the main extraction peak was observed at extractor electrode at similar timing, now it included only 78% of the trapped antiprotons, and two peaks additionally appeared near the center of the MRT, at $t \approx 130$ s. When the additional annihilation started at $t \approx 105$ s, the depth of trap potential was ~ 25 V, which is approximately equal to the space charge potential produced by the 3×10^8 electrons in the MRT. The additional annihilation peaks are then attributed to antiprotons hitting the MRT electrodes by the $\mathbf{E} \times \mathbf{B}$ drift because of an instability while the electrons are overflowing from the harmonic potential well. In addition, intermittent bursts of antiproton annihilation were observed during the ramping (Fig. 5.2) in the additional annihilation peak, which may again originate from instabilities of the electron plasma during the variation the trapping potential well.

Summarizing, electron ejection before extraction procedure is effective to avoid antiproton loss due to the disturbance of electrons.

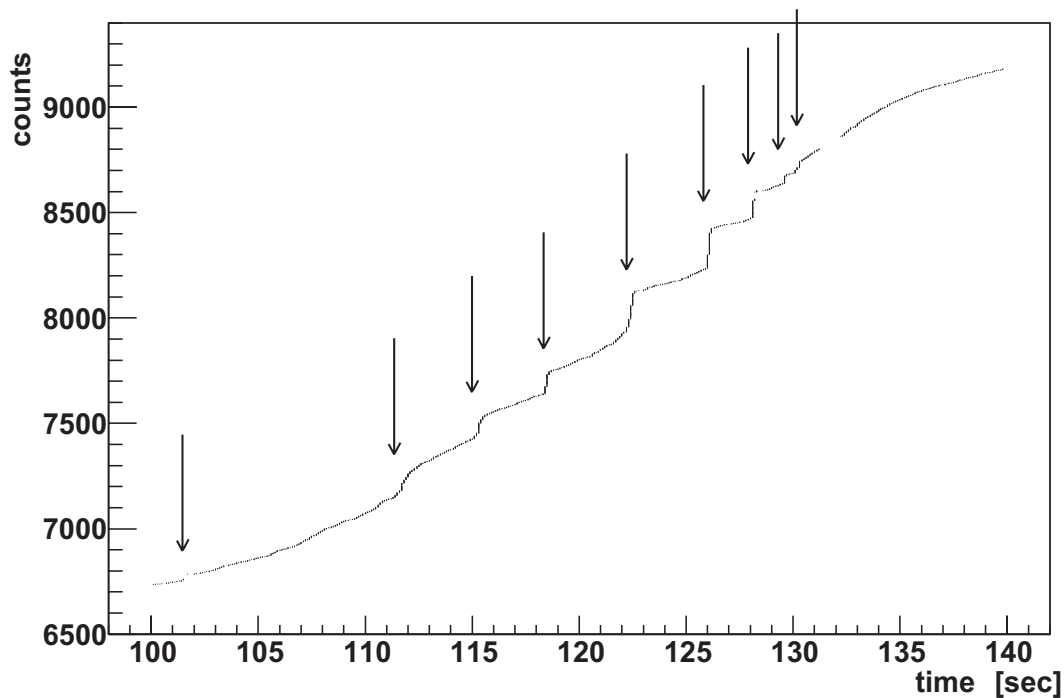


Figure 5.2: Integrated annihilation counts during the potential ramping with electrons. Arrows show some observed “bursts” during the ramping.

5.1.2 Slow extraction of antiprotons from the MRT

For event by event experiments, a continuous beam is often very desirable. As is discussed in Sec 5.1.1, when the potential was ramped linearly, cooled antiprotons were ejected only in the last moment of 3 s out of 100 s-extraction, in which case the antiproton temperature were cooled.

To prepare a continuous ultra-slow antiproton beam with a constant intensity, the ramping rate in the last moment should be decreased, which was realized by scanning the trap potential exponentially like $\phi = \phi_0(1 - \exp(-(t - t_0)/\tau))$, which is shown in Fig. 5.3 together with the case of linear scan. Figure 5.4 compares the extracted beam intensity with the linear and the exponential extraction, where the extracted antiprotons were counted by the MCP located at 165 cm downstream from the center of the MRT. As is seen, the period of beam extraction got longer and the beam intensity was more stable in the case the exponential extraction as compared with the linear extraction. In the exponential case, total duration of extraction procedure can be shorter than the linear extraction still keeping the real extraction time longer, which is convenient to complete the whole procedure including trapping, cooling and extraction within the AD cycle (85–120 s).

5.2 Ultra-slow antiproton beam transport

The annihilation positions of extracted antiprotons in the transport beam line were monitored by the second track detector, which was installed along the beam line. Figure 5.5 and 5.6 show the antiproton annihilation distribution(d) measured by the upstream side and downstream side track detectors, respectively, together with the magnetic field distribution(b) along the axis and the calculated beam radius(c) which was initially 1 mm in the MRT. A calculation shows that the antiproton cloud with 1 mm radius are transported and focused to 2.5 mm in radius at the focal point (MCP2 in Figs. 5.5 and 5.6) which was 3.3 m downstream from the center of the MRT. Here the harmonic potential well center which corresponds to electrode BH1 was located at 10 cm downstream from the center of

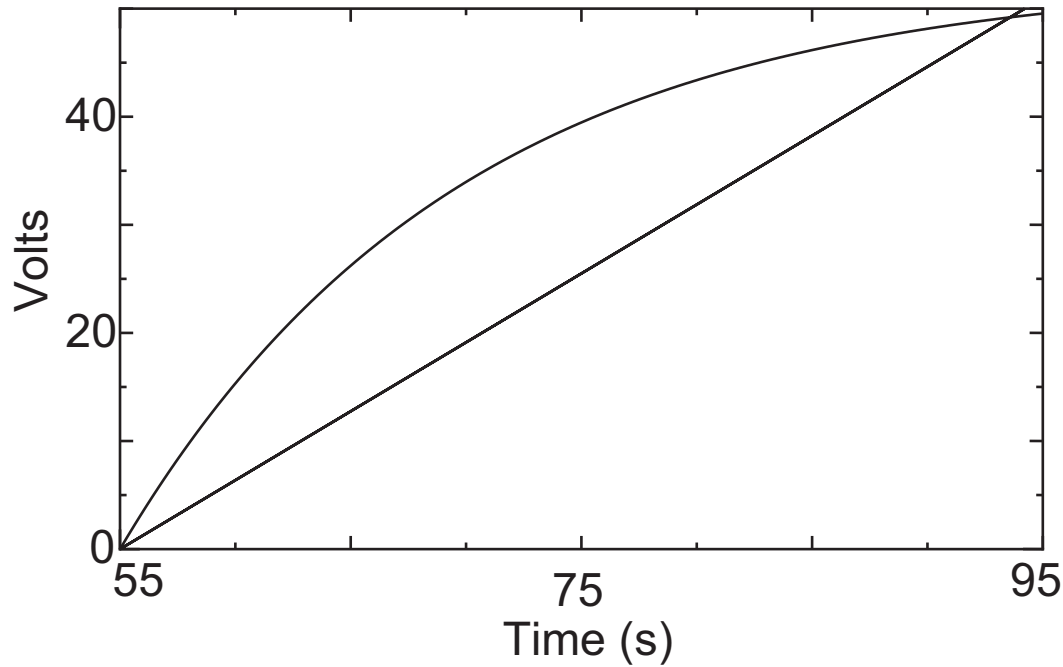


Figure 5.3: Two different functions used for linear and exponential slow extraction.

the superconducting solenoid (See Sec. 2.3.1).

As described in Sec. 5.1.1 a fraction of antiprotons annihilated around 80 cm downstream from the center of the MRT where the extractor electrode was located. Considering that antiprotons follow the magnetic field line, and eventually annihilated at around the extractor electrodes, the diameter of antiproton cloud in the MRT was estimated to be $\sim 15\text{--}20$ mm because the magnetic field at the extractor electrodes were 10–20% of that at the center of the solenoid (see Fig. 5.5 (2)), which was several time larger than that expected from the injected antiproton diameter.

A simulation [69] predicts that an antiproton cloud with its diameter of 2 mm can be transported to the end of the beam line. Most of them whose initial radial position were far from the axis annihilated on the extractor. Although the initial diameter of injected antiproton beam was 2–3 mm (See Sec. 3.2.3 and Fig. 3.5), the final diameter expanded to ~ 15 mm. This unexpected feature is discussed in connection with the first results of the centrifugal separation (Sec. 5.3).

The histogram in Fig. 5.6 (d) shows an example of the measured annihilation position

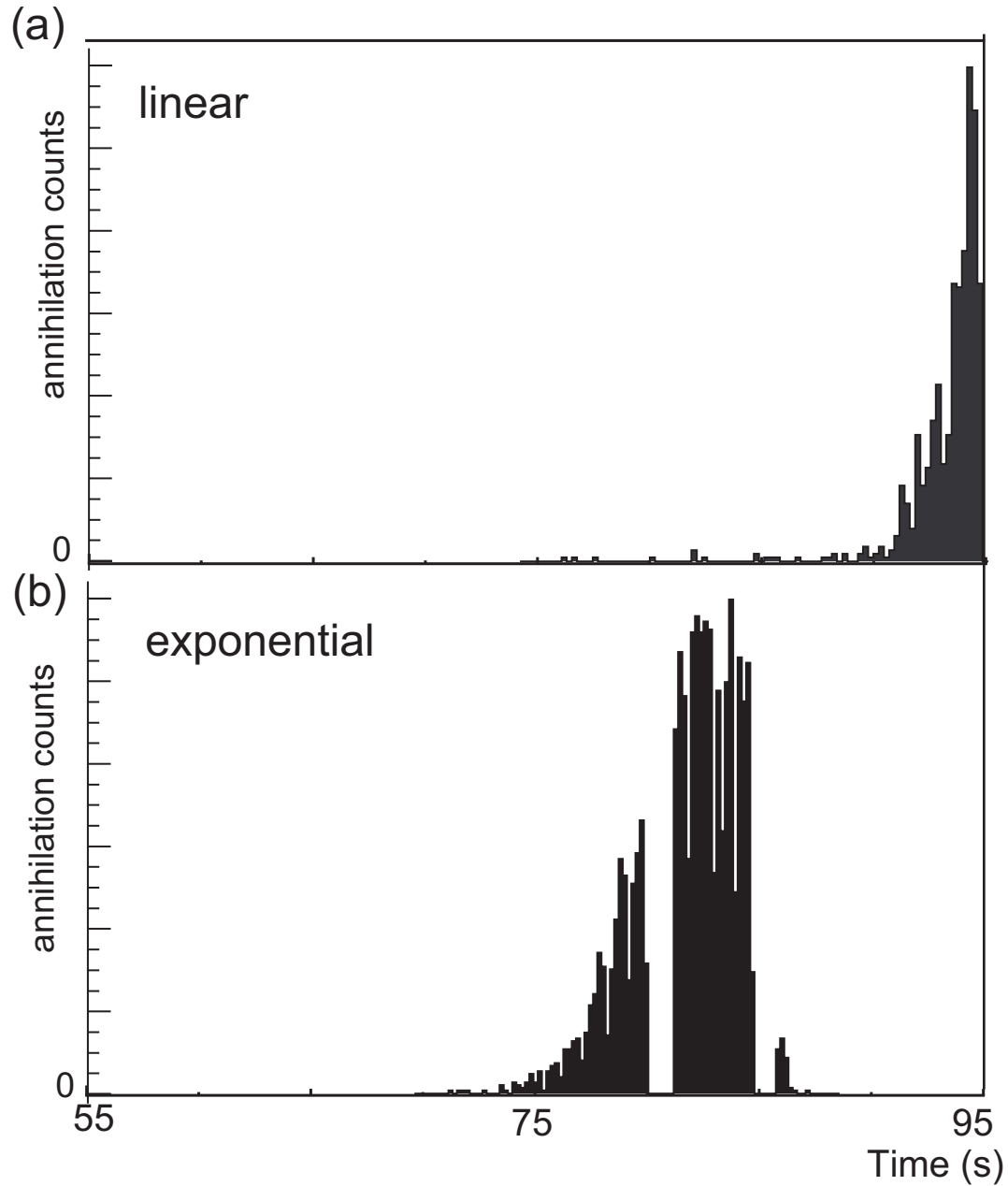


Figure 5.4: Counts at MCP1 [in the pass of the extraction beam line] for (a) linear extraction and (b) exponential extraction. The data from 80 s to 82 s and 85 s to 86 s were accidentally lost because of a problem of the data acquisition system. Here only events coincident with a scintillation detector were recorded.

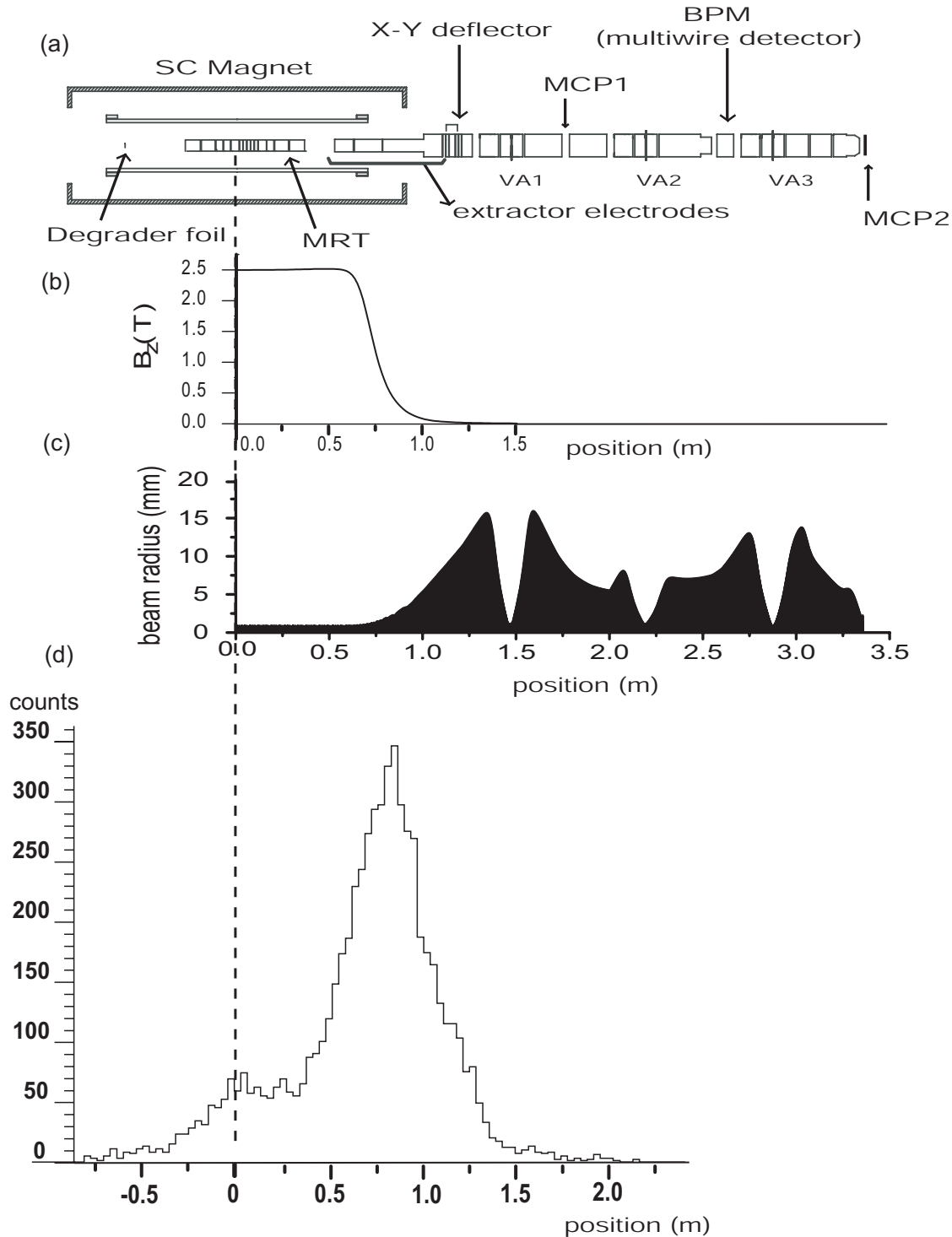


Figure 5.5: Antiproton annihilations detected by the solenoid-side track detector (d). The schematic view of the MRT and transport beam line (a), the magnetic field distribution along the axis (b), B_z , and the calculated beam radius (c) which is initially 1 mm in diameter in the MRT are shown.

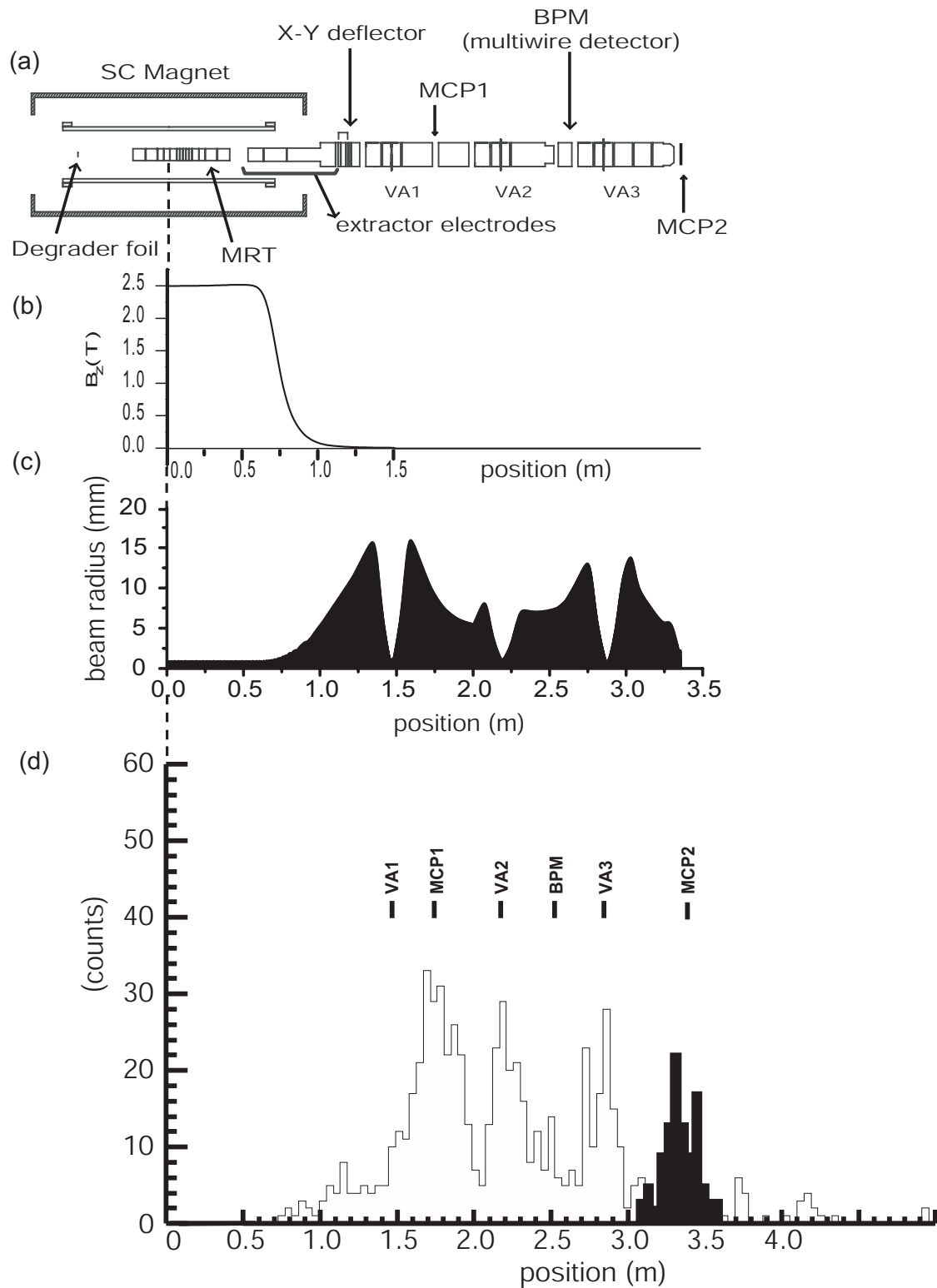


Figure 5.6: Antiproton annihilations along the beam line detected by the beam line-side track detector (d) is shown with the schematic view (a), the magnetic field (b), B_z , and calculated radius of extracted beam (c) which shows that the initial radial position in the MRT of antiprotons which annihilate at several positions are like following; at VA1 1.75 mm, at VA2 1.35 mm, at VA3 1.30 mm, at the focal point (MCP2) 1.15 mm.

distribution along the extraction beam line for a 250 eV antiproton beam. As is seen, the distribution exhibits several peaks along the extraction beam line, which are attributed from left to right to annihilations at the variable aperture VA2 and VA3, while that corresponds to VA1 is missing. The filled peak at 3.3 m corresponds to annihilation at MCP2 where the beam was focused.

To identify the aforementioned annihilation distribution, antiproton trajectories were calculated for various initial radial position, r , of the antiproton in the MRT [69]. Simulated annihilation positions of antiprotons are;

1. upstream of VA1 or at VA1 for $r > 1.75$ mm,
2. between VA1 and VA2 for $1.75 \text{ mm} > r > 1.35$ mm,
3. at VA2 for $r \approx 1.35$ mm,
4. between VA2 and VA3 for $1.35 \text{ mm} > r > 1.30$ mm,
5. at VA3 for $r \approx 1.30$ mm,
6. between VA3 and MCP2 (focal point) for $1.30 \text{ mm} > r > 1.15$ mm.

A part of antiproton cloud whose radial position was smaller than 1.7 mm were transported to the MCP1 installed at 165 cm downstream from the center of the MRT. Figure 5.7 shows that an example of beam profile at the MCP1 had a hollow-like structure somehow. In order to distinguish antiprotons from some negative particles like H^- , only events registered in coincidence with a scintillation detector located near the MCP was counted. At MCP1, the number of extracted antiprotons was 6×10^4 , at the maximum.

A position distribution of particles at the MCP2 which was located at the focal point (Fig. 5.6 (a)) of the beam during the extraction is shown in Fig. 5.8. The number of observed events per shot was 8×10^3 at the maximum, which was comparable to those assigned as annihilations at MCP2 as monitored by the second track detector (filled area in Fig. 5.6) corrected for its solid angle and the multiplicity of the charged pions emitted

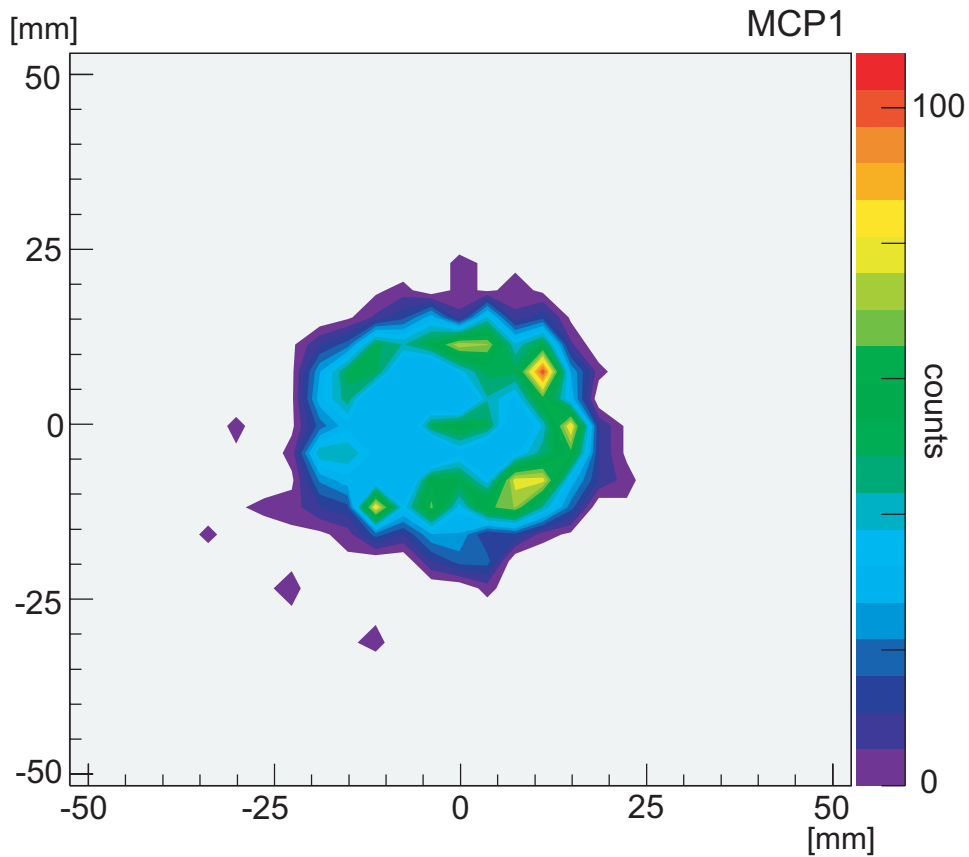


Figure 5.7: Extracted 250 eV antiproton beam profile measured by the MCP in the pass of the extraction beam line.

from each annihilation. It is seen that the distribution was wider than expected. This is one of the evidence that a radial outward separation of antiprotons from the electron plasma has taken place as discussed in the following section, which increases the radius of the antiproton cloud in the MRT, decrease the transmission efficiency, and results in a wider distribution.

Extractions at 500 eV, 100 eV and 10 eV were also performed giving similar distribution and similar number of events at MCP, that is, although the total number of antiprotons transported was not great, antiproton beams as low as 10 eV in energy were prepared for the first time.

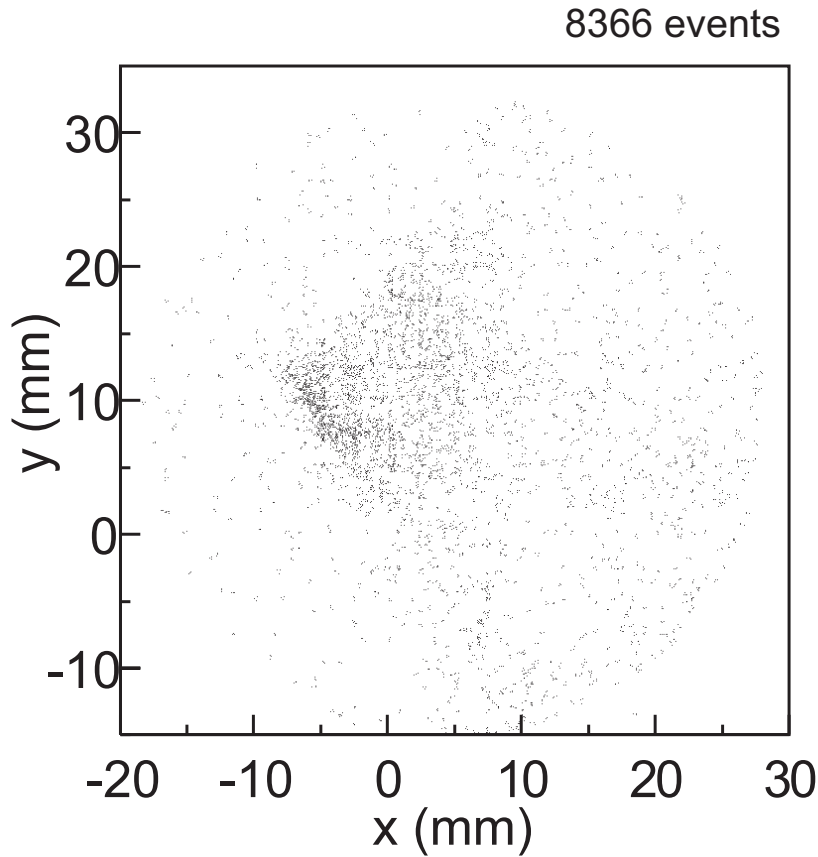


Figure 5.8: The dot plot of particles reaching the MCP located at the focal point of the extraction beam line during 250 eV extraction.

5.3 Extraction efficiency

As described in Sec. 5.1 and 5.2, the number of extracted and transported antiprotons was still small.

Test experiments with positive ions ($p + H_3^+$) (See also App.B.3) were performed. The positive ions cloud of ~ 1 cm in diameter including $\sim 10^6$ ions were extracted from the MRT and transported to the end of the beam line (MCP2). The number of transported ions was $\sim 10^5$.

On the other hand, when $\sim 10^6$ antiprotons 3 mm in diameter (as shown in Sec. 3.2) was injected to the MRT, only $\sim 10^3$ antiprotons were transported to the MCP2 at 10–500 eV.

The annihilation position distribution of Fig. 5.1 indicates that the size of antiproton cloud in the MRT was 15–20 mm in diameter which was 5–7 times larger than that at the moment of the injection. If the radial distribution of antiprotons during the extraction is uniform, the transport efficiency should be $(2/20)^2 \approx 1\%$, which is still 10 times larger than that observed. This indicates that the antiproton cloud had a hollow-like structure. A possible reason of this radial expansion is the centrifugal separation between electron and antiproton clouds coexisting in the MRT.

When two species of ions which has different mass or charge are confined at lower temperature than the present case, centrifugal separation is observed [86] [87]. This separation results because the rotation of the heavier component is slightly slower than that of the lighter one (See App. C.3). Different rotation frequencies induce collisions between differed components resulting in a momentum transfer in θ direction between the species in the cylindrical coordinate (r, θ, z) . The momentum transfer between two species produces an inward force for lighter component and an outward force on the heavier component. The equilibrium density distribution of a two component nonneutral plasma was studied by O’Neil [84] and Kiwamoto et al. [85]. In the present case, from those circumstantial evidences, the centrifugal separation is a possible reason why the number density of antiprotons around the axis was lower, which had never been observed at relatively higher temperature.

5.3.1 Attempt of the radial compression of the antiproton cloud

To compress a charged particle cloud radially, a couple of techniques have been known, i.e., an electric rotating wall field [67] [88] [89] [90] and sideband cooling [91] [92] [93].

The results and possible solutions to improve the efficiency are discussed.

Rotating wall field

The rotating wall method has been developed to control radial distribution of nonneutral plasmas.

Hollmann et al.[89] applied a rotating electric field to an electron plasma and Mg^+ ion plasma via azimuthally segmented electrodes (Fig. 5.9), whose frequencies were around the rigid rotation frequency of plasma. In the case of Mg^+ ions, it took ~ 1000 s to compress the plasma radially.

Greaves et al. [90] and Ichioka [67] succeeded in realizing the radial compression of light particle plasma, i.e., positron and electron plasmas with higher compression rate, respectively. The frequencies were several times higher than rigid rotor frequencies of plasmas. The compression periods were ≤ 10 s in Greaves case, and 30–120 s in Ichioka case.

In both cases, a strong cooling mechanism was required to counteract the heating produced by the applied rotating electric field. Greaves et al. observed that when the background pressure was increased, the compression rate was increased [90].

Since light particles, namely positron and electron, lose their energy in a strong magnetic field (See Sec. 4.2.2), they can be radially compressed by rotating wall field in an ultra-high vacuum condition. In the case of heavier particles like antiproton, the synchrotron radiation cooling rates are negligibly small, and another cooling mechanism should be incorporated. In fact, any improvement of extraction efficiency was not observed.

Therefore the compression of antiproton cloud were tested with electrons in the MRT

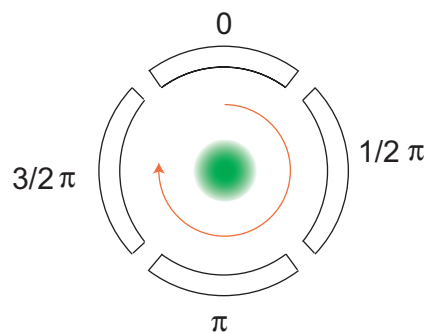


Figure 5.9: Cross section of azimuthally segmented electrode. In this case the electrode is segmented in 4. Oscillating electric fields having 4 different phases are applied to the electrodes.

expecting the electrons to work as coolant via synchrotron radiation. Unfortunately no indications of the compression were observed although the rotating field frequencies were scanned from 300 kHz to 6 MHz. Especially when the rotating field applied more than 120 s, i.e., long time, no antiprotons were transported to the MCP1. It looks that the separation force is stronger than the compression force.

Sideband cooling

In the case of the sideband cooling method, an applied oscillating electric field parametrically couples the azimuthal magnetron motion to the axial bounce motion in a harmonic Penning trap [91] (See also App. B). The oscillating electric field frequency ω is explicitly given by $\omega = \omega_m + \omega_z$ where ω_m is the magnetron motion frequency and ω_z is the bounce motion frequency (See App. B). In usual electromagnetic traps, e.g., Penning-Malmberg trap, this method becomes ineffective for large number of trapped plasmas, because the bounce motion (ω_z) becomes modified by plasma space charge effects. Our MRT can compensate this space charge effects.

As described in App. B, proton and H_3^+ ion clouds were successfully compressed in the worse background pressure, where the bore tube was cooled to 30 K, than the present case.

When the oscillating electric field was applied, it was observed that antiprotons annihilated in the MRT. The reason is not identified but in the case of “pure” antiproton cloud, there was no mechanism to dissipate heat produced by the electric field.

One possible solution is that some amount of electrons coexist during the sideband cooling. Because electrons can be cooled spontaneously via synchrotron radiation cooling. The number of electrons must be kept constant, since the antiproton bounce motion frequency depends on the harmonic potential depth including the electrons’ space charge potential. The coupling between magnetron motion and cyclotron motion of antiproton maybe useful for sideband cooling [94], because cyclotron frequency is independent from the space charge potential of electron and only depends on the magnetic field.

Chapter 6

Conclusions

A large number of antiprotons were cooled and confined in the multi-ring trap by a sequential combination of the AD, the RFQD and the MRT.

Among 3×10^7 antiprotons contained in one AD shot, $\sim 30\%$ of antiprotons were decelerated to 110 keV by the RFQD. The decelerated antiprotons then passed through degrader foils located at the entrance of the MRT and reduced their energy down to around 10 keV. They were captured by the set of high-voltage electrodes. We have succeeded in trapping and cooling of 1.2×10^6 antiprotons via collisions with preloaded electrons. This figure is 50 times more than the best reported values obtained with ordinary thick-foil energy degraders. By stacking several AD shots in sequence, five million antiprotons were confined in the MRT in proportion to the number of AD shots, which is the largest number of cold antiprotons ever accumulated.

During the electron cooling of antiprotons, nondestructive measurements of the electrostatic mode of the plasma were performed to the electron-antiproton two component plasma. We have estimated the temperature variations of the electron plasma and the energy variation of antiprotons from the time evolution of frequencies of the (3,0) mode taking into account the energy distribution of the injected antiproton beam, the electron-antiproton collisions, and the synchrotron radiation cooling. The cooling time of antiprotons to sub-eV was about 30 s.

We also found a frequency shift of the (1,0) mode after the antiproton injection for the

first time. This results from the mixing of electrons and antiprotons.

Finally, cooled antiprotons were extracted from the MRT and were transported to the 3.3 m downstream via the transport beam line which allows differential pumping of six orders of magnitudes. Although the numbers were still small, a few thousands of antiprotons of 10 to 500 eV were delivered to the end of the beam line. This low efficiency indicates that the radius of the antiproton cloud in the MRT was very large and the number of antiprotons around the center axis was smaller, which probably due to centrifugal separation. It is the important future subject to understand the mechanism of radial expansion and to find procedures to compress the radius, which is the necessary condition for efficient extraction of antiprotons from the strong magnetic field.

The author played a leading role in planning and making the experiments at CERN as summarized in the above. Regarding the construction of the experimental setup, the author contributed to the construction of the two dimensional delay line position sensitive detector for measurements of ultra-slow antiprotons, and of the control system.

Appendix A

Planned atomic collision experiment

A.1 Antiproton collision experimental chamber

As described in Sec. 1.2.1, formation cross sections of $\bar{p}p$ or $\bar{p}A^+$ has been theoretically studied [21] [22] [24]. Due to the results, when the energy of the injectile, \bar{p} , is lower, the formation cross section of antiprotonic atoms is larger.

Therefore the ultra-slow antiprotons to be developed in this work enable to investigate the initial process of $\bar{p}A^+$ formation. And the spectroscopic nature of isolated $\bar{p}A^+$ at the initial stage of their formation will be studied.

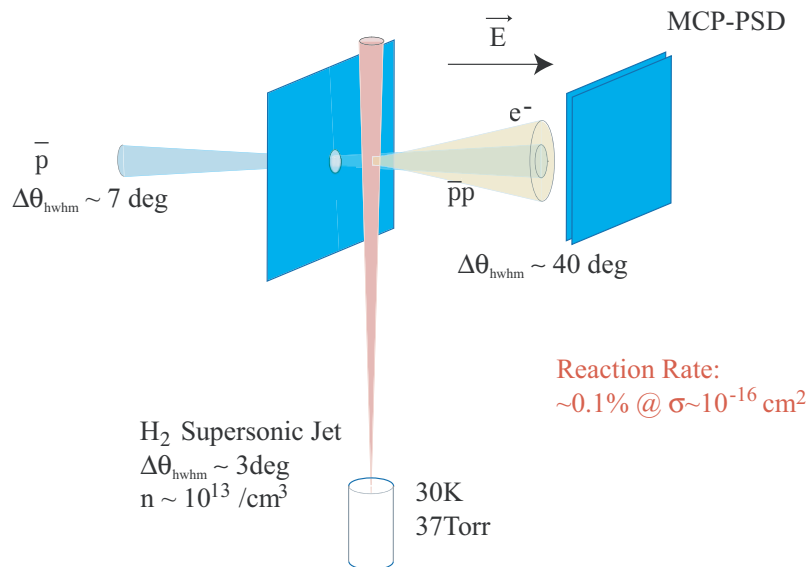


Figure A.1: Schematic drawing of the experimental configuration for antiprotonic hydrogen atom formation.

To study an initial formation stage of antiprotonic hydrogen atom, $\bar{p}p$, an atomic collision experiment is planned [95]. The scheme of the experiment is shown in Fig. A.1. The produced ultra-slow antiprotons are focused and injected to the collision region. Here a supersonic molecular hydrogen gas jet is selected as the target. The MCP-PSD is used to detect the released electron, the antiproton and formed antiprotonic atom. Hence the momentum of $\bar{p}p$ is roughly the same as that of the incident antiproton, and so the traveling time of the $\bar{p}p$ from the collision region to the MCP is a factor of two longer than that of antiproton, the identification of the collision processes is expected to be straightforward. An MCP-PSD to detect antiprotons and the collision products is installed on a rotatable arm in the chamber, and so can detect particles at any angle around the gas jet.

To perform this experiment, a gas target chamber has been developed (Fig. A.2 [96]). This chamber consists of several chambers and dumpers to maintain the pressure at “main chamber” less than 5×10^{-7} Torr. The density of H_2 is designed as high as $1 \times 10^{13}/\text{cm}^3$. From the CTMC and full quantum calculation for the formation cross section of $\bar{p}p$ [23][24], $\sim 10^{-16} \text{ cm}^2$, the expected reaction probability is $\sim 0.1\%$.

Appendix B

Sideband cooling

Charged particles orbit in a Penning trap. To minimize the radius of charged particle's cloud, the sideband cooling technique was applied.

When the radius of antiproton cloud in the MRT is compressed, the extraction and transportation efficiency will increase. This technique was applied to a proton cloud for practice to apply an antiproton cloud. This experiment yields that the proton cloud was successfully compressed radially.

B.1 Particle motion in a trap

In the MRT, as same as in the Penning trap, charged particles' motion is superimposed three motions, axial motion along the direction of the magnetic field, cyclotron motion and magnetron motion (Fig. B.1). The cyclotron frequency under the magnetic field B is given by,

$$\omega_c = \frac{|qB|}{m}, \quad (\text{B.1})$$

with q electric charge, and m mass. The trapping harmonic potential in the MRT is expressed as,

$$\phi_h(r, z) = \phi_0 \frac{R^2 - r^2 + 2z^2}{2L^2}, \quad (\text{B.2})$$

for $|z| \leq L$, where L is the half length of the trapping potential along the axis the MRT, R is the inner radius of the MRT and the (r, z) is the position in the MRT expressed by cylindrical coordinate. Under the above potential, charged particles in the MRT harmonically

	antiproton	electron
cyclotron frequency	38 MHz	70 GHz
magnetron frequency	800 Hz	800 kHz
axial motion frequency	246.8 kHz	10.59 MHz

Table B.1: Three motions of antiproton and electron in the MRT at 2.5 T.

oscillate,

$$\omega_z^2 = \frac{|q\phi_0|}{md^2}. \quad (\text{B.3})$$

The charged particles are also affected by the $\mathbf{E} \times \mathbf{B}$ drift. The equation of this motion is,

$$\ddot{\boldsymbol{\rho}} - \boldsymbol{\omega}_c \times \dot{\boldsymbol{\rho}} - \frac{1}{2}\omega_z^2 \boldsymbol{\rho} = 0. \quad (\text{B.4})$$

This equation has two roots,

$$\omega_+ \equiv \omega'_c = \omega_c - \omega_m, \quad (\text{B.5})$$

$$\omega_- \equiv \omega_m = \frac{\omega_z^2}{2\omega'_c}. \quad (\text{B.6})$$

Here ω'_c , modified cyclotron frequency, is almost same as ω_c , on the other hand ω_m is the magnetron motion of the charged particles.

As is shown in the Fig. B.1, if the magnetron radii of the particles are suppressed, the cloud of the particles will be smaller. This method is known as sideband cooling [91].

B.2 Sideband cooling

As is seen in Fig. B.1, usually, a motion of a particle trapped in a Penning-type electromagnetic trap is superimpose of three motions.

In the trap, when a particle lose the energy, in the case of cyclotron and axial motion, the amplitude of these motion will be smaller. Therefore these motions are stable motion. On the other hand, the radius of the magnetron motion gets larger when the particle lose its energy for the motion. In other words, magnetron motion of a particle moves along the contour line around the top of the potential. The radius of the motion increases with the energy-losing processes, and finally it crashes an electrode of the trap. Since the time

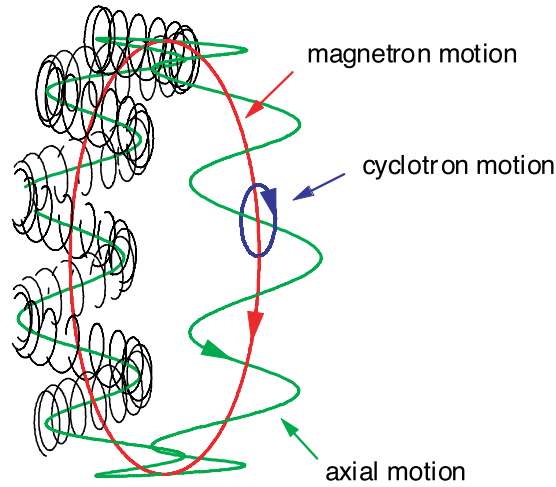


Figure B.1: Charged particle motion in the Penning trap.

constant to reach an electrode is so long, the magnetron motion is metastable. Thus to shrink the radius of the magnetron motion, an energy has to be given to the system. Sideband cooling is a method to decrease the radius of the motion using a coupling between the magnetron motion and the other motion.

The coupling of the different motions is explained by a quantum mechanical treatment [91]. Here we consider the coupling between the magnetron motion and the axial motion, where these motions are denoted as (k, l) . As shown in Fig. B.2, it is supposed that the initial energy state is in (k, l) . There are two kinds of interactions between a trapped particle and a light whose energy is $\hbar(\omega_m + \omega_z)$, that is, absorption of the light $(k, l) \rightarrow (k + 1, l - 1)$ and emission $(k, l) \rightarrow (k - 1, l + 1)$. In the case of absorption, the quantum number of magnetron motion is decreased, and the probability for the transition is proportional to $(k + 1)l$. In contrast, for emission, the number is increased and the probability element is $k(l + 1)$. Therefore, when $l > k$, the process of photon absorption, namely the “cooling” of the magnetron motion is dominant.

Meanwhile, considering transitions $(k, l) \rightarrow (k + 1, l + 1)$ and $(k, l) \rightarrow (k - 1, l - 1)$, they correspond to an absorption and an emission of a light with $\hbar(\omega_z - \omega_m)$ energy. The

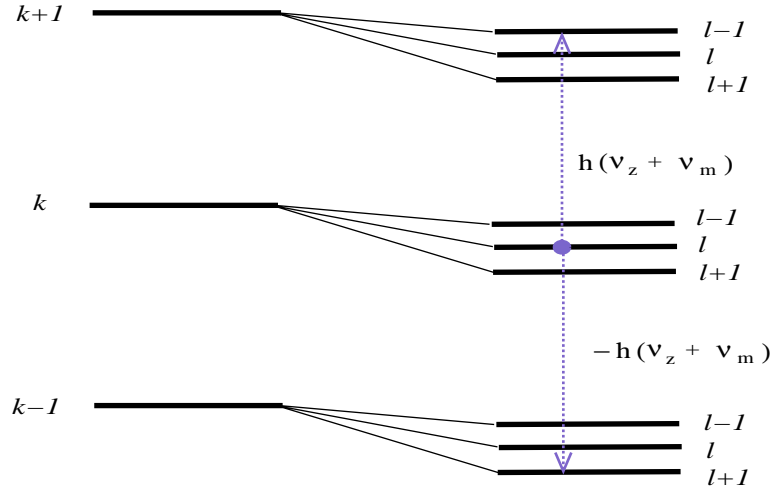


Figure B.2: Scheme of coupling between the axial motion (k) and the magnetron motion (l).

transition probability contains the factor of $(k+1)(l+1)$ for $(k, l) \rightarrow (k+1, l+1)$, and $(k-1)(l-1)$ for $(k, l) \rightarrow (k-1, l-1)$. For this reason, magnetron motion is heated in these case.

In consequence, when the process which gives the energy $\hbar(\omega_m + \omega_z)$ from outside to the particle, magnetron motion of the particle is cooled down.

B.3 Radial compression of proton and H_3^+ ion cloud

Protons and H_3^+ ions were produced by ionizing residual gas which mainly consists of H_2 by 60 eV electrons. From the time-of-flight measurement, produced positive ions were identified, that is to say, mixture of protons and H_3^+ ions formed through ion-molecule reactions like $\text{H}_2^+ + \text{H}_2 \rightarrow \text{H}_3^+ + \text{H}$ [97]. To prepare a pure proton cloud, H_3^+ ions were removed by applying an RF of 140 kHz which was a bounce frequency for H_3^+ ions with 50 V depth harmonic potential [93]. For an H_3^+ ion cloud, protons were kicked out vice versa.

For proton and H_3^+ cloud, the sideband cooling technique was applied by using rotating electric field whose frequency was the sideband frequency ($\omega = \omega_m + \omega_z$). In the MRT,

the sideband frequencies for proton and H_3^+ are theoretically $f_{z,p} = 242$ kHz and $f_{z,h} = 140$ kHz, respectively. As shown in Fig. B.3, we found that the compression worked for a single component cloud and also mixture cloud of proton and H_3^+ ion by applying rotating electric field [92]. Figure B.3 shows the frequencies for compression of proton dominant cloud, H_3^+ ion cloud and mixture of them. This was confirmed by the image of the extracted cloud using a phosphor screen with an MCP located 1.2 m outside of the trap where the magnetic field strength is 100 time weaker than in the MRT. The radius of extracted proton cloud on the phosphor screen was about 1 cm after the compression in contrast to initial 4 cm. Considering the magnetic field, the radius in the MRT was estimated to be about 0.1 cm.

Since the magnetron frequency $f_m \approx f_z^2/2f_c$ is about 800 Hz with cyclotron frequency $f_c \approx 38$ MHz (Table. B.1), the frequency for the sideband cooling is estimated to be 250 kHz. As is seen in Fig. B.3, there are slight discrepancies between theoretical and experimental values. This results from small modification of the effective potential induced by a large number of ions and a small amount of different ion species. In this experiment, it took about 100 s to compress the proton or H_3^+ ion cloud.

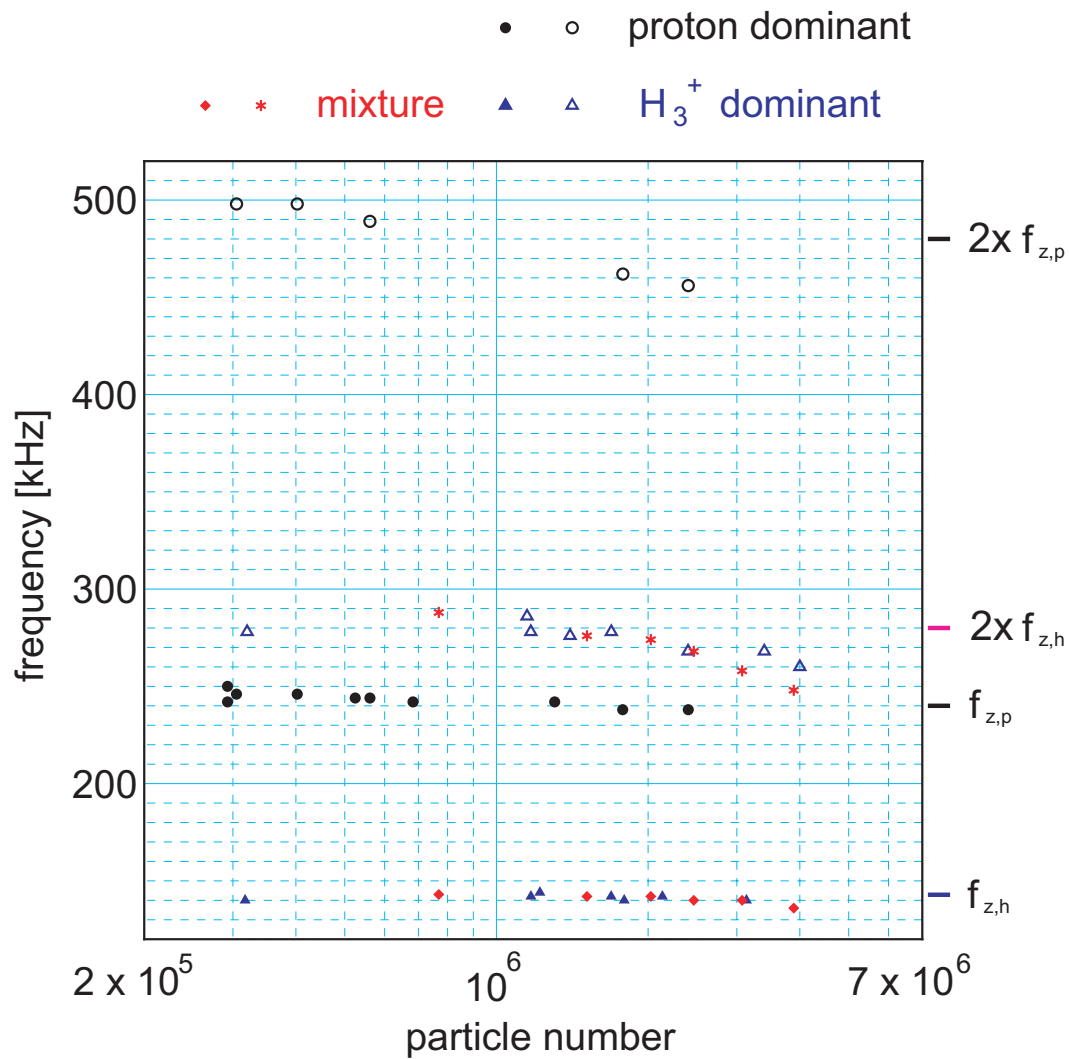


Figure B.3: Frequencies for radial compression for protons and/or H₃⁺ ions as a function of the particle number.

Appendix C

Properties of nonneutral plasma

C.1 Plasma oscillation

Suppose that there is a perturbation in an uniform plasma which displaces a charged particle. Then an electric field arises from the displacement, which is satisfied with the followed Poisson equation;

$$\nabla \cdot \mathbf{E} = \frac{q}{\epsilon_0}(n - n_0). \quad (\text{C.1})$$

Then the particle is accelerated by the field,

$$m \frac{d\mathbf{v}}{dt} = -q\mathbf{E}. \quad (\text{C.2})$$

The density was changed by the particles flux $\Gamma = n_j v_x$ due to the displacement, which is expressed by a equation of continuity,

$$\frac{\partial n}{\partial t} + \nabla \cdot (n\mathbf{v}) = 0. \quad (\text{C.3})$$

Here $n = n_0 + \delta n$ and $\delta n \ll n_0$, then

$$\frac{\partial^2 \delta n}{\partial t^2} + \frac{n_0 q^2}{m \epsilon_0} \delta n = 0. \quad (\text{C.4})$$

This shows that δn oscillates at the frequency

$$\omega_p = \sqrt{\frac{n_0 q^2}{m \epsilon_0}}, \quad (\text{C.5})$$

which wave is called the plasma wave and the frequency is plasma frequency.

C.2 Debye shielding

One of the fundamental nature of a nonneutral plasma is shielding of the electrostatic potential surrounding a test charged particle in a plasma. This shielding distance is called Debye shielding length which is derived as following.

Let assume a test charge (charge q , density n and location in the plasma \mathbf{x}'_0), Poisson's equation for the total electrostatic potential $\phi = \phi_0 + \delta\phi(x, t)$ can be expressed as

$$\nabla^2\phi = \frac{q}{\epsilon_0} \left[n \exp\left(\frac{q\delta\phi}{k_B T}\right) + \delta(\mathbf{x} - \mathbf{x}'_0) \right], \quad (\text{C.6})$$

where $\delta\phi$ is the perturbed potential associated with the introduced test charge.

For $|q\delta\phi/k_B T| \gg 1$, the exponential factor in the above equation is expanded. Relating terms of first order in $\delta\phi$ is expressed as,

$$\nabla^2\delta\phi = \frac{n_0 q^2}{\epsilon_0 k_B T} \delta\phi + \frac{q}{\epsilon_0} \delta(\mathbf{x} - \mathbf{x}'_0), \quad (\text{C.7})$$

where $\lambda_D = \sqrt{\epsilon_0 k_B T / n q^2}$ is called Debye length. The solution to Eq.(C.7) gives the spherically symmetric potential,

$$\delta\phi = \frac{q}{4\pi\epsilon_0 |\mathbf{x} - \mathbf{x}'_0|} \exp\left\{-\frac{|\mathbf{x} - \mathbf{x}'_0|}{\lambda_D}\right\}. \quad (\text{C.8})$$

This means the potential of test charge is shielded in the range of λ_D .

C.3 Rigid rotor equilibrium

In an electromagnetic trap, a plasma rotates as a rigid body. Here assume one species of charged particles. Since particles can move freely along the z -direction, the potential is equivalent along every magnetic field lines. The space charge potential from particles themselves gives rise to an electric field,

$$E_r(r) = q \int_0^r dr' \frac{r' n(r', z)}{\epsilon_0 r}, \quad (\text{C.9})$$

which cause the force qE_r perpendicular to the magnetic field line. Therefore the guiding center drifts to θ -direction with the velocity $v_\theta = E_r/B = r\omega_r(r)$. In consequence, as

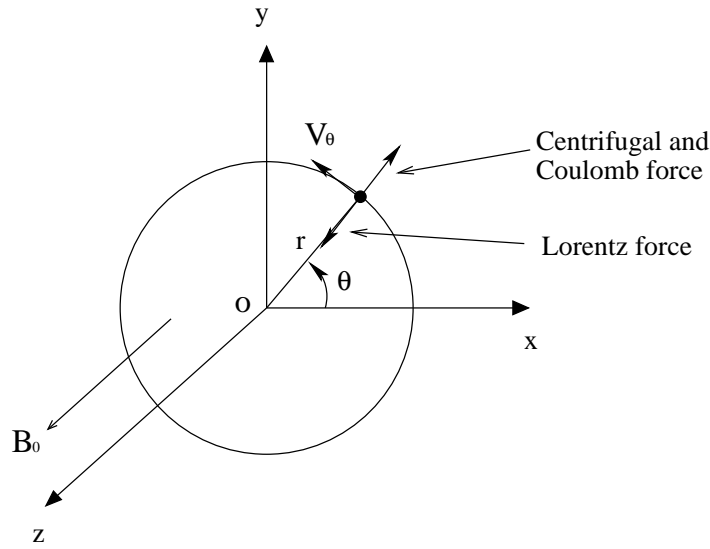


Figure C.1: Force balance of the rotating plasma.

shown in Fig. C.1, the force balance is

$$mr\omega_r^2(r) = -qE_r(r) + qr\omega_r(r)B. \quad (\text{C.10})$$

The rotation frequency $\omega_r(r)$ is given by

$$\omega_r = \omega_r^\pm = \frac{\omega_c}{2} \left[1 \pm \left(1 - \frac{2\omega_p^2}{\omega_c^2} \right) \right]. \quad (\text{C.11})$$

From this relation, it is trivial that ω_r is independent of r , this means that the plasma rotates uniformly. Hence ω_r is called as “rigid rotation frequency”. Equation (C.11) also requests $\omega_p^2/\omega_c^2 \leq 1/2$. This limits the density of the plasma, $n \leq n_B = \varepsilon_0 B^2/2m$, which is called Brillouin density limit.

Here we also discuss about the conservation of canonical angular momentum of non-neutral plasma briefly. Let suppose a system including charged particles, its mass is m and electric charge is q . The canonical angular momentum is expressed as

$$P_\theta = \sum_j \left(mv_\theta r_j + \frac{qBr_j^2}{2} \right). \quad (\text{C.12})$$

Here the ratio between the first term and the second is the ratio of Larmor radius and the plasma radius. Under a strong magnetic field, the first term can be neglected. When a

particle gets away from the axis, from $\sum_j r_j^2/2 = \text{const.}$, another particle comes close to the axis. Therefore a long time confinement of nonneutral plasma is guaranteed.

In the following subsections, we consider two components nonneutral plasma and its thermal equilibrium [49].

C.3.1 Vlasov equation

A motion of a particle in a phase space is expressed as,

$$\frac{dq_i}{dt} = \frac{\partial H(q_j, p_j, t)}{\partial p_i}, \quad (\text{C.13})$$

$$\frac{dp_i}{dt} = -\frac{\partial H(q_j, p_j, t)}{\partial q_i}. \quad (\text{C.14})$$

From Liouville's theorem, a time evolution of small volume Δ is

$$\frac{d\Delta}{dt} = \sum_i \left(\frac{\partial^2 H}{\partial p_i \partial q_i} - \frac{\partial^2 H}{\partial q_i \partial p_i} \right) \Delta = 0. \quad (\text{C.15})$$

The total number of particles in the volume $\delta N = f(q_i, p_i, t) \delta \mathbf{p} \delta \mathbf{q}$ is conserved under the collisionless condition where $f(q_i, p_i, t)$ is a distribution function in a phase space, namely,

$$\frac{\partial f}{\partial t} + \sum_i \left(\frac{\partial H}{\partial p_i} \frac{\partial f}{\partial q_i} - \frac{\partial H}{\partial q_i} \frac{\partial f}{\partial p_i} \right) = 0. \quad (\text{C.16})$$

Hamiltonian expressed by a Cartesian coordinate, $x_1, x_2, x_3, v_1, v_2, v_3$, is given by

$$H = \frac{1}{2m} (\mathbf{p} - q\mathbf{A})^2 + q\phi, \quad (\text{C.17})$$

$$p_i = mv_i + qA_i, \quad (\text{C.18})$$

$$q_i = x_i. \quad (\text{C.19})$$

The Hamiltonian equation is

$$\frac{dx_i}{dt} = \frac{\partial H}{\partial p_i} = v_i, \quad (\text{C.20})$$

$$\frac{dp_i}{dt} = -\frac{\partial H}{\partial x_i} = \sum_k \frac{(p_k - qA_k)}{m} q \frac{\partial A_k}{\partial x_i} - q \frac{\partial \phi}{\partial x_i}. \quad (\text{C.21})$$

Then Eq. (C.16) is rewritten as,

$$\frac{\partial f}{\partial t} + \sum_i v_i \frac{\partial f}{\partial x_i} + q \sum_i \left(\sum_k v_k \frac{\partial A_k}{\partial x_k} - \frac{\partial \phi}{\partial x_i} \right) \frac{\partial f}{\partial p_i} = 0, \quad (\text{C.22})$$

where

$$\sum_k v_k \frac{\partial A_k}{\partial x_i} = (\mathbf{v} \cdot \nabla) A_i + (\mathbf{v} \times (\nabla \times \mathbf{A}))_i. \quad (\text{C.23})$$

By using Eq. (C.18) and (C.19), Eq. (C.22) is given by,

$$\frac{\partial f}{\partial t} + \sum_i v_i \frac{\partial f}{\partial x_i} + \sum_i \frac{q}{m} (\mathbf{E} + \mathbf{v} \times \mathbf{B})_i \frac{\partial f}{\partial v_i} = 0. \quad (\text{C.24})$$

The above equation is called Vlasov equation, namely collisionless Boltzmann equation. The variation of the function f affects the charge and current distribution changes the electric and magnetic fields through Maxwell equations. As a result, the distribution f is affected. Therefore this Vlasov equation contains a long range interaction between particles in the plasma.

C.3.2 Rigid rotor Vlasov equilibria

For nonrelativistic particles, we can write the distribution function [49] [98],

$$f_j^0 = f_j(H_\perp - \omega_{rj} P_\theta) g_j(p_z), \quad (\text{C.25})$$

with constants of motion under a thermal equilibrium. Here, $p_z = m_j v_z$ is the axial momentum of particle- j with velocity, v_z . The canonical angular momentum P_θ is calculated as

$$P_\theta = r \left(p_\theta + \frac{q_j B r}{2} \right). \quad (\text{C.26})$$

Moreover the perpendicular energy H_\perp defined by

$$H_\perp = \frac{1}{2m} (p_r^2 + p_\theta^2) + q_j \phi(r). \quad (\text{C.27})$$

Here, the combination $H_\perp - \omega_{rj} P_\theta$ is expressed in the form

$$H_\perp - \omega_{rj} P_\theta = \frac{1}{2m} [p_r^2 + (p_\theta - m_j \omega_{rj} r)^2] + \psi_j(r), \quad (\text{C.28})$$

where the effective potential $\psi_j(r)$ is defined by

$$\psi_j(r) = \frac{m_j}{2} \left(-\frac{q_j B \omega_{rj}}{m_j} - \omega_{rj}^2 \right) r^2 + q_j \phi_0(r). \quad (\text{C.29})$$

From Eqs. (C.25) and (C.29), it is evident that the average azimuthal flow velocity reduces to

$$v_{\theta j}^0(r) = \omega_{rj} r. \quad (\text{C.30})$$

Therefore, the average azimuthal motion of component j corresponds to a rigid rotation with angular velocity $\omega_{rj} = \text{const}$.

The density profile can be expressed as

$$\begin{aligned} n_j^0(r) &= \int f_j^0(r, \mathbf{p}) d^3 p, \\ n_j^0(r) &= \hat{n}_j \int_0^\infty f_j(U + \phi_j(r)) dU, \end{aligned} \quad (\text{C.31})$$

where $U = p_r^2 + (p_\theta - m_j r \omega_{rj})^2 / (2m)$.

Near the axis of the plasma column ($r = 0$), Eq.(C.31) can be integrated to give $\phi_0(r) = -(\sum_k \pi \hat{n}_k q_k) r^2$, where $\psi_j(r) = 0$ and $n_j^0(r) = 1$. Substituting into Eq.(C.29) gives

$$\begin{aligned} \psi_j(r) &= \frac{m_j}{2} \left(-\frac{q_j B \omega_{rj}}{m_j} - \omega_{rj}^2 \frac{2q_j}{m_j} \sum_k \pi \hat{n}_k q_k \right) r^2, \\ &= -\frac{m_j}{2} (\omega_{rj} + \omega_{rj}^+) (\omega_{rj} - \omega_{rj}^-) r^2, \end{aligned} \quad (\text{C.32})$$

for small value of r . Here, ω_{rj}^+ and ω_{rj}^- are the rotation frequency defined by

$$\omega_{rj}^\pm = -\frac{q_j B}{2m_j} \left\{ 1 \pm \left(1 - \sum_k \frac{2n_j q_k n_k}{m_j \omega_{c_j}^2} \right)^{1/2} \right\}. \quad (\text{C.33})$$

For antiproton and electron two components plasma, Eq.(C.33) is rewritten as

$$\omega_{r\bar{p}} = \frac{\omega_{c\bar{p}}}{2} \left\{ 1 - \left(\frac{2}{\omega_{c\bar{p}}^2} \left(\omega_{p\bar{p}}^2 + \omega_{pe}^2 \frac{m_e}{m_{\bar{p}}} \right) \right)^{1/2} \right\}. \quad (\text{C.34})$$

Thermal equilibrium corresponds to the rigid rotor distribution function [99],

$$f^0(r, \mathbf{p}) = \frac{n_j}{(2\pi m_j k_B T)^{3/2}} \exp\left\{ -\frac{H - \omega_{rj} P_\theta}{k_B T} \right\}, \quad (\text{C.35})$$

where, T , the temperature is constant.

Bibliography

- [1] O. Chamberlain, E. Segrè, C. Wiegand, and T. Ypsilantis. Observation of Antiprotons. *Phys. Rev.*, 100(3):947, November 1955.
- [2] A. Apostolakis, E. Aslanides, G. Backenstoss, P. Bargassa, O. Behnke, A. Benelli, V. Bertin, F. Blanc, P. Bloch, P. Charlson, M. Carroll, E. Cawley, M.B. Chertok, M. Danielsson, M. Dejardin, J. Derre, A. Ealet, C. Eleftheriadis, W. Fetscher, M. Fidecaro, A. Filipčič, D. Francis, J. Fry, E. Gabathuler, R. Gamet, H.-J. Gerber, A. Go, A. Haselden, P.J. Hayman, E. Henry-Couannier, R.W. Hollander, K. Jon-And, P.-R. Kettle, P. Kokkas, R. Kreuger, R. Le Gac, F. Leimgruber, I. Mandić, N. Manthos, G. Marel, M. Mikuž, J. Miller, F. Montanet, A. Muller, T. Nakada, B. Pagels, I. Papadopoulos, P. Pavlopoulos, G. Polivka, R. Rickenbach, B.L. Roberts, T. Ruf, L. Sakeliou, M. Schäfer, L.A. Schaller, T. Schietinger, A. Schopper, L. Tauscher, C. Thibault, F. Touchard, C. Touramanis, C.W.E. Van Eijk, S. Vlachos, P. Weber, O. Wigger, M. Wolter, C. Yeche and D. Zavrtnik, and D. Zimmerman. A determination of the CP violation parameter η_{+-} from the decay of strangeness-tagged neutral kaons. *Phys. Lett. B*, 458(4):545, July 1999.
- [3] C.J. Batty. Antiprotonic-hydrogen atoms. *Rep. Prog. Phys.*, 52(10):1165, October 1989.
- [4] H. Knudsen and J.F. Reading. Ionization of atoms by particle and antiparticle impact. *Phys. Rept.*, 212(issues 3-4):107, March 1992.

- [5] J.C. Evance Jr. and R.I. Steinberg. Nucleon Stability: A Geochemical Test Independent of Decay Mode. *Science*, 197(4307):989, September 1977.
- [6] C. Amsler. Proton-antiproton annihilation and meson spectroscopy with the Crystal Barrel. *Rev. Mod. Phys.*, 70(4):1293, October 1998.
- [7] J. Eades and F.J. Hartmann. Forty years of antiprotons. *Rev. Mod. Phys.*, 71(1):373, January 1999.
- [8] T. Yamazaki, E. Widmann, R.S. Hayano, M. Iwasaki, S.N. Nakamura, K. Shigaki, F.J. Hartmann, H. Daniel, T. von Egidy, P. Hofmann, Y.-S. Kim, and J. Eades. Formation of long-lived gas-phase antiprotonic helium atoms and quenching H₂. *Nature*, 361(6409):238, January 1993.
- [9] M. Hori, J. Eades, R.S. Hayano, T. Ishikawa, J. Sakaguchi, E. Widmann, H. Yamaguchi, H.A. Torii, B. Júhasz, D. Horváth, and T. Yamazaki. Sub-ppm Laser Spectroscopy of Antiprotonic Helium and a CPT-Violation Limit on the Antiprotonic Charge and Mass. *Phys. Rev. Lett.*, 87(9):093401, August 2001.
- [10] H.A. Torii, R.S. Hayano, M. Hori, T. Ishikawa, N. Morita, M. Kumakawa, I. Sugai, T. Yamazaki, B. Ketzer, F.J. Hartmann, T. von Egidy, R. Pohl, C. Maierl, D. Horváth, J. Eades, and E. Widmann. Laser measurements of the density shifts of resonance lines in antiprotonic helium atoms and stringent constraint on the antiproton charge and mass. *Phys. Rev. A*, 59(1):223, January 1999.
- [11] G. Gabrielse, X. Fei, K. Helmerson, S.L. Rolston, R. Tjoelker, and T.A. Trainer. First capture of antiproton in a Penning trap: A Killoelectron volt source. *Phys. Rev. Lett.*, 57(20):2504, November 1986.
- [12] M.H. Holtzscheiter, X. Feng, T. Goldman, N.S.P King, R.A. Lewis, M.M. Nieto, and G.A. Smith. Are antiprotons forever? *Phys. Lett. A*, 214(5-6):279, May 1996.

- [13] G. Gabrielse, A. Khabbaz, D.S. Hall, C. Heimann, H. Kalinowsky, and W. Jhe. Precision Mass Spectroscopy of the Antiproton and Proton Using Simultaneously Trapped Particles. *Phys. Rev. Lett.*, 82(16):3198, April 1999.
- [14] G. Bauer, G. Boero, S. Brauksiepe, A. Buzzo, W. Eyrich, R. Geyer, D. Grzonka, J. Hauffe, K. Kilian, M. LoVetere, M. Macri, M. Moosburger, R. Nellen, W. Oelert, S. Passaggio, A. Pozzo, K. Röhrich, K. Sachs, G. Schepers, T. Sefzick, R.S. Simon, R. Stratmann, F. Stinzinger, and M. Wolke. Production of antihydrogen. *Phys. Lett. B*, 368(1-3):251, February 1996.
- [15] G. Blanford, D.C. Christian, K. Gollwitzer, M. Mandelkern, C.T. Munger, J. Schultz, and G. Zioulas. Observation of Atomic Antihydrogen. *Phys. Rev. Lett.*, 80(14):3037, April 1998.
- [16] M. Amoretti, C. Amsler, G. Bonomi, A. Bouchta, P. Bowe, C. Carraro, C.L. Cesar, M. Charlton, M.J.T. Collier, M. Doser, V. Filippini, K.S. Fine, A. Fontana, M.C. Fujiwara, R. Funakoshi, P. Genova, J.S. Hangst, R.S. Hayano, M.H. Holzschneider, L.V. Jørgensen, V. Lagomarsino, R. Landua, D. Lindelöf, E.L. Rizzini, M. Macrì, N. Madsen, G. Manuzio, M. Marchesotti, P. Montagna, H. Pruys, C. Regenfus, P. Riedler, J. Rochet, A. Rotondi, G. Rouleau, G. Testera, A. Variola, T.L. Watson, and D.P. Van der Werf. Production and detection of cold antihydrogen. *Nature*, 419(6906):456, October 2002.
- [17] G. Gabrielse, N.S. Bowden, P. Oxley, A. Speck, C.H. Storry, J.N. Tan, M. Wessels, D. Grzonka, W. Oelert, G. Schepers, T. Sefzick, J. Waltz, H. Pittner, T.W. Hänsch, and E.A. Hessels (ATRAP Collaboration). Background-Free Observation of Cold Antihydrogen with Field-Ionization Analysis of Its States. *Phys. Rev. Lett.*, 89(21):213401, November 2002.
- [18] E. Fermi and E. Teller. The Charge of Negative Mesotrons in Matter. *Phys. Rev.*, 72(5):399, September 1947.

- [19] T. Yamazaki, N. Morita, R.S. Hayano, E. Widmann, and J. Eades. Antiprotonic helium. *Phys. Rept.*, 366(issues 4-5):183, August 2002.
- [20] E. Widmann, J. Eades, T. Ishikawa, J. Sakaguchi, T. Tasaki, H. Yamaguchi, R.S. Hayano, M. Hori, H.A. Torii, B. Juhász, D. Horváth, and T. Yamazaki. Hyperfine Structure of Antiprotonic Helium Revealed by a Laser-Microwave-Laser Resonance Method. *Phys. Rev. Lett.*, 89(24):243402, December 2002.
- [21] J.S. Cohen and N.T. Padial. Initial distribution, cascade, and annihilation of $\bar{p}p$ atoms formed in $\bar{p} + H$ and $\bar{p} + H^-$ collisions in near vacuum. *Phys. Rev. A*, 41(7):3460, April 1990.
- [22] J.S. Cohen. Capture of negative muons and antiprotons by noble-gas atoms. *Phys. Rev. A*, 65(5):052714, May 2002.
- [23] J.S. Cohen. Molecular effects on antiproton capture by H_2 and the states of $\bar{p}p$ formed. *Phys. Rev. A*, 56(5):3583, November 1997.
- [24] K. Sakimoto. Full quantum-mechanical study of protonium formation in slow collisions of antiproton with hydrogen atoms. *Phys. Rev. A*, 65(1):012706, January 2001.
- [25] K. Sakimoto. Protonium formation in slow collisions of antiprotons with hydrogen atoms. *J. Phys. B*, 34(9):1769, May 2001.
- [26] G. Budker and A.N. Skrinsky. Electron cooling and new possibilities in elementary particle physics. *Sov. Phys. -Usp.*, 21(4):277, April 1978.
- [27] M.H. Holtzscheiter and M. Charlton. Ultra-low energy antihydrogen. *Rep. Prog. Phys.*, 62(1):1, January 1999.
- [28] G. Gabrielse, S.L. Rolston, L. Haarsma, and W. Kells. ANTIHYDROGEN PRODUCTION USING TRAPPED PLASMAS. *Phys. Lett. A*, 129(1):38, May 1988.

- [29] M. Charlton. Antihydrogen production in collisions of antiprotons with excited states of positronium. *Phys. Lett. A*, 143(3):143, January 1990.
- [30] J. Mitroy and A.T. Stelbovics. Formation of antihydrogen from antiproton collisions with positronium. *J. Phys. B*, 27(3):79, February 1994.
- [31] A. Igarashi, N. Toshima, and T. Shirai. Hyperspherical coupled-channel calculation for antihydrogen formation in antiproton-positronium collisions. *J. Phys. B*, 27(15):497, August 1993.
- [32] D.S. Hall and G. Gabrielse. Electron Cooling of Protons in a Nested Penning Trap. *Phys. Rev. Lett.*, 77(10):1962, September 1996.
- [33] G. Gabrielse, J. Estrada, J.N. Tan, P. Yesley, N.S Bowden, P. Oxley, T. Roach, C.H. Storry, M. Wessels, J. Tan, D. Grzonka, W. Oelert, G. Schepers, T. Sefzick, W.H. Breunlich, M. Cargnell, H. Fuhrmann, R. King, R. Ursin, J. Zmeskal, H. Kalinowsky, C. Wesdorp, J. Walz, K.S.E. Eikema, and T.W. Hänsch. First positron cooling of antiprotons. *Phys. Lett. B*, 507(1-4):1, May 2001.
- [34] R.G. Greaves and C.M. Surko. Antimatter plasmas and antihydrogen. *Phys. Plasmas*, 4(5):1528, May 1997.
- [35] T.M. Squires, P. Yesley, and G. Gabrielse. Stability of a Charged Particle in a Combined Penning-Ioffe Trap. *Phys. Rev. Lett.*, 86(23):5266, June 2001.
- [36] D.H.E. Dubin. Three designed for a magnetic trap that will simultaneously confine neutral atoms and a non-neutral plasma. *Phys. Plasmas*, 8(10):4331, October 2001.
- [37] J. Waltz, S.B. Ross, C. Zimmermann, L. Ricci, M. Prevedelli, and T.W. Hänsch. Combined Trap with the Potential for Antihydrogen Production. *Phys. Rev. Lett.*, 75(18):3257, October 1995.
- [38] A. Mohri and Y. Yamazaki. A possible new scheme to synthesize antihydrogen and to prepare a polarized antihydrogen beam. *EuroPhys. Lett.*, 63(2):207, July 2003.

- [39] M. Niering, R. Holzwarth, J. Reichert, P. Pokasov, Th. Udem, M. Wietz, T.W. Hänsch, P. Lemonde, G. Santarelli, M. Abgrall, P. Laurent, C. Salomon, and A. Clairon. Measurement of the Hydrogen $1S$ - $2S$ Transition Frequency by Phase Coherent Comparison with a Microwave Cesium Fountain Clock. *Phys. Rev. Lett.*, 84(24):5496, June 2000.
- [40] R.J. Hughes. Antihydrogen and fundamental symmetries. *Hyperfine Interactions*, 76:3, 1993.
- [41] P.F. Winkler, D. Kleppner, T. Myint, and F.G. Walther. Magnetic Moment of the Proton in Bohr Magnetrons. *Phys. Rev. A*, 5(1):83, January 1972.
- [42] A. Kreissl, A.D. Hancock, H. Koch, Th. Köhler, H. Poth, U. Raich, D. Rohmann, A. Wolf, L. Tauscher, A. Nilsson, M. Suffert, M. Chardalas, S. Dedoussis, H. Daniel, T. von Egidy, F.J. Hartmann, W. Kanert, H. Plendl, G. Schmidt, and J.J. Reidy. Re-measurement of the magnetic moment of the antiproton. *Z. Phys. C*, 37:557, 1988.
- [43] E. Widmann, J. Eades, R.S. Hayano, M. Hori, D. Horvath, T. Ishikawa, B. Juhasz, J. Sakaguchi, H.A. Torii, H. Yamaguchi, and T. Yamazaki. Hyperfine Structure Measurements of Antiprotonic Helium and Antihydrogen. In S.G. Kahrhenboim, editor, *The Hydrogen Atom; Precision Physics of Simple Atomic Systems*, volume 570 of *Lecture notes in Physics*, page 528, Heidelberg, 2001. Springer Verlag.
- [44] G. Gabrielse, N.S. Bowden, P. Oxley, A. Speck, C.H. Storry and J.N. Tan, M. Wessels, D. Grzonka, W. Oelert, G. Schepers, T. Sefzick, and J. W. Waltz ATRAP Collaboration. Stacking of cold antiprotons. *Phys. Lett. B*, 548(3-4):140, November 2002.
- [45] M. Amoretti, C. Amsler, G. Bonomi, A. Bouchta, P.D. Bowe, C. Carraro, M. Charlton, M.J.T Collier, M. Doser, V. Filippini, K.S. Fine, A. Fontana, M.C. Fujiwara, R. Funakoshi, P. Genova, A. Glauser, D. Grögler, J. Hangst, R.S. Hayano, H. Higaki, M.H. Holtzscheiter, W. Joffrain, L.V. Jørgensen, V. Lagomarsino, R. Landua, C. Lenz Cesar, D. Lindelöf, E. Lodi-Rizzini, M. Macri, N. Madsen, D. Manuzio, G. Manuzio,

- M. Marchesotti, P. Montagna, H. Pruys, C. Regenfus, P. Riedler, J. Rochet, A. Rontoni, G. Rouleau, G. Testera, D.P. van der Werf, A. Variola, T.L. Watson, T. Yamazaki, and Y. Yamazaki. The ATHENA antihydrogen apparatus. *Nucl. Instrum. Methods in Phys. Res. A*, 518(3):679, February 2004.
- [46] W. Paul. Electromagnetic traps for charged and neutral particles. *Rev. Mod. Phys.*, 62(3):531, July 1990.
- [47] F.M. Penning. Die Glimmentladung bei niedrigem druck zwischen koaxialen Zylindern in einem axialen Magnetfeld. *Physica*, III(9):873, November 1936.
- [48] D.J. Wineland and W.M. Itano. High-resolution spectroscopy of stored ions. *Adv. At. Mol. Phys.*, 19:135, 1983.
- [49] Ronald C. Davidson. *PHYSICS OF NONNEUTRAL PLASMAS*. Imperial College Press and World Scientific, London, 2001.
- [50] G. Gabrielse, L. Haarsma, and S.L. Rolston. OPEN-ENDCAP PENNING TRAPS FOR HIGH PRECISION EXPERIMENTS. *Int. J. Mass Spec. and Ion Proc.*, 88:319, 1989.
- [51] J.H. Malmberg and J.S. deGrassie. Properties of Nonneutral Plasmas. *Phys. Rev. Lett.*, 35(9):577, September 1975.
- [52] C.F. Driscoll and J.H. Malmberg. Length-Dependent Containment of a Pure Electron-Plasma Column. *Phys. Rev. Lett.*, 50(3):167, January 1983.
- [53] A. Mohri, H. Higaki, H. Tanaka, Y. Yamazawa, M. Aoyagi, T. Yuyama, and T. Michishita. Confinement of Nonneutral Spheroidal Plasmas in Multi-Ring Electrode Traps. *Jpn. J. Appl. Phys.*, 37(1-2):664, February 1998.
- [54] M.H. Holtzscheiter, R.E. Brown, J.B. Camp, S. Cornford, T. Darling, P. Dyer, T. Goldman, S. Høibråten, K. Hosea, R.J. Hughes, N. Jarmie, R.A. Kenefick, N.S.P.

- King, D.C. Lizon, M.M. Nieto, M.M. Midzor, S.P. Parry, J. Rochet, R.A. Ristinen, M.M. Schauer, J.A. Schecker, and F.C. Witteborn. Trapping of antiprotons in a large Penning trap – progress towards a measurement of the gravitational acceleration of the antiproton. *Nucl. Phys. A*, 558:709c, June 1993.
- [55] G. Gabrielse, X. Fei, L.A. Orozco, R.L. Tjoelker, J. Haas, H. Kalinowsky, T.A. Trainor, and W. Kells. Thousandfold improvement in the measured antiproton mass. *Phys. Rev. Lett.*, 65(11):1317, September 1990.
- [56] S. Maury, P. Belochitskii, J. Bosser, J. Buttkus, C. Carti, F. Caspers, V. Chohan, D. Cornuet, T. Eriksson, A. Findlat, M. Giovannozzi, B. Holzer, D. Möhl, R. Maccaferri, N. Madsen, M. Marchesotti, S. Pasinelli, F. Pedersen, L. Soby, J. Tan, and G. Tranquille. Commissioning the First Operation of the Antiproton Decelerator (AD). In P. Lukas and S. Webber, editors, *Proceedings of the 2001 Particle Accelerator Conference*, page 580, Chicago, 2001. IEEE.
- [57] A.M. Lombardi. Decelerating and Accelerating RFQs. In C.E. Eyberger, R.C. Pardo, and M.M. White, editors, *Proceedings of the XIX International LINAC Conference*, page 377, Chicago, 1998. IEEE.
- [58] J. Bosser, P. Bourquin, M. Brouet, B. Couturier, G. Gelato, M. Giovannozzi, F. Grandclaude, J.-Y. Hémerly, A.M. Lombardi, U. Mikkelsen, S. Maury, D. Möhl, F. Pedersen, W. Pirkel, U. Raich, H.H. Umstätter, and M. Vretenar. FEASIBILITY STUDY OF A DECELERATING RADIO FREQUENCY QUADRUPOLE SYSTEM FOR THE ANTIPROTON DECELERATOR AD. PS/HP Note 97-36, CERN, Genève, Switzerland, January 1998.
- [59] A.M. Lombardi, W. Pirkel, and Y. Bylinsky. First Operating Experience with the CERN Decelerating RFQ for Antiprotons. In P. Lukas and S. Webber, editors, *Proceedings of the 2001 Particle Accelerator Conference*, page 585, Chicago, 2001. IEEE.

- [60] M. Hori, J. Eades, R.S. Hayano, T. Ishikawa, W. Pirkl, E. Widmann, H. Yamaguchi, H.A. Torii, B. Juhász, D. Horváth, and T. Yamazaki. Direct measurement of transition frequencies in isolated $\bar{p}\text{He}^+$ atoms, and new CPT violation limits on the antiproton charge and mass. *Phys. Rev. Lett.*, 91(12):123601, September 2003.
- [61] A.M. Lombardi. private communication.
- [62] T.J. Murphy and C.M. Surko. Positron trapping in an electrostatic well by inelastic collisions with nitrogen molecules. *Phys. Rev. A*, 46(9):5696, November 1992.
- [63] G. Bollen and S. Schwarz. Ion traps for radioactive beam manipulation and precision experiments. *Nucl. Instrum. Methods Phys. Res. B*, 204:466, May 2003.
- [64] O. Kester, T. Sieber, S. Emhofer, F. Ames, K. Reisinger, P. Reiter, P.G. Thirolf, R. Lutter, D. Habs, B.H. Wolf, G. Huber, P. Schmidt, A.N. Ostrowski, R. von Hahn, R. Repnow, J. Fitting, M. Lauer, H. Scheit, D. Schwalm, H. Podlech, A. Schempp, U. Ratzinger, O. Forstner, F. Wenander, J. Cederkäll, T. Nilsson, M. Lindroos, H. Fynbo, S. Franchoo, U. Bergmann, M. Oinonen, J. Äystö, P. Van Den Bergh, P. Van Duppen, M. Huyse, N. Warr, D. Weisshaar, J. Eberth, B. Jonson, G. Nyman, M. Pantea, H. Simon, G. Shrieder, A. Richter, O. Tengblad, T. Davinson, P.J. Woods, G. Bollen, L. Weissmann, L. Liljeby, K.G. Rensfelt, and the ISOLDE Collaboration. Accelerated radioactive beams from REX-ISOLDE. *Nucl. Instrum. Methods Phys. Res. B*, 204:20, May 2003.
- [65] M. Wada, Y. Ishida, T. Nakamura, Y. Yamazaki, T. Kambara, H. Ohyama and Y. Kanai, T.M. Kojima, Y. Nakai, N. Oshima, A. Yoshida, T. Kubo, Y. Matsuo, Y. Fukuyama, K. Okada, T. Sonoda, S. Ohtani, K. Noda, H. Kawakami, and I. Katayama. Slow RI-beams from projectile fragment separators. *Nucl. Instrum. Methods Phys. Res. B*, 204:570, May 2003.

- [66] G. Gabrielse, X. Fei, L.A. Orozco, R.L. Tjoelker, J. Haas, H. Kaliowsky, T.A. Trainor, and W. Kells. Cooling and Slowing of Trapped Antiprotons below 100 meV. *Phys. Rev. Lett.*, 63(13):1360, September 1989.
- [67] T. Ichioka. *Development of intense beam of ultracold antiprotons*. PhD thesis, University of Tokyo, 2001.
- [68] C.A. Spindt, C.E. Holland, A. Rosengreen, and I. Brodie. Field-emitter arrays for vacuum microelectronics. *IEEE Trans. Elec. Dev.*, 38(10):2355, October 1991.
- [69] K. Yoshiki Franzen, N. Kuroda, H.A. Torii, M. Hori, Z. Wang, H. Higaki, S. Yoneda, B. Juhász, D. Horváth, A. Mohri, K. Komaki, and Y. Yamazaki. Transport beam line for ultraslow monoenergetic antiprotons. *Rev. Sci. Instrum.*, 74(7):3305, July 2003.
- [70] M. Hori, K. Yamashita, R.S. Hayano, and T. Yamazaki. Analog Cherenkov detectors used in laser spectroscopy experiments on antiprotonic helium. *Nucl. Instrum. Methods Phys. Res. A*, 496(1):102, January 2003.
- [71] 米田 諭 (YONEDA Satoshi). 超音速ガスジェット標的実験槽の設計製作と極低温反陽子ビームの引き出し (in Japanese). 修士論文 (Master's thesis), 東京大学 (University of Tokyo), 2002.
- [72] CERN Program Library Long Writeup W5013, Geneva. *GEANT Ver.3*.
- [73] M.D. Tinkle, R.G. Greaves, C.M. Surko, R.L. Spencer, and G.W. Mason. Low-Order Modes as Diagnostics of Spheroidal Non-neutral Plasmas. *Phys. Rev. Lett.*, 72(3):352, January 1994.
- [74] C.S. Weimer, J.J. Bollinger, F.L. Moore, and D.J. Wineland. Electrostatic modes as a diagnostic in Penning-trap experiments. *Phys. Rev. A*, 49(5):3842, May 1994.
- [75] A.W. Trivelpiece and R.W. Gould. Space Charge Waves in Cylindrical Plasmas Columns. *J. Appl. Phys.*, 30(11):1784, November 1959.

- [76] D.H.E. Dubin. Theory of Electrostatic Fluid Modes in a Cold Spheroidal Non-Neutral Plasma. *Phys. Rev. Lett.*, 66(16):2076, April 1991.
- [77] H. Higaki, N. Kuroda, T. Ichioka, K. Yoshiki Franzen, Z. Wang, K. Komaki, and Y. Yamazaki. Electron cooling of high-energy protons in a multiring trap with a tank circuit monitoring the electron-plasma oscillations. *Phys. Rev. E*, 65(4):046410, April 2002.
- [78] D.H.E. Dubin and J.P. Schiffer. Normal modes of cold confined one-component plasmas. *Phys. Rev. E*, 53(5):5249, May 1996.
- [79] F. Anderegg, N. Shiga, D.H.E. Dubin, C.F. Driscoll, and R.W. Gould. Thermally excited Trivelpiece-Gould modes as a pure electron plasma temperature diagnostic. *Phys. Plasmas*, 10(5):1556, May 2003.
- [80] B.R. Beck, J. Fajans, and J.H. Malmberg. Temperature and anisotropic-temperature relaxation measurements in cold, pure-electron plasmas. *Phys. Plasmas*, 3(4):1250, April 1996.
- [81] S. Ichimaru and M.N. Rosenbluth. Relaxation Processes in Plasmas with Magnetic Field. Temperature Relaxations. *Phys. Fluids*, 13(11):2778, November 1970.
- [82] T.M. O'Neil and P.G. Hjorth. Collision dynamics of a strongly magnetized pure electron plasma. *Phys. Fluids*, 38(11):3241, November 1985.
- [83] D.V. Sivukhin. COULOMB COLLISIONS IN A FULLY IONIZED PLASMA. In Acad. M.A. Leontovich, editor, *Review of Plasma Physics*, volume 4, New York, 1966. Consultants Bureau.
- [84] T.M. O'Neil. Centrifugal separation of a multispecies pure ion plasma. *Phys. Fluids*, 24(8):1447, August 1981.

- [85] Y. Kiwamoto, A. Mohri, and M. Fujiwara. Equilibrium Density Distribution of a Two-Species Plasma with a Single Sign of Charge. *J. Phys. Soc. Jpn.*, 73(1):102, January 2004.
- [86] D.J. Larson, J.C. Bergquist, J.J. Bollinger, W.M. Itano, and D. Wineland. Sympathetic cooling of trapped ions: A laser cooled two-species nonneutral plasma. *Phys. Rev. Lett.*, 57(1):70, July 1986.
- [87] H. Imajo, L. Hayasaka, R. Ohmukai, U. Tanaka, M. Watanabe, and S. Urabe. Spatial separation of ion clouds between sympathetically laser-cooled Cd^+ -ion isotopes. *Phys. Rev. A*, 55(2):1276, February 1997.
- [88] F. Anderegg, E.M. Hollmann, and C.F. Driscoll. Rotating Field Confinement of Pure Electron Plasma Using Trivelpiece-Gould Modes. *Phys. Rev. Lett.*, 81(22):4875, November 1998.
- [89] E.M. Hollmann, F. Anderegg, and C.F. Driscoll. Confinement and manipulation of non-neutral plasmas using rotating wall electric fields. *Phys. Plasmas*, 7(7):2776, July 2000.
- [90] R.G. Greaves and C.M. Surko. Inward Transport and Compression of a Positron Plasma by a Rotating Electric Field. *Phys. Rev. Lett.*, 85(9):1883, August 2000.
- [91] L.S. Brown and G. Gabrielse. Geonium theory: Physics of a single electron or ion in a Penning trap. *Rev. Mod. Phys.*, 58(1):233, January 1986.
- [92] H. Higaki, N. Kuroda, K. Yoshiki Franzen, Z. Wang, M. Hori, A. Mohri, K. Komaki, and Y. Yamazaki. Radial compression of protons and H_3^+ ions in the multiring trap: for the production of ultra low energy antiproton beams. *submitted to Phys. Rev. E*.
- [93] 黒田 直史 (KURODA Naofumi). 反陽子プラズマの電子冷却と制御法の開発 (in Japanese). 修士論文 (Master's thesis), 東京大学 (University of Tokyo), 2001.

- [94] G. Bollen, S. Becker, H.-J. Kluge, M. König, R.B. Moore, T. Otto, H. Rainmbault-Hartmann, G. Savard, L. Schweikhard, and the ISOLDE Collaboration H. Stolzenberg. ISOLTRAP: a tandem Penning trap system for accurate on-line mass determination of short-lived isotopes. *Nucl. Instrum. Methods Phys. Res. A*, 368(3):675, January 1996.
- [95] Y. Yamazaki. Production of ultra slow antiprotons, its application to atomic collisions and atomic spectroscopy – ASACUSA project. *Nucl. Instrum. Methods Phys. Res. B*, 154:174, June 1999.
- [96] Z. Wang. private communication.
- [97] M.G. Holliday, J.T. Muckerman, and L. Friedman. Isotopic Studies of the Proton-Hydrogen Molecule Reaction. *J. Chem. Phys.*, 54(3):1058, February 1971.
- [98] R.C. Davidson and N.A. Krall. Vlasov Equilibria and Stability of an Electron Gas. *Phys. Fluids*, 13(6):1543, June 1970.
- [99] R.C. Davidson and N.A. Krall. Vlasov Description of an Electron Gas in a Magnetic Field. *Phys. Rev. Lett.*, 22(16):833, April 1969.

Acknowledgements

超低速反陽子ビームの生成は、CERN に於ける ASACUSA 共同実験の最終目標の一つである反陽子原子生成初期過程の研究と分光に必須です。ここに、この様な形でまとめることが出来たのは、一重に指導教官の山崎泰規教授の御指導、御鞭撻の故です。先生の指導、要所所での適切なる助言がなければ、ここまで研究を進めることが出来なかつたかもしれません。また、指導教官ではないにも関わらず、普段より指導して下さい、本論文も丁寧に読み返して逐次誤りを指摘して下さい小牧研一郎教授にも深く感謝致します。

毛利明博京都大学名誉教授には、トラップ中の荷電粒子雲、プラズマの振舞いを理解する上で重要であるにも拘らず著者には全く不明であった非中性プラズマという分野を紹介して下さいただでなく、実験にも参加して下さい、漂流しそうになる実験に解決への方向性を与えて下さいました。

鳥居寛之助手には CERN での実験中だけに限らず、様々な場面で議論に乗って頂きました。

著者とほぼ同じ時期にこの実験プロジェクトに参加された Ken Yoshiki Franzen 博士がいなければ、超低速反陽子輸送ビームラインは今日のような形にはならなかつたでしょう。いつも冷静にこちらの見落すような点まで気を配って下さいました。

CERN の堀正樹博士は、実験装置や計測系、データ解析の全面に渡り面倒を見て下さり、ともすればその複雑さに飲込まれそうになる著者に適切かつ簡潔極まりない助言を与えて下さいました。また、反陽子散乱実験槽の設計製作を担当された王志剛博士、そして track detector のシミュレーションなどで貢献してくれた米田諭氏、忍耐強くビームタイムに参加し実験を手伝ってくれた井上正人氏にも感謝します。実験中、CERN では共同研究者の Újvári Balázs 氏、Juhász Bertalan 氏、Barna Dániel 氏の力にも大いに助けられました。勿論実験だけでなく、John Eades 上級研究員、Horváth Dezső 教授、早野龍五教授を始め、ASACUSA 共同実験のメンバーとの様々な議論を通じて、低速反陽子を使った研究に興味をかきたてられました。また、RFQD の設計開発をされた CERN の旧 PS-division の方々、特に Werner Pirkl 氏には実験中大いに助けて頂きました。ここに厚く御礼申し上げます。

CERN に於いて反陽子を使った本実験を始める前に、東京大学駒場キャンパスにある地下実験室で、陽子や H^- イオン、電子を使った予備実験を行っていました。この時、檜垣浩之博士には装置の使い方に始まり、電子回路製作など実験遂行上必要な様々なことを教えて頂きました。市岡利康博士には事細かに物理を説明して下さい、同じく立ち上げ時から携わっておられた大島永康博士共々、本研究の礎を築いて下さいました。理化学研究所の神原正副主任研究員には、著者が研究を始めた頃に手取り足取り面倒を見て頂きました。本研究で使用された MCP-PSD はその成果です。この予備実験中に消費した莫大な量の寒剤を休みなく提供して下さい小田嶋豊氏、石田晶紀氏、芦沢佳子氏にも深く感謝致します。

勿論、本研究に直接関係がなくとも同じ研究室に所属する皆様には普段の研究生活を通じて様々な場面で助けて頂きました。

最後にこのような研究活動を行なうことに理解を示し、経済的精神的な支えとなってくれた家族に深い感謝の念を捧げます。